Applications of hybrid measurements with discrete and continuous variables

Laghaout, Amine; Andersen, Ulrik Lund

Publication date:
2013

Document Version
Publisher's PDF, also known as Version of record

Applications of hybrid measurements with discrete and continuous variables

Department of Physics, Technical University of Denmark

PhD Candidate: Amine Laghaout

Supervisor: Prof. Ulrik Lund Andersen

June 14, 2013

Acknowledgements

I would like first and foremost to thank my supervisor, Prof. Ulrik Lund Andersen, for having me as a PhD student in his group these past three years. His approachable character and the independence he conferred me in carrying out my research have made for a pleasant work environment.

I am also indebted to Prof. Gunnar Björk for the patient correspondence he had with me in the course of 2010 and 2011 and from which two publications have ensued. Jonas Schou Neergaard-Nielsen, who helped me through my last year, has been inspirational with his clear thinking and vast knowledge of both theoretical and experimental quantum optics. My laboratory experience is owed to the most part to Anders Tipsmark who dutifully introduced me to all the workings of the cat state setup. I would also like to thank Alexander Huck, whose work ethic pervaded the office we shared, for answering my daily impromptu questions on both theory and experiment.

Last but not least, I would like to say thank you to all other members of the Quantum Information group for having made these past three years an enriching experience both at the academic and personal level.

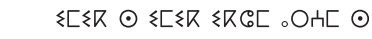

Applications of hybrid measurements with discrete and continuous variables

Abstract. The main topic of this thesis revolves around quantum measurement. We illustrate how two different views of quantum objects, the discrete- and continuous-variable views, can be combined to more effectively distinguish between orthogonal states. Such combined measurements are referred to as hybrid. The discrete-variable view is more appropriate to probe energy eigenstates. However, when two or more energy eigenstates are superposed, accurate measurements in the energy eigenbasis require rotations in phase space which are very unwieldy as they require strong nonlinearities and elaborate interactions between light and matter. On the other hand, energy eigenstate superpositions carry a continuous relative phase which is easily probed by continuous-variable interference measurements such as homodyning. The tradeoff between photon counting and homodyning is in practice determined by feasibility studies. This is what we do for two particular applications of quantum measurements: Bell tests and the amplification of Schrödinger cat states. This project also had an experimental component which was supposed to produce high-fidelity Schrödinger cat states. This goal turned out to be hampered by noise from the laser as well as a series of anomalous behavior of the nonlinear crystal whereby no classical de-amplification, and therefore no squeezing, could be observed.

Anvendelser af hybride målinger med diskrete og kontinuerte variable

Dansk resumé. Det vigtigste emne for denne afhandling kredser omkring kvantemåling. Vi viser hvordan to forskellige beskrivelser af et kvanteobjekt—den diskrete og den kontinuerte variable tilgang—kan kombineres, og derved mere effektivt kan skelne mellem ortogonale tilstande. Sådanne kombinerede målinger omtales som hybride. Den diskrete variable tilgang er mere hensigtsmæssigt til at måle energi-egentilstande, men når to eller flere energi-egentilstande er overlejret kræver nøjagtige målinger i energi-egenbasen rotationer i Fock-rummet. Disse er meget besværlige, da de kræver stærke ikke-lineariteter eller vanskelige interaktioner mellem lys og stof. På den anden side bærer superpositionerne af energi-egentilstande en kontinuerlig relativ fase, som let probes ved kontinuerte variable interferensmålinger såsom homodyning. Afvejningen mellem foton tælling og homodyning bestemmes i praksis ved forundersøgelser. Dette er, hvad vi gør for to særlige anvendelser af kvante målinger: Bell test og forstærkningen af Schrödinger kat-tilstande. Dette projekt havde også en eksperimentel komponent. Målet var at producere meget rene Schrödinger kat-tilstande med anvendelse indenfor kvanteinformatik. Dette mål viste sig at være hæmmet af støj fra laseren samt en serie af unormal adfærd af det ulineære krystal, hvorved ingen klassisk negativ forstærkning, og derfor ingen squeezing, kunne observeres.

Contents

Chapter 1

Introduction

As far as informatics is concerned, the related superposition and uncertainty principles that pertain to the quantum world present an advantage and disadvantage, respectively. Whereas the former can be harnessed for powerful computational applications via coherent interference and entanglement, the latter renders the measurement process very challenging. Simply put, this is because quantum measurements consist of projecting a complex, multi-dimensional quantum object onto a one-dimensional classical spectrum. To perform such operations, one needs to devise an optimal—though not always possibly ideal—strategy which takes into account both the nature of the quantum state and the set of experimental devices at hand. To illustrate this point, consider the intuitive sketch of projective measurements in Fig. 1.1 where "quantum objects" and measurements are represented by three- and two-dimensional shapes, respectively. If the object can be lain flat onto the measurement surface so that both areas match exactly, then the measurement can be pictured as ideal. However, we rarely are able to tailor the measurement perimeter as the range of measurement devices is limited. To pursue the classical analogy, if the imprint of the measured object onto the measuring interface is only partial, we effectively have an approximate measurement which is prone to ambiguity. The name of the game is therefore to see how the quantum object can be re-oriented or re-shaped so as to maximize its overlap with the measurement device. Rephrased in mathematical terms, the goal is to transform the states and measurement operators such that the interaction Hamiltonian between the them is diagonalized.

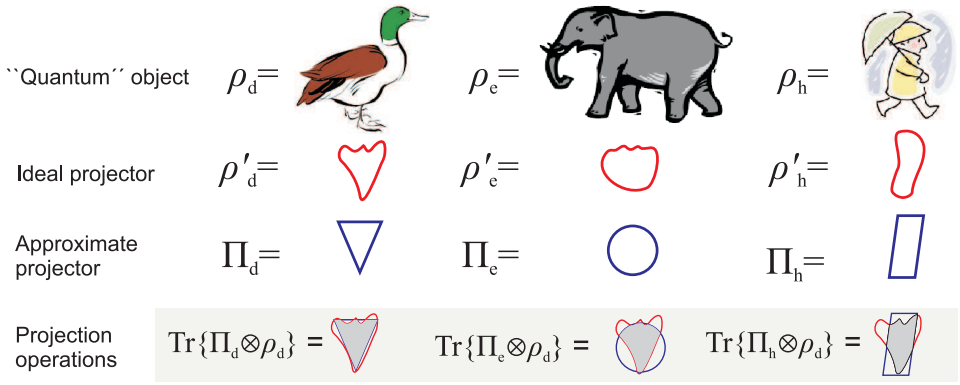

Figure 1.1: Toy model for the measurement problem of quantum mechanics. Quantum objects $\hat{\rho}$ span a mutli-dimentional Hilbert space of which we can only see a cross-section at time due to the complementarity principle. The imprint of the object on that cross-section, just like a footprint on the ground, is thus the only signature of the object available to identify it. Ideally, the measurement projector consists of a "cast" $\hat{\rho}'$ which perfectly matches the imprint. In practice, however, the measurement devices available in the laboratory are only approximations $\hat{\Pi}$ of this ideal cast. In addition, any given object may exhibit partial overlap with the ideal projector of a different object, thereby leading to ambiguous measurement. (We assume of course that all objects are "normalized", i.e., that all footprint areas are equal.)

As an illustration of how hard it can be to measure certain states, we shall describe in Chapter 3 an instance of Bell measurements where the probability of success is restricted to 50% for linear operations [1]. The difficulty with such measurements originates from the fact that the states at hand lie in a basis other than the energy eigenbasis. One has therefore to rotate the state so as to align it with the measurement basis. As will be shown, although this method works in principle, it nonetheless is a testimony to the difficulty in measuring certain states.[1]

If one is willing to sacrifice the quality of quantum measurement by allowing for some inaccuracy in the readout of detection, then one has to devise approximate projectors (cf. Fig. 1.1). In Chapter 4, such projectors are built to discriminate two orthogonal Fock state superpositions, which—once again—are not aligned with the energy eigenbasis, namely $\frac{1}{\sqrt{2}}(|0\rangle \pm |1\rangle)$.

[1] Chapter 3 is adapted from Phys. Rev. A **85**, 022316 (2012).

The accuracy of the discrimination is then incorporated in a feasibility study for Bell tests, where the conclusiveness of the test is quantified as a function of quantum efficiencies.[2]

Another specificity of quantum measurements is that, unlike their classical counterparts, they are not only ends in themselves, but can also serve computational purposes in the processing of quantum states. They can indeed be thought of as operations in Hilbert space which reduce a multimode input into a smaller sub-state with certain desired properties. This technique is variously referred to as a measurement-induced operation, post-selection, or heralding. Chapter 5 will be devoted to illustrating this point for the purpose of amplifying coherent state superpositions in realistic conditions.[3]

As transpires from the above, the recurring theme of this dissertation is therefore quantum measurement. We shall however start in the next chapter by illustrating two ways of looking at quantum objects, namely the discrete variable (DV) and continuous variable (CV) approaches. Whereas the first describes optical quanta in a discrete Hilbert space, the second is the formal analog of the phase space picture. In very loose terms, the DV and CV pictures can be alternated depending on whether one is interested in probing the particle-like or wave-like nature of light. As we shall see, DV and CV degrees of freedom are best recorded by photon-counting and homodyne detectors, respectively. The two types of detectors can then be put to use at different parts of a same setup. Such arrangements, either for state measurement or state preparation, are known as *hybrid* [2], and will be featured in Chapters 4 and 5.

The last chapter, though somewhat unrelated to the central theme of the thesis, serves as a record of the experimental challenges faced in the course of the project.

[2]Chapter 4 is adapted from Phys. Rev. A **84**, 062127 (2011).
[3]Chapter 5 is adapted from Phys. Rev. A **87**, 043826 (2013).

Chapter 2

Quantum optics toolbox

Today's informatics is mostly realized by the field of classical electronics. Information is represented in discrete electric charges which propagate in a circuit according to the rules of boolean logic to produce the desired output. These three main components—the representation, processing, and readout of information—are also present in quantum information (Tab. 2.1). The goal of this chapter is to present these three compartments of the quantum optics toolbox.

2.1 Representations

Classical information encoded in electrical signals can either be analog or digital. Whereas the former can add up as continuous functions, the latter obey the rules of boolean logic. One can see in these two representations of classical information a manifest similarity with the wave and particle representations from modern physics. The novelty in quantum mechanics is that the two representations are fundamentally one and the same: Discrete quanta can add up and interfere as wave-like probability distributions. For the external observer, the choice of whether to measure a quantum system

	Classical	**Quantum**
Representation	Digital or analog	Discrete or continuous variable
Storage	Electronic charges (bits)	Quantum states (qubits)
Foundation	Boolean logic	Superposition principle
Probability	Always extrinsic	Either inherent or extrinsic

Table 2.1: Qualitative comparison of classical and quantum information.

as a wave or particle really reduces to a choice of strategy depending on what aspect of information is to be extracted.

This section describes the digital (DV) and analog (CV) representations of the quantum objects, namely the Fock and Wigner functions. By quantum objects, we will come to mean not only the quantum states that carry the information, but also the operators that act on these carriers, i.e., measurement projectors.

2.1.1 Fock

The most intuitive quantum representation of optical states is that which enumerates photons in any given field mode. This is known as the photon-number, or Fock, representation; its Hilbert space is spanned by the energy eigenstates $\{|n\rangle\}$, where n is the number of photons. Let's briefly review how this Hilbert space arises from a formal analogy between the energetics of the electromagnetic field and that of a harmonic oscillator [3].

Consider an electric field of amplitude E_0 pointing in the Cartesian x direction and propagating along z,

$$E_x(z,t) = E_0 \sin(kz)\sin(\omega t), \tag{2.1}$$

where k is the wave vector and ω is the angular frequency. With the magnetic field being orthogonal to the electric field, Maxwell-Ampère's equation,[1]

$$\nabla \times \vec{B} = \epsilon_0\mu_0 \frac{\vec{E}}{\partial t} \Rightarrow -\frac{\partial B_y}{\partial z} = \epsilon_0\mu_0 \frac{\partial E_x}{\partial t}, \tag{2.2}$$

is solved by

$$B_y(z,t) = \frac{E_0}{c}\cos(kz)\cos(\omega t). \tag{2.3}$$

The electromagnetic energy density is therefore given by

$$\begin{aligned} U &= \frac{1}{2}\left(\epsilon_0 E^2 + \frac{1}{\mu_0}B^2\right) \\ &= \frac{1}{2}\epsilon_0 E_0^2 \left(\sin^2 kz \sin^2 \omega t + \cos^2 kz \cos^2 \omega t\right). \end{aligned} \tag{2.4}$$

Let's assume the light to be confined to an arbitrary cavity of transverse area A and length L such that its volume is $V = AL$. The contained

[1] We are here treating the case where the magnetization current $\vec{J}$ is null.

electromagnetic energy $\mathcal{E}$ is then

$$\begin{aligned}\mathcal{E} &= \int_V U \,\mathrm{d}V \\ &= A\int_0^L U(z)\,\mathrm{d}z \\ &= \frac{1}{4}\epsilon_0 E_0^2 V\left(\sin^2\omega t + \cos^2\omega t\right), \end{aligned} \tag{2.5}$$

where we assumed that the field vanishes at the boundaries; i.e., we have a standing wave inside the cavity. If we now substitute[2]

$$\begin{cases} x(t) = \frac{1}{\omega}\sqrt{\frac{\epsilon_0 V}{2}}E_0 \sin\omega t \\ p(t) = \sqrt{\frac{\epsilon_0 V}{2}}E_0 \cos\omega t \end{cases} \tag{2.6}$$

into the Hamiltonian of the harmonic oscillator

$$\mathcal{H} = \frac{1}{2}\left(p^2 + \omega^2 x^2\right), \tag{2.7}$$

we see that we recover (2.5). Notwithstanding the choice of units, the electric and magnetic fields are thus formally reducible to the position and momentum of a harmonic oscillator.

Now that we have arrived at the harmonic oscillator Hamiltonian, there remains to follow any standard quantum mechanics textbook's treatment of how quantization ensues from the correspondence rule [4]. We then obtain

$$\hat{\mathcal{H}} = \hbar\omega\left(\hat{a}^\dagger\hat{a} + \frac{1}{2}\right), \tag{2.8}$$

where the operators $\hat{a}^\dagger$ and $\hat{a}$ respectively create and annihilate excitations of the electromagnetic field—photons—of energy $\hbar\omega$ and exhibit the non-commutativity relation $[\hat{a}, \hat{a}^\dagger] = 1$. The Schrödinger equation,

$$\hat{\mathcal{H}}|n\rangle = \hbar\omega\left(n + \frac{1}{2}\right)|n\rangle, \tag{2.9}$$

is solved by the energy eigenstates $\{|n\rangle\}$ consisting of n indistinguishable photons of frequency ω. These solutions, also known as Fock states, obey

[2]Beware of notational confusion: The variable $x(t)$ here has nothing to do with the transverse Cartesian coordinate x.

the following key equations:

$$\hat{a}|n\rangle = \sqrt{n}|n-1\rangle, \tag{2.10}$$
$$\hat{a}^\dagger|n\rangle = \sqrt{n+1}|n+1\rangle, \tag{2.11}$$
$$\hat{a}^\dagger\hat{a}|n\rangle = n|n\rangle, \tag{2.12}$$
$$|n\rangle = \frac{(\hat{a}^\dagger)^n}{\sqrt{n!}}|0\rangle. \tag{2.13}$$

As a transition from the discrete Fock picture to the continuous variable description to be used extensively later, let's see how the energy eigenstates of the electromagnetic field can be expressed as continuous wave equations. The first step to this effect is to introduce the so-called quadrature operators

$$\begin{cases} \hat{x} = \sqrt{\frac{\hbar}{2}}\left(\hat{a}^\dagger + \hat{a}\right), \\ \hat{p} = i\sqrt{\frac{\hbar}{2}}\left(\hat{a}^\dagger - \hat{a}\right). \end{cases} \tag{2.14}$$

Note that unlike the ladder operators $\hat{a}$ and $\hat{a}^\dagger$, the quadrature operators are Hermitian and therefore qualify as physical observables. We shall from now on refer to them as the position x and momentum p. A wave function corresponding to an arbitrary Fock state $|n\rangle$ can then be expressed in either basis $\{|x\rangle\}$ or $\{|p\rangle\}$ or any combination thereof $\hat{q}_\theta = \cos(\theta)\,\hat{x} + \sin(\theta)\,\hat{p}$. For example, the wave function of $|n\rangle$ in the position basis is given by

$$\begin{aligned} \varphi_n(x) &= \langle x|n\rangle \\ &= \frac{\mathrm{H}_n(x)}{\sqrt{2^n\sqrt{\pi}n!}}e^{-x^2/2}, \end{aligned} \tag{2.15}$$

where H_n is the n^{th} Hermite polynomial.

Up to now, we have only looked at pure states $|n\rangle$, which we can linearly combine to produce other pure states $\{\sum c_n|n\rangle : n \in \mathbb{N}, c_n \in \mathbb{C}\}$. It is precisely this coherent superposition of orthogonal states that lies at the heart of quantum mechanical behaviour. In real life, however, the coherence of the superposition is seldom maintained due to the plethora of couplings that can take place with the environment. Two orthogonal eigenstates $|n\rangle$ and $|m\rangle$ may not "co-exist" simultaneously; rather, either one or other—but not both—of them may be pre-existing for any experimental preparation of the system. This is illustrated in Fig. 2.1. With mixed states, therefore, the probability associated with any possible measurement outcome merely encapsulates our ignorance of the system, just as is customary in treatment of ensembles in statistical physics.

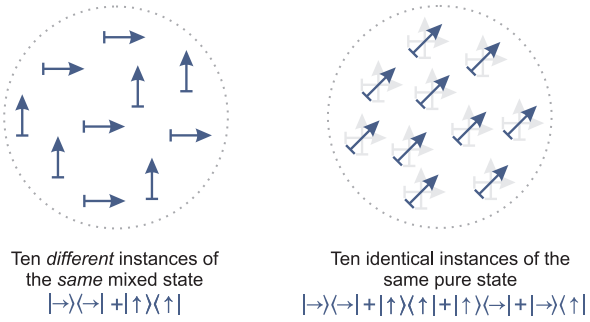

Figure 2.1: Illustration of the difference between coherent superpositions (pure states) and classical ensembles (mixed states) for ten preparations of the *same* state. The measurement of several mixed states is tantamount to picking out a different copy of either one of two states $\{|\uparrow\rangle, |\rightarrow\rangle\}$ from a classical "grab bag": Although the mixed state as a whole can be represented as a single density matrix, it in fact instantiates as *different* states. On the right, however, all instances of the pure state are objectively identical copies of a diagonal superposition $|\nearrow\rangle = \frac{1}{\sqrt{2}}(|\uparrow\rangle + |\rightarrow\rangle)$. It is only upon measurement in the orthogonal basis that the diagonal vector collapses—randomly—onto one of the basis states, thereby producing the same statistics as with a classical mixture.

The most general notation for quantum states, both pure and mixed, is the density matrix

$$\hat{\rho} = \sum_{n,m} c_{n,m} |n\rangle\langle m|, \tag{2.16}$$

which satisfies the following properties

$$\begin{aligned} \mathrm{Tr}\,\{\hat{\rho}\} &= 1, & (2.17)\\ \hat{\rho} &= \hat{\rho}^{\dagger}, & (2.18)\\ \langle u|\hat{\rho}|u\rangle &\geq 0,\ \forall |u\rangle \in \{|n\rangle\}\,. & (2.19) \end{aligned}$$

For practical purposes, we shall note that completely mixed states—i.e., those that possess no fixed quantum phase—the density matrix has no off-diagonal elements. If, in the example illustrated in Fig. 2.1, we use $\{|\uparrow\rangle, |\rightarrow\rangle\}$ as the basis of the Hilbert space, then we get that the mixed state is

$$\hat{\rho}_{\mathrm{mixed}} = \frac{1}{2}\left(|\uparrow\rangle\langle\uparrow| + |\rightarrow\rangle\langle\rightarrow|\right) = \frac{1}{2}\begin{bmatrix} 1 & 0 \\ 0 & 1 \end{bmatrix}, \tag{2.20}$$

whereas the pure state is

$$\hat{\rho}_{\text{pure}} = \frac{1}{2}\left(|\uparrow\rangle + e^{i\theta}|\rightarrow\rangle\right) = \frac{1}{2}\begin{bmatrix} 1 & e^{i\theta} \\ e^{-i\theta} & 1 \end{bmatrix}. \tag{2.21}$$

2.1.2 Wigner

Consider the mapping of an (algebraic) operator $\hat{A}$ to an (analytical) function $\tilde{A}$,

$$\tilde{A}(x,p) = \int e^{-ipy/\hbar}\langle x + y/2|\hat{A}|x - y/2\rangle \,\mathrm{d}y, \tag{2.22}$$

where the variables x and p are taken to be the canonical position and momentum, respectively. I.e, if $\hat{A}$ is a complex matrix expanded in the Fock basis as $\hat{A} = \sum_{n,m} A_{n,m}|n\rangle\langle m|$, then the bra-ket integrand in (2.22) unfolds as

$$\langle x + \tfrac{y}{2}|\hat{A}|x - \tfrac{y}{2}\rangle = \sum_{n,m} A_{n,m}\,\varphi_n\left(x + \frac{y}{2}\right)\varphi_m^*\left(x - \frac{y}{2}\right). \tag{2.23}$$

The continuous function $\tilde{A}(x,p)$ is called the Weyl transform of the operator $\hat{A}$. Though historically it arose from an attempt to reach a quantum operator from a classical function [5], its subsequent use turned out to be different. Not only did it offer an alternative description to the discrete Fock representation, but—more importantly—it allowed for a simultaneous visualization of the wave function in the position and momentum basis. As we shall see in a moment, this representation of quantum states bears some resemblance with classical phase space portraits and thereby offers a complete description of quantum states. In modern quantum mechanics, this phase space representation of a density matrix $\hat{\rho}$ is called the Wigner function $W(x,p)$ and is simply the Weyl transform of the matrix divided by Planck's constant,

$$\begin{aligned} W(x,p) &= \frac{1}{h}\tilde{\rho} \\ &= \frac{1}{h}\int e^{-ipy/\hbar}\langle x + y/2|\hat{\rho}|x - y/2\rangle \,\mathrm{d}y. \end{aligned} \tag{2.24}$$

One important property of the Weyl transform is that the quantum projection of an operator $\hat{A}$ onto another $\hat{B}$ can be re-written analytically as

$$\mathrm{Tr}[\hat{A}\hat{B}] = \frac{1}{h}\iint \tilde{A}(x,p)\tilde{B}(x,p)\,\mathrm{d}x\,\mathrm{d}p. \tag{2.25}$$

The relevance of the above product integral will become apparent in the next sections where it will serve as the mathematical blueprint for several physical

concepts such as projective measurements, fidelity, purity, and success rate. For now let's note that it can produce the expectation value of an observable $\hat{A}$ when used with the Wigner function of the quantum state $\hat{\rho}$, in complete analogy to the trace of the matrix product $\hat{\rho}\hat{A}$,[3]

$$\begin{aligned} \langle \hat{A} \rangle &= \mathrm{Tr}[\hat{\rho}\hat{A}] \\ &= \frac{1}{h} \iint \tilde{\rho}(x,p)\tilde{A}(x,p)\,\mathrm{d}x\,\mathrm{d}p \\ &= \iint W(x,p)\tilde{A}(x,p)\,\mathrm{d}x\,\mathrm{d}p. \end{aligned} \tag{2.26}$$

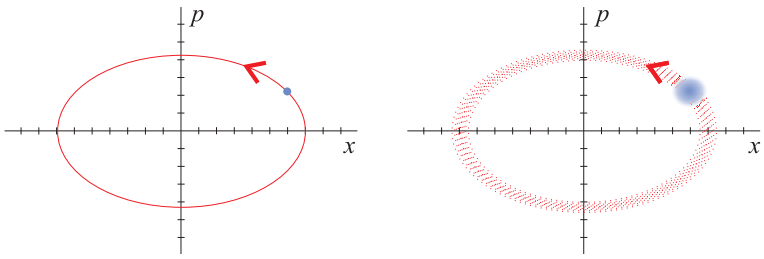

Figure 2.2: Comparison between the classical (left) and quantum (right) phase space representation of the harmonic oscillator. Classically, the particle is represented by a point coordinate traveling on a well-defined ellipse. Quantum mechanically, a coherent state consists of an ensemble of point-like particles traveling in unison in phase space. Their distribution is Gaussian and is guided by the same ellipse as that of a classical particle.

Now that we have defined the mathematics of the Wigner function, let's return to its interpretation as a phase space distribution. In classical mechanics, a particle of momentum p lying at position x is represented in phase space as a well-defined point. Its subsequent trajectory in phase space is entirely determined by its initial configuration, (x_0, p_0) and by the classical Hamiltonian governing its motion. This simple state of affairs does not carry over to quantum mechanics since, as prohibited by the uncertainty principle, conjugate variables cannot be well defined for any single particle.[4] A convenient imagery is then to consider not one particle, but an ensemble—or

[3] We assume for simplicity that the state $\hat{\rho}$ is normalized.

[4] Note that we are only referring to position and momentum as the conjugate canonical variables that arise from, say, the Harmonic oscillator. In quantum optics, these are simply the quadratures of the electromagnetic field, and do not have any kinematic meaning as in classical physics.

distribution—of particles spread over a continuous, albeit finite, area $\Delta x \Delta p$ of phase space (Fig. 2.2). Conceptually, the Wigner function lies somewhere between the complex wave function representation and the classical probability distribution given that, though entirely real, it can take on negative values that "encode" the interference of probability amplitudes [6]. In fact, the probability amplitude can be recovered directly from the Wigner function by projecting onto—i.e., integrating over—one of the quadratures. For example, the probability distribution of momentum is given by $\int W(x,p)\,\mathrm{d}x$; the probability for a particle to lie within a given interval $[x_a, x_b]$ is

$$P(x_a \leq x \leq x_b) = \int_{x_a}^{x_b} \int_{-\infty}^{\infty} W(x,p)\,\mathrm{d}p\,\mathrm{d}x. \tag{2.27}$$

2.2 States

This section will serve as a "photo album" of the states that constitute the staple of most quantum optics applications, namely, the Fock state, coherent state, and squeezed state. The first two are relevant because they constitute computational bases—i.e., alphabet spaces—for potential quantum information uses. We shall in particular discuss superpositions in those respective bases and how they are represented in the Wigner picture. Though rich in "quantumness", such superpositions are notoriously difficult to produce and characterize.[5] The third category, the squeezed state, is on the other hand a relatively easy resource to produce in a quantum optics laboratory and can be harnessed to emulate coherent state superpositions in the low intensity regime. We shall define the key attributes of these states and touch on the central concept of Gaussianity.

2.2.1 Fock state superposition

A recurring theme throughout this dissertation is the alternative visualization of quantum states in the two descriptions presented in the previous section. We shall in particular emphasize the conversion from the Fock to the Wigner representation. Recall that the density matrix is really just a linear combination of outer products, ket-bras, of general form $|n\rangle\langle m|$ where

[5] Characterization by means of tomography is always an easy "brute force" option provided we have several copies of the state. What is meant by difficult characterization, however, is when we only have a single copy of the state. Whereas a single interferometry or photon-counting measurement is enough to determine unambiguously states such as $|\gamma\rangle$ or $|n\rangle$, respectively, there does not exist simple setups to characterize even trivial superpositions such as $\frac{1}{\sqrt{2}}(|\gamma\rangle \pm |-\gamma\rangle)$ or $\frac{1}{\sqrt{2}}(|0\rangle \pm |1\rangle)$.

$n, m \in \mathbb{N}$. From Wigner's formula (2.24) and the definition of the x-wave function φ_n (2.15) we see that the Wigner term corresponding to the density matrix element $|n\rangle\langle m|$ is[6]

$$W_{|n\rangle\langle m|} = \frac{1}{h}\int_{\mathbb{R}} e^{-\frac{ipy}{\hbar}}\,\varphi_n\left(x+\frac{y}{2}\right)\varphi_m^*\left(x-\frac{y}{2}\right)\mathrm{d}y. \tag{2.28}$$

Note that contrary to a full-fledged Wigner function, the "Wigner elements" $W_{|n\rangle\langle m|}$ may or may not be real if $n \neq m$. Their computational advantage is that, just like matrix elements $|n\rangle\langle m|$, they add up linearly to form the overall state

$$\hat{\rho} = \sum_{n,m} \rho_{n,m}|n\rangle\langle m| \Leftrightarrow W_{\hat{\rho}} = \sum_{n,m} \rho_{n,m} W_{|n\rangle\langle m|}. \tag{2.29}$$

Two of the most trivial examples are the vacuum and the single photon,

$$W_{|0\rangle} = \frac{1}{\pi}e^{-x^2-p^2}, \text{ and} \tag{2.30}$$

$$W_{|1\rangle} = \frac{1}{\pi}e^{-x^2-p^2}\left(2x^2+2p^2-1\right). \tag{2.31}$$

We shall note that (i) only the vacuum has a Gaussian profile, (ii) all other states are non-Gaussian and exhibit a negative pseudo-probability at the origin, and (iii) no Fock state has any phase dependence (Fig. 2.3).

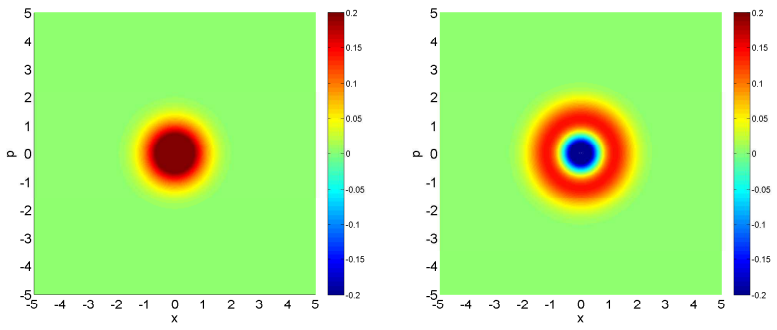

Figure 2.3: Wigner function of the vacuum $|0\rangle$ (left) and single photon $|1\rangle$ (right).

A more interesting case arises with superpositions of Fock states. Consider for example the state $c_1|n\rangle + c_2|m\rangle$ where $c_1, c_2 \in \mathbb{C}$. One cannot simply

[6] We shall from now take for granted the arguments (x, p) of the Wigner function. The latter shall therefore be simply written W as opposed to $W(x, p)$.

add the Wigner functions of the two pure terms $c_1 W_{|n\rangle} + c_2 W_{|m\rangle}$. Instead, all interference terms and their complex conjugates should be considered. This can only be done from the full density matrix expansion

$$\begin{aligned} c_1|n\rangle + c_2|m\rangle \quad &\equiv \quad |c_1|^2 \, |n\rangle\langle n| + c_1 c_2^* |n\rangle\langle m| + \\ &\qquad c_1^* c_2 |m\rangle\langle n| + |c_2|^2 \, |m\rangle\langle m|, \end{aligned} \tag{2.32}$$

thereby yielding

$$W = \frac{|c_1|^2 \, W_{|n\rangle\langle n|} + |c_2|^2 \, W_{|m\rangle\langle m|} + c_1 c_2^* W_{|n\rangle\langle m|} + c_1^* c_2 W_{|m\rangle\langle n|}}{|c_1|^2 + |c_2|^2 + c_1^* c_2 \langle n|m\rangle + c_1 c_2^* \langle m|n\rangle}, \tag{2.33}$$

where the denominator ensures the normalization of the Wigner function $\iint W \, \mathrm{d}x \, \mathrm{d}p \stackrel{!}{=} 1$. (More will be said later about this normalization condition and the information that can be extracted from non-normalized Wigner functions, namely the success probability of a given process.) As for the inner product of Fock states it is simply given by

$$\langle n|m\rangle = \delta_{n,m}. \tag{2.34}$$

A particular example of Fock state superposition we will be interested in is the vacuum-photon qubit,

$$|\psi_{\mathrm{qbit}}\rangle = \cos\phi|0\rangle + e^{i\theta} \sin\phi|1\rangle, \tag{2.35}$$

which can be thought of as a unit vector pointing along the polar coordinates (θ, ϕ) of the Bloch sphere, with the vacuum and single photon representing the north and south poles, respectively. Its Wigner function is given by

$$W_{|\psi_{\mathrm{qbit}}\rangle} = \frac{1}{\pi} e^{-x^2-p^2} \left(\cos(2\phi) + 2(x^2+p^2)\sin^2\phi + \sqrt{2}\sin(2\phi)(x\cos\theta - p\sin\theta) \right) \tag{2.36}$$

The special case $\phi = \frac{\pi}{4}$ is plotted in Fig. 2.4 for θ equalling π and 0.

2.2.2 Coherent state superposition

Recall the analogy between the classical and quantum harmonic oscillators in phase space (Fig. 2.2). We saw that no point-like state could exist in the quantum picture. Instead, one is bound to have continuous distributions of finite area $\Delta x \Delta p \geq \frac{1}{2}$. If this inequality is tight, and if furthermore the probability distribution is Gaussian, then we have a coherent state. This is the state whose behaviour is closest to that of a classical oscillator while

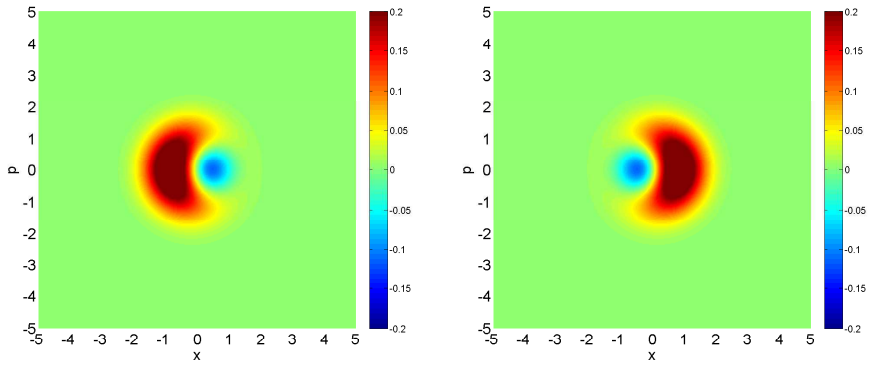

Figure 2.4: Wigner function of the Fock state superposition $\frac{1}{\sqrt{2}}(|0\rangle \pm |1\rangle)$. Unlike the the Fock states $|0\rangle$ and $|1\rangle$ taken individually, their superposition does have a phase dependence.

still abiding by Heisenberg's uncertainty principle. It is of ubiquitous use in quantum optics for several reasons. The first is that, for being a pure state, it carries with it valuable phase information which, combined with its potentially high luminosity (as opposed to individual Fock states), allows one to use it as a phase reference. In that case it is called a local oscillator and can be thought of a propagating ruler (or clock) with which other states can interfere, thereby revealing phase information. The second reason why coherent states are useful is that they can effectively form a computational basis in the limit of high intensity. Let's expand on this point with the formal definition of a coherent state in the Fock basis

$$|\gamma\rangle = e^{-\frac{1}{2}|\gamma|^2} \sum_{n=0}^{\infty} \frac{\gamma^n}{\sqrt{n!}} |n\rangle, \tag{2.37}$$

where $\gamma \in \mathbb{C}$.[7] A note of warning should be stated up-front regarding the orthogonality of coherent states. They only form an effective basis at high intensities γ because, unlike Fock states, they are not truly orthogonal as their inner product reads[8]

$$\langle \alpha | \beta \rangle \quad = \quad e^{-\frac{1}{2}|\alpha|^2 - \frac{1}{2}|\beta|^2 + \alpha^* \beta}. \tag{2.38}$$

[7]Note that both Fock states and coherent states are indicated with the Dirac notation. We shall distinguish the two bases by labeling Fock states with Roman letters and coherent states with Greek letters.

[8]We shall occasionally set $\hbar = 1$. Any time a numerical result is presented, this evaluation of Planck's constant is implied.

With the above in mind, we can go over the same reasoning as in §2.2.1 to convert any mixture of coherent states from the Dirac notation to the Wigner formalism. We start with the x-wave function

$$\begin{aligned}\varphi_\gamma(x) &= \langle x|\gamma\rangle \\ &= \pi^{-\frac{1}{4}} e^{-\frac{1}{2}\left(x-\sqrt{2}\Re\{\gamma\}\right)^2 + i\sqrt{2}\Im\{\gamma\}x - i\Re\{\gamma\}\Im\{\gamma\}},\end{aligned} \tag{2.39}$$

which we can then use in determining the Wigner term corresponding to any matrix element $|\alpha\rangle\langle\beta|$ in the coherent state basis

$$W_{|\alpha\rangle\langle\beta|} = \frac{1}{h}\int_{\mathbb{R}} e^{-\frac{ipy}{\hbar}}\,\varphi_\alpha\left(x+\frac{y}{2}\right)\varphi^*_\beta\left(x-\frac{y}{2}\right)\mathrm{d}y. \tag{2.40}$$

In particular, an arbitrary coherent state $|\gamma\rangle$ will be given by,

$$\begin{aligned}W_\gamma &= W_{|\gamma\rangle\langle\gamma|} \\ &= \frac{1}{\pi} e^{-x^2-p^2+2x\sqrt{2}\Re\{\gamma\}-2\Re\{\gamma\}^2+2p\sqrt{2}\Im\{\gamma\}-2\Im\{\gamma\}^2}.\end{aligned} \tag{2.41}$$

In the coherent state basis $\{|\gamma\rangle\}$, two examples of states which show no coherence are shown in Fig. 2.5, namely a single pure state and a mixture. Neither exhibits any negativity in the quasi-probability distribution that would indicate a quantum interference effect.[9]

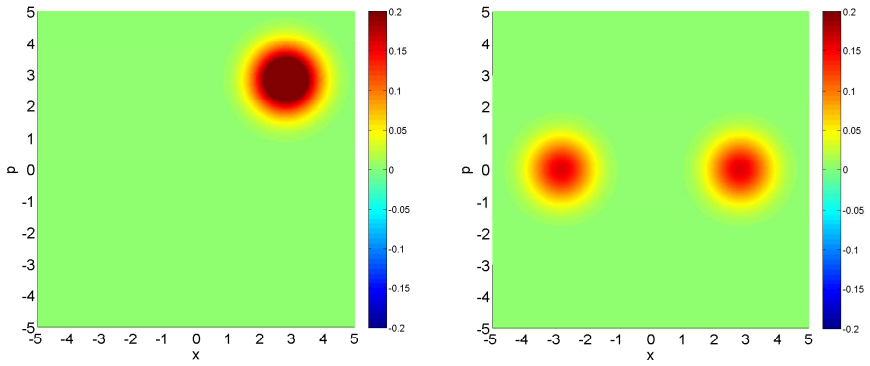

Figure 2.5: Coherent state of amplitude $\gamma = 2e^{i\pi/4}$ (left). Mixed state $\frac{1}{2}\left(|\gamma\rangle\langle\gamma| + |-\gamma\rangle\langle-\gamma|\right)$ for $\gamma = 2$ (right).

[9]Note that this is despite the fact that coherent states are actually coherent superpositions in the *Fock* basis.

Let's now move on to superpositions of coherent states. Just like we have put forth the vacuum-photon superposition (2.35) as a qubit, we can also conceive of superpositions of (pseudo-)orthogonal coherent states as qubits in an analogous Bloch sphere [7]. Such states shall be called cat states, in reference to Schödinger's cat, that is both dead and alive, the parallel drawn here is that the coherent state harmonic oscillator sways in two out-of-phase eigenstates simultaneously. In Dirac notation, a cat state of amplitude $\gamma \in \mathbb{C}$ shall be defined as

$$|\kappa_{\pm}(\gamma)\rangle = \frac{1}{\sqrt{2 \pm 2e^{-2|\gamma|^2}}} \left(|\gamma\rangle \pm |-\gamma\rangle\right), \tag{2.42}$$

where the sign $\pm$ indicates the even and odd cat, respectively (Fig. 2.6). More generally, any superposition $c_1|\alpha\rangle + c_2|\beta\rangle$ can be written in Wigner representation as

$$W = \frac{|c_1|^2 W_{|\alpha\rangle\langle\alpha|} + |c_2|^2 W_{|\beta\rangle\langle\beta|} + c_1 c_2^* W_{|\alpha\rangle\langle\beta|} + c_1^* c_2 W_{|\beta\rangle\langle\alpha|}}{|c_1|^2 + |c_2|^2 + c_1^* c_2 \langle\alpha|\beta\rangle + c_1 c_2^* \langle\beta|\alpha\rangle}. \tag{2.43}$$

The particular case of (2.42) is then given by

$$\begin{aligned} W_{\kappa_\pm}(\gamma) &= -\frac{e^{-x^2-p^2+2\sqrt{2}i\gamma p}}{2\pi\left(-e^{-2\gamma^2} \mp 1\right)} - \frac{e^{-x^2-p^2-2\sqrt{2}i\gamma p}}{2\pi\left(-e^{-2\gamma^2} \mp 1\right)} \qquad (2.44) \\ &\quad + \frac{e^{-x^2-p^2+2\sqrt{2}\gamma x-2\gamma^2}}{2\pi\left(-e^{-2\gamma^2} \mp 1\right)} + \frac{e^{-x^2-p^2-2\sqrt{2}\gamma x-2\gamma^2}}{2\pi\left(-e^{-2\gamma^2} \mp 1\right)} \\ &= \frac{e^{-x^2-p^2}}{\pi\left(e^{-2\gamma^2} \pm 1\right)} \left[\cos(2\sqrt{2}\gamma p) - e^{-2\gamma^2}\cosh(2\sqrt{2}\gamma x)\right]. \qquad (2.45) \end{aligned}$$

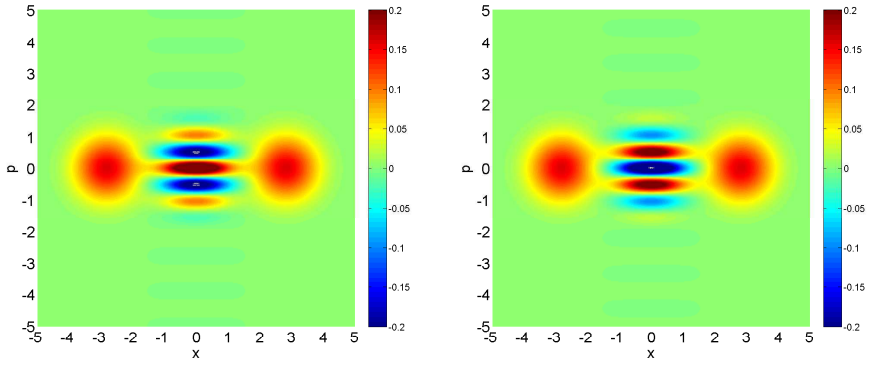

Figure 2.6: Even and odd cat of amplitude $\gamma = 2$.

A key point to retain from the above which we shall stress in the next sections is that every Wigner element $W_{|\alpha\rangle\langle\beta|}$ is Gaussian (though not necessarily real if $\alpha \neq \beta$). This property will turn out to be a computational advantage when, upon many integrals transforms involving Gaussian kernels (cf. (2.25) and §2.3.1), the integral outcome remains conveniently Gaussian. We shall come back to this point in greater detail in §2.5.

2.2.3 Squeezed state

Consider the classical harmonic oscillator whose phase portrait is plotted in Fig. 2.2 (left). We could exemplify this oscillator with an idealized case of Hooke's law involving a mass m attached to a spring of constant k and displaced from rest by x_0 on a friction-less horizontal surface. The total energy is given by $E_0 = \frac{1}{2}kx_0^2$ and the area of the ellipse traced in phase space is $A_0 = \pi x_0 p_0$ where x_0 and $p_0 = \sqrt{km}x_0^2$ represent the horizontal and vertical semi-axes, respectively. Because the motion is sinusoidal,[10]

$$\begin{cases} x(t) = x_0 \cos\left(\sqrt{\frac{k}{m}}t\right) \\ p(t) = \sqrt{km}\, x_0 \cos\left(\sqrt{\frac{k}{m}}t + \frac{\pi}{2}\right) \end{cases}, \tag{2.46}$$

the variance of position over an oscillation period $T = 2\pi\sqrt{\frac{m}{k}}$ is then

$$\begin{aligned} \mathcal{V}_x &= \frac{1}{T}\int_0^T (x(t))^2 \,\mathrm{d}t - \left(\frac{1}{T}\int_0^T x(t)\,\mathrm{d}t\right)^2 \\ &= \frac{1}{2}x_0^2, \end{aligned} \tag{2.47}$$

and similarly for momentum

$$\mathcal{V}_p = \frac{1}{2}kmx_0^2 = \frac{1}{2}p_0^2. \tag{2.48}$$

In other words, if we are to perform at any given time some stroboscopic measurement of either[11] position or momentum, it will turn out to be off by an of average $\sqrt{\mathcal{V}_x}$ or $\sqrt{\mathcal{V}_p}$ from its mean value of zero. Now imagine we

[10] These equations of motion can be easily shown to follow from the Hamiltonian $\mathcal{H} = \frac{1}{2m}p^2 + \frac{1}{2}kx^2$.

[11] This exclusive disjunction can be relaxed for the classical case, but let's maintain it for now for the sake of drawing the parallel with the non-commutativity in the quantum case.

need to have better control over the spread of position or momentum. What can we do such that their standard deviation is reduced (i.e., squeezed)? Given that the semi-axes of the ellipse are proportional to the standard deviation, the straightforward solution is have it narrowed and/or widened by multiplicative factors s_x and s_p as in

$$\begin{cases} x_0 \to x_0' = s_x x_0, \\ p_0 \to p_0' = s_p p_0 = s_p \sqrt{km} x_0. \end{cases} \tag{2.49}$$

If we assume the mass m to be constant, the transformation (2.49) can be implemented by multiplying the release position x_0 by s_x and the spring constant by s_p^2. For example, if we halve the release position and quadruple the spring constant, then the position distribution over any oscillation period is halved at the expense of a doubled "uncertainty" in momentum.

Let's now introduce the additional requirement that the squeezing process conserves the total energy. This will later be referred to as *pure* squeezing and represents a wide class of quantum optical transformations referred to as passive (cf. §2.3.1). The energy transformed by (2.49) is

$$E_0 \to E_0' = \frac{1}{2} k' x_0'^2 = \frac{1}{2}(k s_p^2)(s_x x_0)^2 = (s_x s_p)^2 E_0, \tag{2.50}$$

which, under a conservative process $E_0' = E_0$ implies that $s_x s_p = 1$. (We assume that s_x and s_p are positive—any negative values they could take on would anyhow merely reflect a phase delay.) Pure squeezing therefore enforces a trade-off in the uncertainties of the canonical coordinates: A squeezed—i.e., narrower—spread in position entails a commensurately heightened uncertainty—i.e., anti-squeezing—in momentum, and vice versa. (Very often we will refer to the overall process as squeezing, keeping in mind that it always involves both squeezing proper and anti-squeezing.)

Topologically, energy conservation $E_0' = E_0$ translates into an area conservation $A_0' = A_0$ of the ellipse in phase space. This will be touched on more formally with references to Liouville's theorem in §2.3.1. For now it can be easily verified from (2.49) and the requirement that $s_x s_p = 1$,

$$A_0 \to A_0' = \pi(s_x x_0)(s_p p_0) = \{s_x s_p = 1\} = A_0. \tag{2.51}$$

Though somewhat lengthy, the classical digression above makes it easier to grasp the concept of squeezing. In quantum optics, instead of adjusting x_0 and k, we shape the phase portrait of our "electromagnetic pendulum" via nonlinear interactions within a crystal. This is discussed in §6.2; for the time

being, we shall only go through the "kinematics" of squeezing and lay out its main parameters. We shall in particular restrict ourselves to the squeezing of vacuum (cf. Fig. 2.3 left). In view of Heisenberg's uncertainty principle, this implies that instead of referring to a sharply defined (hollow) ellipse, the squeezing will be applied to a two-dimensional Gaussian distribution characterized by the variance of vacuum, which we know from (2.30) to be[12]

$$\begin{aligned} \mathcal{V}_0 &= \iint_{\mathbb{R}} x^2 W_{|0\rangle}\, \mathrm{d}x\, \mathrm{d}p \\ &= \iint_{\mathbb{R}} x^2 \frac{1}{\pi} e^{-x^2-p^2}\, \mathrm{d}x\, \mathrm{d}p \\ &= \frac{1}{2}. \end{aligned} \tag{2.52}$$

In order to mold the phase space distribution into a Gaussian of variance $\mathcal{V}_x$ and $\mathcal{V}_p$, the quadratures need to be re-scaled by ratio of the desired standard deviation with that of the vacuum

$$s_x = \sqrt{\frac{\mathcal{V}_x}{\mathcal{V}_0}}, \text{ and } s_p = \sqrt{\frac{\mathcal{V}_p}{\mathcal{V}_0}}. \tag{2.53}$$

(We are looking at the square root of variance because, by dimensional analysis, quadratures are linear to the standard deviation.) In experimental quantum optics, it is more customary to expressed squeezing in decibels with respect to the vacuum variance , the latter of which is called shot noise. The squeezing ξ_q in decibels along a quadrature q is thus given by

$$\xi_q = 10 \log_{10} \frac{\mathcal{V}_q}{\mathcal{V}_0} = 20 \log_{10} s_q \Leftrightarrow s_q = 10^{\xi_q/20}. \tag{2.54}$$

For the sake of completeness we shall introduce a third variable to quantify squeezing that is equivalent to s and ξ, but usually contains the actual physical constants underpinning the squeezing process, namely the interaction time t and the non-linearity strength χ of the crystal. We will come back to this in §§2.3.1 and 6.2. For now, let's relate it to the dimensionless quadrature rescaling factor by

$$s = e^r, \tag{2.55}$$

where $r \propto \chi t$.

[12]Here, we are looking at the variance in the x direction, but because of the symmetry of the vacuum Wigner function a similar variance is obtained along p. We have also omitted to subtract the mean as it clearly is zero.

Purity of squeezing

As mentioned above, the purity of squeezing can be related to the trade-off in uncertainty between conjugate canonical variables. When this trade-off is tight, i.e., when the overall uncertainty is minimized to satisfy $\mathcal{V}_x\mathcal{V}_p = \mathcal{V}_0^2$, the squeezing is considered pure. Any departure from this condition implies that external information (i.e., noise) has filtered through the system via de-coherence. (To return to the classical analogy of a Hooke's law, it's as if an external driving force were applied to the mass and therefore the mass-spring system is not isolated anymore.)

As we shall motivate in §2.6, the purity of a state of Wigner function W is

$$\mathcal{P} = 2\pi \iint W^2 \,\mathrm{d}x\mathrm{d}p, \tag{2.56}$$

and the Wigner function of a squeezed vacuum state $\hat{S}|0\rangle$ is

$$W_{\hat{S}|0\rangle}(x,p) = \frac{1}{\pi s_x s_p} e^{-(x/s_x)^2-(p/s_p)^2}. \tag{2.57}$$

The purity of squeezed vacuum can therefore be shown to be

$$\mathcal{P} = \frac{1}{s_x s_p} = 10^{-\frac{1}{20}(\xi_x+\xi_p)}. \tag{2.58}$$

2.3 Operations

"*Information is physical.*" This aphorism, owed to Rolf Landauer [8], summarizes the correspondence between information theory and physical systems. Just like information can be stored, processed, and output, so can physical observables be prepared, operated on by a series of Hamiltonians, and measured.[13] We have discussed the storage, or encoding, of information into physical states in the previous section. We shall now look at what can be done to physical states so that they take on a new piece of information and how that newly processed information can be read out. Let's start by illustrating this point with a very sketchy example from classical mechanics. Assume that the initial information, the input, is encoded in the position-momentum pair (x, p) of some marble of mass m and initial velocity v_0,

[13] In addition to this formal similitude between information and physical systems, there remains the semi-philosophical question as to whether information can conceivably exist outside any physical encoding, or conversely—and of higher relevance to the interpretation of quantum mechanics—whether a physical system can objectively *not* contain any predefined information before measurement.

traveling on a flat friction-less path. We are not being specific about how this alphabet—in the computer science sense of the term—is used, but simply state that any pair (x, p) can be used to store information. We want to process this initial information (x, p) into the output (x', p'), namely into the "answer" of the computation. This transformation can be represented by a mathematical function f

$$(x, p) \to (x', p') = f(x, p). \tag{2.59}$$

If, for example, the correct output of the computation consists of x and p oscillating out of phase of one another at frequency ω, then a harmonic potential $V \propto \omega x^2$ would offer the ideal physical operator corresponding to the function f. This is shown in Fig. 2.7.

One can thus see that mathematical computations f, once transposed in the physical world, are simply Hamiltonians acting on a given system. As a consequence, the trajectory of the particle in phase space is redirected along a new path. In the example under consideration, it transforms a straight line into a closed elliptical loop. As we shall see throughout this dissertation, the "name of the game" in continuous variable quantum information is to devise operations that reshape input phase space distributions into new ones according to a given algorithm. This brings us to discuss quantum systems. They, too can be used to process information with the added advantage that the superposition principle permits to solve problems intractable with the procedural steps of classical mechanics. The major difference is that, unlike the point-like marble of Fig. 2.7, quantum objects can only exists as one or more probability clusters flowing about in phase space. The rest of the analogy regarding the nature of physical information processing remains however unchanged. The encoded information—now stored in qubits—can be processed through several Hamiltonian operators which then mold the phase space distribution into an output state.

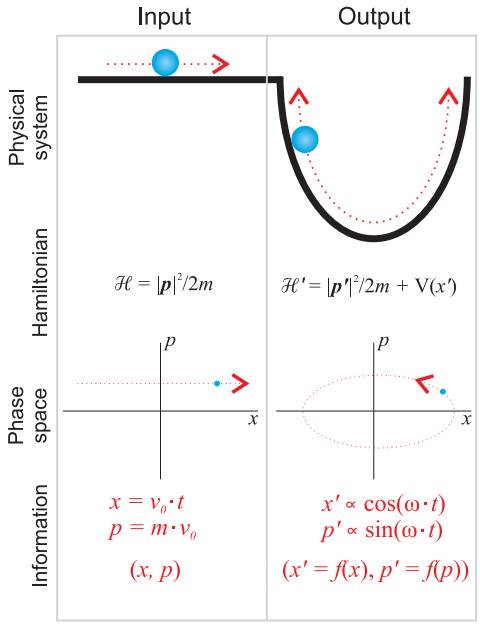

Figure 2.7: Information is physical. Here, x and p represent the linear position along the friction-less path. The trajectories in configuration- and phase-space are traced by the dotted red line, with the arrow indicating the direction of time. The marble at any given point is shown in blue.

2.3.1 Canonical transformations

We shall now introduce the simplest class of computations, namely linear transformations of the type

$$f : \vec{q} \to \ \mathbf{A}\vec{q} + \delta\vec{q}, \tag{2.60}$$

where $\vec{q}$ is a position-momentum pair $(x, p)^{\mathrm{T}}$, $\mathbf{A}$ is a constant 2×2 matrix, and $\delta\vec{q}$ is a constant 2×1 vector. In the particular case where $\delta\vec{q} = 0$ and $\mathbf{A} \in \mathrm{SU}(2)$, the physical system neither dissipates to nor receives any energy from the environment, and thereby retains the entirety of its information content. Mappings of the type (2.60) are one-to-one, reversible, and are therefore called canonical transformations, in reference to form-invariant systems in Hamiltonian mechanics. As we shall see in a while, they model a wide array of optical elements alternatively called passive, Gaussian, or more generally, *linear*.

One can recall from Hamiltonian mechanics that canonical transformation are really just coordinate transformations in phase space. Let's di-

gress for a while to illustrate a basic example of coordinate transformation that belongs to the SU(2) group, namely the rotation operation of a vector $\vec{v} = (v_1, v_2)^{\mathrm{T}}$ by an angle θ,

$$\begin{bmatrix} v_1 \\ v_2 \end{bmatrix} \rightarrow \begin{bmatrix} \cos\theta & -\sin\theta \\ \sin\theta & \cos\theta \end{bmatrix} \begin{bmatrix} v_1 \\ v_2 \end{bmatrix}, \tag{2.61}$$

where the "output" vector

$$\vec{v'} = \begin{bmatrix} \cos(\theta)v_1 - \sin(\theta)v_2 \\ \sin(\theta)v_1 + \cos(\theta)v_2 \end{bmatrix} \tag{2.62}$$

has has the same norm as that of the input $|\vec{v}| = |\vec{v'}|$, thereby indicating the energy-conserving property of the transformation. The crucial point to be retained from this example is that the rotation (our computation) can be modeled either by rotating the vector (our information) by θ or by rotating the coordinate space (our "alphabet space") by $-\theta$ while leaving the vector unchanged (left column of Fig. 2.8).

Let's return to continuous variable quantum optics, for which the Wigner function is established as the most appropriate representation. For being an analytical function, the Wigner distribution belongs to a different domain than that of density matrices. The two nonetheless satisfy a one-to-one correspondence via Weyl's transform (2.22). This correspondence extends to transformations. For example, the transformation of a quantum state $\hat{\rho}$

$$\hat{\rho} \rightarrow \hat{U}^{\dagger}\hat{\rho}\hat{U} \tag{2.63}$$

translates in Wigner notation to an integral transform [9, 10]

$$W(x,p) \rightarrow \tilde{W}(x,p) = \iint_{\mathbb{R}} K(x',p') \cdot W(x',p')\,\mathrm{d}x'\mathrm{d}p' \tag{2.64}$$

where K is a transformation function, also known as a kernel.[14] The kernel is independent of the initial and final states of the system, but encompasses instead all its dynamical properties.

As is illustrated in the left column of Fig. 2.8, it turns out that for systems whose Hamiltonian is at most quadratic in the ladder operators a canonical transformation suffices, rather than a full blown integral transform. One only needs to transform the phase space coordinates while leaving the Wigner function "unchanged" and then renaming the new function in

[14] The most common example of integral transforms is the Fourier transform.

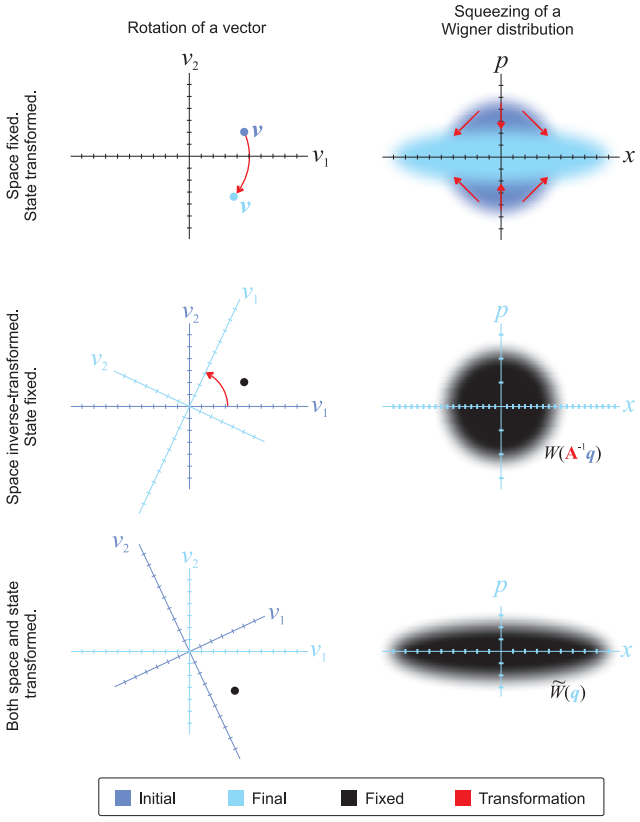

Figure 2.8: Illustration of a canonical transformation in phase space (right column) by analogy to a simple transformation in vector space, namely a rotation (left column). Whereas the information on the left is encoded as a point in vector space $[v_1, v_2]$, it is encoded on the right as a probability distribution W in a phase space $[x, p]$. The transformation under consideration is that of a pure squeezing in the p quadrature. In the first row, the information processing is performed in one step, which would entail an integral transform for the Wigner function. The message to be conveyed is that this can be simplified into two algebraic steps where only phase space is re-scaled while maintaining the function unchanged. Please be aware that we have only represented the Wigner function as a flat disk while in reality it is a continuous distribution of finite volume pervading phase space to infinity. We shall assume for this example that it has Gaussian cross sections in both quadratures and that the disk merely delineates its surface lying above a given threshold.

the re-scaled space as our final function in the old space. I.e., the first row of Fig. 2.8 is tantamount to the second row followed by the third. The transformation thus reads

$$W(\vec{q}) \to W(\mathbf{A}^{-1}\vec{q}) = \tilde{W}(\vec{q}). \tag{2.65}$$

Note that coordinates undergo the inverse transformation to that applied to the function.

It should be said that (2.60) is a special case of the broader set of Bogoliubov transformations acting on M modes,

$$\hat{a}_i' = \sum_{j=1}^{M} A_{ij}\hat{a}_j + B_{ij}\hat{a}_j^\dagger + \gamma_i, \tag{2.66}$$

where A and B satisfy $AB^{\mathrm{T}} = \left(AB^{\mathrm{T}}\right)^{\mathrm{T}}$ and $AA^\dagger = BB^\dagger + \hat{\mathbb{I}}$ so as to abide by the bosonic commutation relation [11]. A Bogoliubov transformation can describe any combination of Hamiltonians that are quadratic in the ladder operators.

The time is now ripe to work out from scratch an example of canonical transformations from an actual Hamiltonian. We shall look at the squeezing operation. For this we use a non-linear crystal as a transducer between an exciting mode $\hat{a}_p$ of frequency 2ω, the pump, and two indistinguishable modes $\hat{a}_s$ and $\hat{a}_i$ of frequency ω each, referred to as the signal and idler. We will elaborate on this in Sec. 6.2; but for now we shall retain that energy is transferred from the pump into the signal-idler pair via the crystal, while—naturally—satisfying energy and momentum conservation. Quantum mechanically we therefore remove an excitation from the pump with $\hat{a}_p$ to transfer it to both the signal and idler with $\hat{a}_p^\dagger$ and $\hat{a}_i^\dagger$. For the sake of reversibility, we also need to add the complex conjugate of the process. The interaction Hamiltonian thus reads

$$\hat{\mathcal{H}} \propto i\hbar\chi^{(2)}\left(\hat{a}_p\hat{a}_s^\dagger\hat{a}_i^\dagger - \hat{a}_p^\dagger\hat{a}_s\hat{a}_i\right). \tag{2.67}$$

We shall further make two simplifications. First, we shall approximate the pump to be so strong as to traverse the nonlinear medium virtually undepleted. This allows us to treat it as a classical reservoir of energy and thus lift the requirement to have it modeled as a quantum operator. We can thus apply the so-called parametric approximation: $\hat{a}_p \approx \alpha_p = |\alpha_p|\, e^{i\Theta}$ [12]. The second simplification consists of looking only at the degenerate

case $\hat{a}_s = \hat{a}_p = \hat{a}$ so that two identical photons emerge from a single pump photon of double the frequency. The Hamiltonian becomes

$$\hat{\mathcal{H}} = i\hbar\frac{\kappa}{2}\left(\left(\hat{a}^\dagger\right)^2 e^{i\Theta} - \hat{a}^2 e^{-i\Theta}\right), \tag{2.68}$$

where we have bundled the pump amplitude and the non-linearity of the crystal into a single coupling term κ.

Setting the macroscopic pump phase to zero $\Theta = 0$, the Heisenberg equation,

$$\frac{\mathrm{d}}{\mathrm{d}t}\hat{a}(t) = \frac{1}{i\hbar}\left[\hat{a}(t), \hat{\mathcal{H}}\right] = \kappa\hat{a}^\dagger(t), \tag{2.69}$$

where we have used the commutation relation $[\hat{a}, \hat{a}^\dagger] = 1$, can be shown to be solved by

$$\hat{a}(t) = \hat{a}(0)\cosh(\kappa t) + \hat{a}^\dagger(0)\sinh(\kappa t). \tag{2.70}$$

The interaction time is labeled by t. Converting the ladder operators into the quadrature operators via (2.14), we finally get the canonical transformation of degenerate squeezing,

$$\begin{bmatrix} x_{\mathrm{out}} \\ p_{\mathrm{out}} \end{bmatrix} = \begin{bmatrix} e^{+r} & 0 \\ 0 & e^{-r} \end{bmatrix} \begin{bmatrix} x_{\mathrm{in}} \\ p_{\mathrm{in}} \end{bmatrix}, \tag{2.71}$$

where $r = \kappa t$ is the squeezing gain. One can clearly see that squeezing is tantamount to stretching the phase space plane in the position direction by e^{+r} while shrinking it in the momentum direction by e^{-r}.

Thanks to the linearity of (2.60), and more generally of Bogoliubov transformations, the serial application of a quadratic Hamiltonians on an initial state can be modeled by a convenient cascade of matrix multiplications and—in the case of coherent displacement—of vector additions. This is illustrated in Fig. 2.9 for the case of a proof-of-principle Hadamard gate in the coherent state basis which makes use of a degenerate single-mode squeezer, a displacement operator, and three beam splitters [13]. (The final part of the operation, the measurements will be discussed in the following sections.)

A reference list of quadratic interaction Hamiltonians and their ensuing canonical transformations is provided in Table 2.2. As can be seen, such transformations need not act on a single mode only, but on any number of modes M such that the vector $\vec{q}$ in (2.60) be of length $2M$.

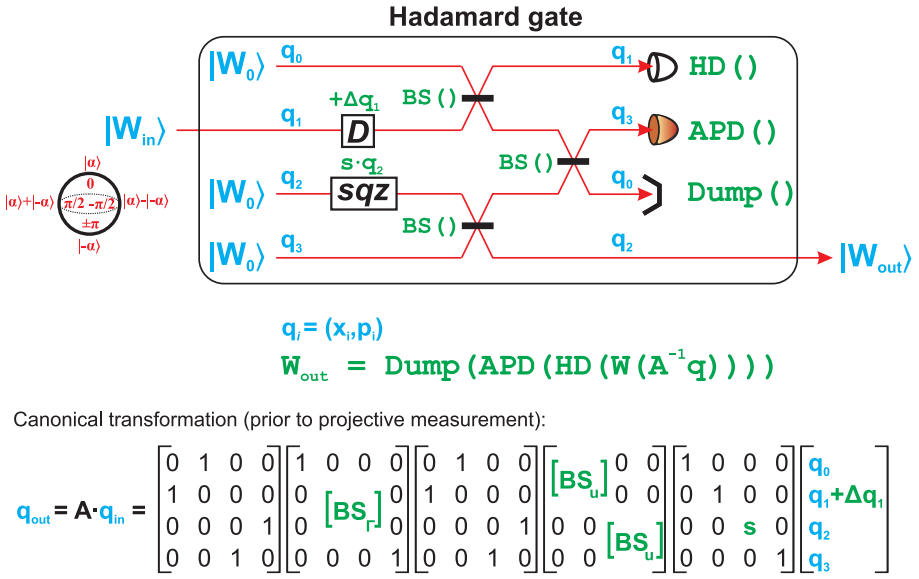

Figure 2.9: *Top*: Circuit of a proof-of-principle Hadamard gate in the coherent state superposition basis [13]. The states (W) and modes (q) are in blue and operations are in green. *Bottom*: Canonical transformation of the quadrature coordinates corresponding to the linear part of the circuit. Note the use of permutation matrices to keep track of the right modes.

Table 2.2: Linear canonical transformations of quadrature bases

Operation	Hamiltonian	Transformation
Phase shift	$\hbar\phi\hat{a}^\dagger\hat{a}/t$	$\begin{bmatrix} \cos\phi & \sin\phi \\ -\sin\phi & \cos\phi \end{bmatrix} \begin{bmatrix} x_{\text{in}} \\ p_{\text{in}} \end{bmatrix}$
Coherent displacement	$i\hbar(\alpha\hat{a}^\dagger - \alpha^*\hat{a})$	$\begin{bmatrix} 1 & 0 \\ 0 & 1 \end{bmatrix} \begin{bmatrix} x_{\text{in}} \\ p_{\text{in}} \end{bmatrix} + \begin{bmatrix} \delta x \\ \delta p \end{bmatrix}$
Single-mode squeezer	$i\hbar\chi\left(\hat{a}^2 - (\hat{a}^\dagger)^2\right)/2$	$\begin{bmatrix} s & 0 \\ 0 & \frac{1}{s} \end{bmatrix} \begin{bmatrix} x_{\text{in}} \\ p_{\text{in}} \end{bmatrix}$
Tow-mode squeezer	$i\hbar\chi\left(\hat{a}_i\hat{a}_s - \hat{a}_i^\dagger\hat{a}_s^\dagger\right)/2$	$\begin{bmatrix} \cosh r & 0 & -\sinh r & 0 \\ 0 & \cosh r & 0 & \sinh r \\ -\sinh r & 0 & \cosh r & 0 \\ 0 & \sinh r & 0 & \cosh r \end{bmatrix} \begin{bmatrix} x_{s,\text{in}} \\ p_{s,\text{in}} \\ x_{i,\text{in}} \\ p_{i,\text{in}} \end{bmatrix}$
Beam splitter	$i\hbar\kappa_l\left(\hat{a}_2^\dagger\hat{a}_1 - \hat{a}_1^\dagger\hat{a}_2\right)/2$	$\begin{bmatrix} \sqrt{T} & 0 & \sqrt{1-T} & 0 \\ 0 & \sqrt{T} & 0 & \sqrt{1-T} \\ -\sqrt{1-T} & 0 & \sqrt{T} & 0 \\ 0 & -\sqrt{1-T} & 0 & \sqrt{T} \end{bmatrix} \begin{bmatrix} x_{1,\text{in}} \\ p_{1,\text{in}} \\ x_{2,\text{in}} \\ p_{2,\text{in}} \end{bmatrix}$
Quantum non-demolition	$\hbar\kappa_q\hat{x}_1\hat{p}_2$	$\begin{bmatrix} 1 & 0 & 0 & 0 \\ 0 & 1 & 0 & -G \\ G & 0 & 1 & 0 \\ 0 & 0 & 0 & 1 \end{bmatrix} \begin{bmatrix} x_{1,\text{in}} \\ p_{1,\text{in}} \\ x_{2,\text{in}} \\ p_{2,\text{in}} \end{bmatrix}$

s is the quadrature rescaling parameter given by $s = e^r$ where $r = \kappa t$.
$T \in [0, 1]$ is the beam splitter transmission and is given by $T = \cos^2(\kappa_l t)$ where κ_l is the linear coupling constant
$G = \kappa_q t$ is the nonlinear interaction gain.

We shall conclude this subsection with a qualitative discussion of Liouville's theorem. Recall that in classical mechanics, Liouville's theorem states that a statistical ensemble of particles whose motion is governed by the same dynamics evolve in phase space as a probability distribution whose density is conserved. The probability density thus behaves as an "incompressible fluid" in phase space [9]. The same is true in quantum mechanics where no process can ever compress the Wigner function into an area smaller than the minimum $\Delta x \Delta p$ specified by Heisenberg's uncertainty relation. Furthermore, no linear process—as expressed by Bogoliubov transforms—can turn a Gaussian Wigner function into a non-Gaussian one, hence the alternative appellation of linear processes as Gaussian processes.

2.3.2 The generic projection: A mathematical blueprint

Recall property (2.25) involving two operators $\hat{A}$ and $\hat{B}$,

$$\mathrm{Tr}[\hat{A}\hat{B}] = \frac{1}{h} \iint \tilde{A}(x,p)\tilde{B}(x,p)\,\mathrm{d}x\,\mathrm{d}p, \tag{2.72}$$

where $\tilde{A}$ and $\tilde{B}$ are the Weyl transforms of $\hat{A}$ and $\hat{B}$. We stated that the above represents the mathematical blueprint for several concepts such as measurement operations, fidelity, purity, and success probability. More generally, it can be thought of as a projection, or "similarity measure", between two quantum objects A and B expressed either in the discrete basis (on the left-hand side) or continuous basis (on the right hand-side). Special cases of (2.72) are straightforward bra-ket inner products $\langle\psi_\mathrm{A}|\psi_\mathrm{B}\rangle$ between two pure states $|\psi_\mathrm{A}\rangle$ and $|\psi_\mathrm{B}\rangle$. More general scenarios are summarized in Table 2.3. Particular emphasis on the continuous-variable implementation of (2.72) will be made in §2.5.

A	B	Interpretation of (2.72)
Any pure quantum state	Any quantum state	Fidelity
Any pure quantum state	$B = A$	Purity
Any quantum state	Any measurement operator	Success probability

Table 2.3: Three different interpretations of Eq. (2.72). Note that if A spans more modes than B, then the success probability is given by normalizing the state living in the remaining modes. Eq. (2.72) thereby also produces the output of the measurement. It is interesting to note that mathematically, the nature of A and B as either quantum states or measurement operators is irrelevant: They are nothing more than density matrices to be compared.

2.3.3 Homodyne measurement

A homodyne measurement corresponds to a projection on a given quadrature $|q_0\rangle\langle q_0|$ where $|q_0\rangle = \cos\theta|x_0\rangle + \sin\theta|p_0\rangle$. This projector, when applied to a state whose Wigner function is $W(x,p)$, "picks out" the cross-section along q_0 to yield a probability density. Such a projection is given in the quadrature basis by

$$\hat{\Pi}_{\mathrm{HD}}(q_0) = |q_0\rangle\langle q_0|, \tag{2.73}$$

which, in the Wigner representation would most appropriately be given by the Dirac delta function

$$W_{\mathrm{HD}}(q_0) = \delta(q - q_0). \tag{2.74}$$

If we choose for simplicity that $q_0 = x_0$, then the projection operation (2.96) onto some state $W(x,p)$ yields

$$\begin{aligned} & \iint_{\mathbb{R}} W(x,p) \cdot \; W_{\mathrm{HD}}(q_0)\,\mathrm{d}x\,\mathrm{d}p \\ = & \iint_{\mathbb{R}} W(x,p)\cdot\delta(x-x_0)\,\mathrm{d}x\,\mathrm{d}p \\ = & \; W(x_0,p) \\ = & \; P(x_0). \end{aligned} \tag{2.75}$$

Intuitively, the probability of measuring exactly the quadrature q_0 should be vanishingly small. Yet, $P(x_0)$ has a finite value since it is a probability *density*. To model the more realistic scenario where homodyne detection has a given resolution bandwidth Δq around the measured value q_0, an interval projector is more appropriate

$$\hat{\Pi}_{\mathrm{HD}}(q_0,\Delta q) = \int_{q_0-\frac{\Delta q}{2}}^{q_0+\frac{\Delta q}{2}} |q\rangle\langle q|\,\mathrm{d}q \tag{2.76}$$

or, in Wigner representation

$$\begin{aligned} & W_{\mathrm{HD}}(q_0,\Delta q) \\ = & \; \frac{1}{2\pi}\int_{q_0-\frac{\Delta q}{2}}^{q_0+\frac{\Delta q}{2}} \delta(q-q')\,\mathrm{d}q' \\ = & \; \frac{1}{2\pi}\left[\Theta\left(q-q_0+\frac{1}{2}\Delta q\right) - \Theta\left(q-q_0-\frac{1}{2}\Delta q\right)\right], \end{aligned} \tag{2.77}$$

where Θ is the Heaviside step function. Note how (2.77) does not fit the Gaussian form of (2.87). For calculational ease, the wide homodyning operation is therefore best performed last so as to maintain the convenient Gaussianity of the quantum states as long as possible.

In the limiting case of ideal homodyning, $\Delta Q \to 0$, we expect (2.74) and (2.77) to yield the same result.

2.3.4 Photon-number measurement

Just like homodyne detectors are the main measurement device for CV quantum optics, DV quantum optics is most naturally probed by detectors whose eigenvalues match those of the photon number operator $\hat{n}$. A photon number resolving detector (PNR) returns a discrete current that is proportional to the number of photons n impinging on it. Mathematically, it is represented by

$$\hat{\Pi}_{\hat{n}} = |n\rangle\langle n| \tag{2.78}$$

In practice, PNRs are not only expensive and difficult to operate but they also have an upper bound $n_{\max}$ on the photon numbers they can resolve [14, 15]. A simpler device, is the avalanche photo diode (APD) which only offers a binary output: Either it clicks if at least one photon impinges on it, or it does not click at all. These two events are modeled by the projectors

$$\hat{\Pi}_1 = \sum_{n=1}^{\infty} |n\rangle\langle n| = \hat{\mathbb{I}} - |0\rangle\langle 0| \tag{2.79}$$

and

$$\hat{\Pi}_0 = |0\rangle\langle 0|, \tag{2.80}$$

respectively.

2.3.5 Adaptive feedback measurement

Whereas homodyne and photon-number measurements are projections onto fixed bases, adaptive feedback measurements project onto a "movable basis" whose orientation in Fock or phase space is continuously adjusted to better probe the incoming state as it gradually collapses. Adaptive feedback techniques are primarily useful to determine the *a priori* unknown phase of a quantum state. The overall procedure consists of distributing the state into multiple spatial or temporal modes which are then collapsed in sequence with measurements settings depending on the history of outcomes. In other words, adaptive feedback measurements can be thought of as a series of

weak measurements on the whole system or, alternatively, as a series of von Neumann projections onto fractions it (Fig. 2.10). After each weak (or subsystem) measurement, the system reveals a tiny piece of information about the desired observable, typically the phase. This infinitesimal information is fed back to the detection apparatus so as to rotate the measurement basis in a direction which is optimally aligned with the orientation of the remaining part of the incoming state vector. This re-alignment procedure could consist, for example, of adjusting the phase of a local oscillator in a homodyne setup, thereby rotating the projection quadrature, or—alternatively—of displacing a coherent state so as to overlap it with the vacuum.

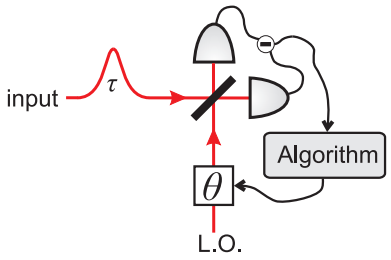

Figure 2.10: An adaptive feedback measurement, as the one sketched here, is essentially a homodyne measurement with a phase for the local oscillator which is adjusted on the fly to better probe the incoming state. By stretching the state in time domain to a lenght τ longer than the response delay of the detector, a series of weak measurement can be performed to feedback the appropriate phase θ of the local oscillator given a pre-defined algorithm.

Although adaptive feedback is a powerful technique to estimate the phase of a system for which no prior information is available, it may not necessarily outperform other techniques (e.g. homodyning) when a given projection basis is known to be privileged. This will be further elaborated in §2.4 in the context of qubit phase measurement.

2.4 Qubit operations

In this section, we shall confine our attention to two-level quantum systems and, in particular, attempt the characterization of generic qubits of the form

$$|\psi_{\varphi,\phi}\rangle = \cos\left(\frac{\varphi}{2}\right)|0\rangle + \sin\left(\frac{\varphi}{2}\right)e^{i\phi}|1\rangle, \tag{2.81}$$

where $\varphi \in [0, \pi]$ and $\phi \in [0, 2\pi)$ are the polar and azimuthal angles, respectively, of the Bloch sphere. As we shall see in chapters 4 and 3, the characterization of such qubits is required to perform Bell measurements in the two-dimensional Fock Hilbert space spanned by $\{|0\rangle, |1\rangle\}$.

Qubit projections

To characterize a qubit $\hat{\varrho}_{\varphi,\,\phi} = |\psi_{\varphi,\,\phi}\rangle\langle\psi_{\varphi,\,\phi}|$, one needs to devise a projector $\hat{\Pi}$ such that the probability of successfully projecting $\hat{\varrho}_{\varphi,\,\phi}$ onto $\hat{\Pi}$ is

$$P(\varphi, \phi) = \frac{\mathrm{Tr}\left\{\hat{\varrho}_{\varphi,\,\phi}\hat{\Pi}\right\}}{\mathrm{Tr}\left\{\hat{\varrho}_{\varphi,\,\phi}\right\}}. \tag{2.82}$$

Ideally, this probability is unity if $\hat{\varrho}_{\varphi,\,\phi}$ and $\hat{\Pi}$ are equal (up to a global phase factor) and zero if they are orthogonal. An ideal projector $\hat{\Pi}_I^{\vartheta,\theta}$ is therefore constructed by simply taking the outer product of a qubit of Bloch angles ϑ and θ

$$\begin{aligned} \hat{\Pi}_I^{\vartheta,\theta} &= |\psi_{\vartheta,\,\theta}\rangle\langle\psi_{\vartheta,\,\theta}| \\ &= \begin{bmatrix} \cos^2(\frac{\vartheta}{2}) & \cos(\frac{\vartheta}{2})\sin(\frac{\vartheta}{2})e^{-i\theta} \\ \sin(\frac{\vartheta}{2})\cos(\frac{\vartheta}{2})e^{i\theta} & \sin^2(\frac{\vartheta}{2}) \end{bmatrix}. \end{aligned} \tag{2.83}$$

In other words, the projection probability (2.82) is proportional to the inner product between the measured (φ, ϕ) and measuring (ϑ, θ) qubits.

The above operator represents the best possible measurement along an arbitrary qubit of Bloch coordinates (ϑ, θ). It turns out that in practice, however, we are most often only interested in knowing if the qubit to be characterized is equal to one of the four states $|0\rangle, |1\rangle, \frac{1}{\sqrt{2}}(|0\rangle + |1\rangle)$, or $\frac{1}{\sqrt{2}}(|0\rangle - |1\rangle)$ so that the whole continuum of qubits need not be resolved.

To measure the vacuum or the single-photon state, which are energy eigenstates, one needs the projectors $\hat{\Pi}_I^{0,\forall\theta}$ and $\hat{\Pi}_I^{\pi,\forall\theta}$, respectively. These projectors are best emulated by photon detectors such as avalanche photo diodes provided one assumes unit quantum efficiency.

The measurement is more complicated if one needs to measure the component of the qubit along the equatorial basis $\frac{1}{\sqrt{2}}(|0\rangle \pm |1\rangle)$ given that it is not aligned with any trivial basis such as the energy eigenbasis. One has then to resort to approximate projectors which can only discriminate between orthogonal states up to a certain accuracy.

A method to achieve this is homodyne thresholding whereby we use two operators $\hat{\Pi}_H^+$ and $\hat{\Pi}_H^-$ to project onto $\hat{\varrho}_{\frac{\pi}{2},\,0}$ and $\hat{\varrho}_{\frac{\pi}{2},\,\pi}$, respectively. In Fock

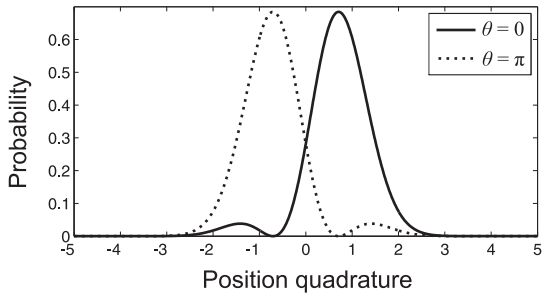

Figure 2.11: $\hat{\varrho}_{\frac{\pi}{2},0}$ and $\hat{\varrho}_{\frac{\pi}{2},\pi}$ project onto the x-quadrature basis as the solid and dotted curve, respectively. Given that the quadrature distribution of the latter is mostly biased towards negative values whereas that of the former is mostly positive, homodyne post-selection can discriminate the two—up to a certain confidence level—by grouping the outcomes of measurements into two bins whereby any measurement x is attributed to $\hat{\varrho}_{\frac{\pi}{2},0}$ if $x > 0$ and to $\hat{\varrho}_{\frac{\pi}{2},\pi}$ if $x < 0$.

basis, these projectors are given by

$$\hat{\Pi}_H^{\vartheta=\pi/2,\theta} = \begin{bmatrix} \varpi_{0,0} & \varpi_{0,1} & \cdots & \varpi_{0,\mathrm{M}} \\ \varpi_{1,0} & \varpi_{1,1} & \cdots & \vdots \\ \vdots & \vdots & \ddots & \vdots \\ \varpi_{\mathrm{M},0} & \varpi_{\mathrm{M},1} & \cdots & \varpi_{\mathrm{M},\mathrm{M}} \end{bmatrix}, \tag{2.84}$$

where $\varpi_{n,m} = \int_{\Delta(\theta)} \langle x|n\rangle\langle m|x\rangle \, \mathrm{d}x$. $M \in \mathbb{N}$ is the maximum number of photons inhabiting the measured mode and is set to $M = 1$ in the particular case of single-photon qubits we are dealing with. The range of integration is $\Delta(\theta = \pi) = (-\infty, 0]$ for $\hat{\Pi}_H^-$ and $\Delta(\theta = \pi) = [0, \infty)$ for $\hat{\Pi}_H^+$. The rationale for such matrices comes from the fact that $\hat{\varrho}_{\frac{\pi}{2},0}$ and $\hat{\varrho}_{\frac{\pi}{2},\pi}$ are most easily discriminated in the x-quadrature basis if they are associated with positive and negative quadrature points, respectively, as illustrated in Fig. 2.11.

For the sake of comparison, one can also devise the projectors that arise from the adaptive feedback method. As shown in [16, 17], the phase readout θ is obtained from a projector $\langle\theta| = \langle 0| + e^{-i\theta}\langle 1|$ with a probability density equal to $|\langle\theta|\psi_{\varphi,\phi}\rangle|^2$. Here, instead of thresholding on a quadrature readout as in the homodyne case, we instead bin the phase readout into two ranges $\Delta(\theta = 0) = [0, \frac{\pi}{2}) \cup [\frac{3\pi}{2}, 2\pi)$ and $\Delta(\theta = \pi) = [\frac{\pi}{2}, \frac{3\pi}{2})$ for projecting onto $\hat{\varrho}_{\frac{\pi}{2},0}$ and $\hat{\varrho}_{\frac{\pi}{2},\pi}$, respectively. In complete analogy to the homodyne case, we

therefore obtain the adaptive feedback projector

$$\hat{\Pi}_A^{\vartheta=\pi/2,\theta} = \begin{bmatrix} \varpi_{0,0} & \varpi_{0,1} & \cdots & \varpi_{0,\mathrm{M}} \\ \varpi_{1,0} & \varpi_{1,1} & \cdots & \vdots \\ \vdots & \vdots & \ddots & \vdots \\ \varpi_{\mathrm{M},0} & \varpi_{\mathrm{M},1} & \cdots & \varpi_{\mathrm{M},\mathrm{M}} \end{bmatrix}, \tag{2.85}$$

where $\varpi_{n,m} = \frac{1}{2\pi}\int_{\Delta(\theta)} \langle\theta|n\rangle\langle m|\theta\rangle \, \mathrm{d}\theta$. Note that the factor of $\frac{1}{2\pi}$ is introduced to enforce the completeness of the projectors.

Ambiguity in qubit discrimination

As stated above, the ideal projector is expected to discriminate perfectly between two orthogonal qubits. For example, if one were to discriminate $\varrho^{\pm} \equiv \frac{1}{\sqrt{2}}(|0\rangle \pm |1\rangle)$ with some projectors $\hat{\Pi}^{\pm}$, then ideally $\mathrm{Tr}\left\{\hat{\Pi}^{\pm}\varrho^{\pm}\right\} = 1$ and $\mathrm{Tr}\left\{\hat{\Pi}^{\mp}\varrho^{\pm}\right\} = 0$. If instead $\mathrm{Tr}\left\{\hat{\Pi}^{\pm}\varrho^{\pm}\right\} = 1-\varepsilon$ and $\mathrm{Tr}\left\{\hat{\Pi}^{\mp}\varrho^{\pm}\right\} = \varepsilon'$ with $\varepsilon, \varepsilon' \in (0,1)$, then the projectors are only approximative. This can shown to be the case for both the homodyne and adaptive feedback techniques, as illustrated by the projective probability onto any equatorial qubit in Fig. 2.12. Because we already know that the qubits $\frac{1}{\sqrt{2}}(|0\rangle \pm |1\rangle)$ are to be discriminated, non-adpative homodyne detection outperforms the adaptive feedback scheme: The two qubits can be confused for on another with a 10.1% chance for the latter method, as opposed to 18.2% for the latter. This increase in ambiguity in the adaptive feedback scheme can be attributed to the fact that the set-up "wastes" quantum information seeking the optimal local oscillator phase whereas it is already properly aligned in the non-adaptive homodyning scheme from the outset. This confirms the fact that adaptive schemes only offer an advantage over non-adaptive ones when the optimal phase is initially unknown and therefore needs to be estimated on the fly.

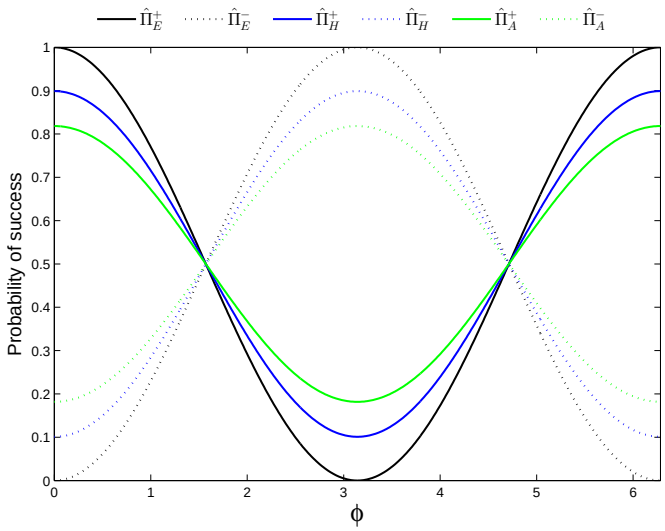

Figure 2.12: Probability of projecting the qubit $\frac{1}{\sqrt{2}}\left(|0\rangle + e^{i\phi}|1\rangle\right)$ onto $\hat{\Pi}^+$ (solid) and $\hat{\Pi}^-$ (dotted) using the exact inner product (E), homodyning (H), and adaptive feedback (A). The adaptive feedback is the worst method of all three as it can only ascertain the detection of a qubit $\frac{1}{\sqrt{2}}\left(|0\rangle \pm |1\rangle\right)$ with an 81.8% confidence level, in contrast to 89.9% for homodyne thresholding.

2.5 Linear transformations and measurements with Gaussian states and operations

In this section, we shall present the calculational tool we used for many of our simulations, particularly in Chapter 5, where the quantum states and operations involved are made up of Gaussian superpositions in the Wigner picture. I.e., any state $\hat{\rho}$ or measurement operator $\hat{\Pi}$ can be written in the Wigner picture as a function

$$W(x,p) = \sum_i G_i(x,p), \tag{2.86}$$

where G is a Gaussian function in both quadratures

$$G(x,p) = g_0 \exp\left(g_1 x^2 + g_2 x + g_3 xp + g_4 p^2 + g_5 p + g_6\right) \tag{2.87}$$

with constant coefficients $g_k \in \mathbb{C} : k \in \{0, \cdots, 6\}$ and $g_1, g_4 \in \mathbb{R}^-$. For example, a coherent state superposition,

$$|\kappa_\pm(\gamma)\rangle = \frac{1}{\sqrt{2 \pm 2e^{-2|\gamma|^2}}} \left(|\gamma\rangle \pm |-\gamma\rangle\right), \tag{2.88}$$

is made up of four such Gaussians

$$W_{|\kappa_\pm(\gamma)\rangle}(x,p) \quad = \quad \sum_{j=1}^{4} G^{(j)}_{\kappa_\pm}(x,p,\gamma), \tag{2.89}$$

where

$$G^{(1)}_{\kappa_\pm}(x,p) = -\frac{e^{-x^2-p^2+2\sqrt{2}i\gamma p}}{2\pi\left(-e^{-2\gamma^2} \mp 1\right)}, \tag{2.90a}$$

$$G^{(2)}_{\kappa_\pm}(x,p) = -\frac{e^{-x^2-p^2-2\sqrt{2}i\gamma p}}{2\pi\left(-e^{-2\gamma^2} \mp 1\right)}, \tag{2.90b}$$

$$G^{(3)}_{\kappa_\pm}(x,p) = \frac{e^{-x^2-p^2+2\sqrt{2}\gamma x-2\gamma^2}}{2\pi\left(-e^{-2\gamma^2} \mp 1\right)}, \tag{2.90c}$$

$$G^{(4)}_{\kappa_\pm}(x,p) = \frac{e^{-x^2-p^2-2\sqrt{2}\gamma x-2\gamma^2}}{2\pi\left(-e^{-2\gamma^2} \mp 1\right)}. \tag{2.90d}$$

Similarly, the projection operation by an avalanche photodiode (APD) is $\hat{\Pi}^{(\mathrm{APD})} = \hat{\mathbb{I}} - |0\rangle\langle 0|$ is made up of only two Gaussians

$$W_{\hat{\Pi}^{(\mathrm{APD})}}(x,p) = \sum_{j=1}^{2} G_{\hat{\Pi}^{(\mathrm{APD},j)}}(x,p) \tag{2.91}$$

where

$$G_{\hat{\Pi}^{(\mathrm{APD},1)}}(x,p) = \frac{1}{2\pi}, \tag{2.92a}$$

$$G_{\hat{\Pi}^{(\mathrm{APD},2)}}(x,p) = -\frac{1}{\pi} e^{-x^2-p^2}. \tag{2.92b}$$

If we now assume that all transformations underwent by the state $\hat{\rho}$ prior to measurement are linear, then the generic Gaussian form (2.87) is conserved and only the quadrature vector

$$\vec{q} = (x_1, p_1, \cdots, x_N, p_N)^T \tag{2.93}$$

of the N modes involved is transformed by a linear mapping

$$\vec{q} \to \mathbf{A} \cdot \vec{q}, \tag{2.94}$$

where the $2N \times 2N$ matrix $\mathbf{A}$ is determined by the linear assemblage of passive elements making up the circuit, e.g., beam splitters, phase shifters, squeezers, etc.

Consider the generic quantum circuit depicted in Fig. 2.13 where once again we only have Gaussian states and operators as defined by (2.86-2.87). The effect of a re-scaled quadrature space (2.94) on a given Wigner function is equivalent to leaving the space unchanged while submitting the function to the inverse transformation. We shall label the transformed multimode Wigner function by a tilde such that the mapping (2.94) yields

$$W(\vec{q}) \to W(\mathbf{A}^{-1}\vec{q}) = \tilde{W}(\vec{q}). \tag{2.95}$$

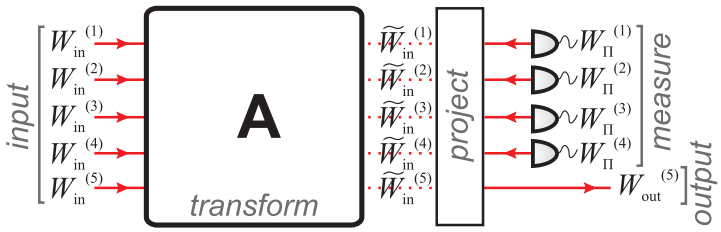

Figure 2.13: Sketch of a black box quantum circuit made up of $N = 5$ input modes, $M = 4$ measurement modes, and $N - M = 1$ output modes. Each state occupying mode k is represented by a Wigner function $W^{(k)}$. The input $\prod_n^N W_{\text{in}}^{(n)}$ is mapped according to (2.95) into a linearly transformed state $\prod_n^N \tilde{W}_{\text{in}}^{(n)}$ which is then projected onto a "measurement state" $\prod_m^M W_{\hat{\Pi}}^{(m)}$.

If we now apply the measurement operators over $M < N$ modes, the output over the remaining $N-M$ modes is given by

$$W_{\hat{\rho}_{\text{out}}} = \iint_{\mathbb{R}} \prod_n^N \tilde{W}_{\hat{\rho}_{\text{in}}}^{(n)} \cdot \prod_m^M W_{\hat{\Pi}}^{(m)} \, \mathrm{d}x_m \mathrm{d}p_m \tag{2.96}$$

where the superscript denotes the k^{th} mode.

Note that the number of output modes equals the number of input modes N minus the number of measured modes M. If $M = N$, then there is no output state and the inner product (2.96) leaves us with a scalar representing

the success probability—or norm—of the projection of input states onto the measurement operators. Alternatively, this number could be interpreted as the fidelity between the overall states at either side of the diagram in Fig. 2.13.

The rationale for (2.96) is valid regardless of whether the Wigner functions are Gaussian superpositions: From a mathematical standpoint, projective measurements are inner products between the measured state and the measuring operator. In functional analysis, this translates to an integral of the product of two states—the measured and the measuring state—over the entire phase space of measurement. The simplicity that comes from using (2.96) with Gaussian superpositions is due to the fact that products and integrals of Gaussians are also still Gaussian.

2.6 Figures of merit

Three figures of merit are of ubiquitous use in quantum information: fidelity, success probability, and purity. Although each one of them tells of a different aspect of quantum states, they all originate from same the mathematical blueprint of overlap between quantum objects—cf. equation (2.72) and Table 2.3.

- **Fidelity** is the measure of similarity between two quantum states W_A and W_B. If at least one of them is pure,[15] it is written

$$F(A,B) = 2\pi \iint_{\mathbb{R}} W_A(x,p) W_B(x,p)\,\mathrm{d}x\,\mathrm{d}p. \tag{2.98}$$

- **Purity** can be thought of as the fidelity of a state with itself

$$P(A) = F(A,A) = 2\pi \iint_{\mathbb{R}} W_A(x,p) W_A(x,p)\,\mathrm{d}x\,\mathrm{d}p. \tag{2.99}$$

  In other words, given several copies of the state, how consistent, or coherent, are all the instances with one another? Alternatively, how much coherence do they contain and how well can they display quantum interference? Recall the sketch in Fig. 2.1; the illustrated mixed

[15] The general expression is given for the fidelity between two (possibly mixed) states $\hat{\rho}_1$ and $\hat{\rho}_2$ is [18]

$$F(\hat{\rho}_1,\hat{\rho}_2) = \mathrm{Tr}\left\{\sqrt{\hat{\rho}_1^{1/2}\,\hat{\rho}_2\,\hat{\rho}_1^{1/2}}\right\}. \tag{2.97}$$

state instantiates into orthogonal states with equal probability and hence has no coherence whatsoever. It is completely mixed and it's purity is zero.

- **Success probability** is the probability with which a given state W_A can be produced from an input state W measurement operations $\hat{\Pi}$. (This was expanded on in §2.5.) More generally, the success probability of any state W_A, regardless of the process through which it was obtain, is given by the its norm, i.e., it's overlap with the unit operator[16]

$$S(A) = F(\hat{\mathbb{I}}, A) = \frac{1}{2\pi} \iint_{\mathbb{R}} W_A(x, p)\, \mathrm{d}x\, \mathrm{d}p. \tag{2.100}$$

[16]The $1/2\pi$ factor emerges from the Weyl transform of the unit operator $\hat{\mathbb{I}}$.

Chapter 3

Deterministic Bell measurements: The hard way

We outline a proof that teleportation with a single particle is in principle just as reliable as with two particles. We thereby hope to dispel the skepticism surrounding single-photon entanglement as a valid resource in quantum information. A deterministic Bell state analyzer is proposed which uses only classical resources, namely coherent states, a Kerr non-linearity, and a two-level atom.

3.1 Introduction

Ever since Tan, Walls and Collett [19] articulated the notion of single-particle nonlocality [20, 21], controversy has surrounded the ability of a single particle to exhibit entanglement [22, 23, 24, 25, 26]. Proposals [27, 28, 29, 30, 31, 32, 33, 34, 35, 36, 37, 38] and experiments [39, 40, 41] demonstrating single photon entanglement, nonlocality, and entanglement purification have been performed, but still, the prospect of teleportation using single photon entanglement as the quantum resource has not been regarded on equal footing with teleportation schemes involving "carrier" particles in each of the entangled modes.

Most of the confusion over this issue can be blamed on semantics: By "single-particle" entanglement, what is really meant is the quantum correlation of two or more modes over which a single excitation (i.e., the particle) is distributed. Regardless of the degree of freedom under consideration, one

should therefore think of entanglement as occurring between modes rather than between any particular excitations of those modes [42]. In fact, all that is needed to enable entanglement is a system with an associated Hilbert space whose dimension can be factored [43]. In light of the above, any reference to single-photon nonlocality in the present chapter should be pictured with field mode entanglement in mind.

Although single-photon teleportation has been discussed quite extensively, and demonstrated experimentally [44], its success rate has been limited to at most 50%. This could be taken by the detractors of entanglement with a single particle as an indication that the involvement of the vacuum state as an agent of correlations bears with it a fundamental limitation. We argue that this lack of determinism, however, is not due to an intrinsic shortcoming of single-particle teleportation, but rather to the difficulty of implementing a deterministic analyzer for the following Bell states:

$$|\psi^{\pm}\rangle = \frac{1}{\sqrt{2}}\left(|01\rangle \pm |10\rangle\right) \tag{3.1}$$

$$|\varphi^{\pm}\rangle = \frac{1}{\sqrt{2}}\left(|00\rangle \pm |11\rangle\right) \tag{3.2}$$

where, e.g., $|01\rangle \equiv |0\rangle_{\mathrm{A}} \otimes |1\rangle_{\mathrm{B}}$ is the shorthand notation for vacuum in Alice's mode and a single photon in Bob's.

If one is restricted to linear optics, it has been shown that this difficulty is fundamental [1], and that the success rate appeared to be limited to the above mentioned 50% . Recently, Pavičić demonstrated that this thereshold can be raised asymptotically to 100% if one uses conditional dynamics on the polarization degree of freedom of a two-photon Bell state [45]. However, his scheme does not lend itself to single photon Bell states because the delocalization behavior of polarization at beam splitters is different for the vacuum state than for a single photon state. E.g., the splitting of, say, a vertically polarized photon $|V\rangle$ on a beam splitter leads to a nonlocal superposition $\frac{1}{\sqrt{2}}\left(|V,0\rangle + |0,V\rangle\right)$ whereas the vacuum remains separable $|0\rangle \otimes |0\rangle$, suggesting once again the alleged shortcoming of the vacuum.

However, what we wish to demonstrate in this paper is that fundamentally, Nature makes no difference as to whether the entanglement needed to perform teleportation is carried by one, or more than one, particle. Hence, we will allow any classical resource, linear or non-linear, but no additional quantum resources. The reader should be warned that although the scheme we outline below is certainly experimentally implementable, it will not be the most practical scheme to teleport a state. Our aim is simply to argue that, at the fundamental level, any task that can be done by a multi-particle

entangled state can also be achieved by the isomorphic state with the vacuum state and single-particle state as the basis. Specifically, we show that deterministic teleportation can be achieved with such a state as the only quantum resource.

In this chapter, we aim to assert the soundness of single-particle teleportation by outlining an experiment which, in principle, can identify any of the four Bell states deterministically and with arbitrary accuracy. The main challenge to this end is that the Bell states $|\varphi^{\pm}\rangle$ are not energy (or more generally, particle number) eigenstates. In particular, no linear-optical scheme can deterministically resolve their phases [50]. We propose a way around this by storing the photonic qubits in two-level atoms. Owing to the two-dimensional Hilbert space of a two-level system, its stored qubits can conveniently be rotated on the Bloch sphere via coherent excitations. Once aligned with the energy eigenbasis of the atom, the orientation of the initial qubit can easily be deduced due to the unitarity of the rotation. Before treating the two-mode case of $|\varphi^{\pm}\rangle$, we first consider in Sec. 3.2 the Hadamard rotation of the single-mode qubit $\frac{1}{\sqrt{2}}(|0\rangle \pm 1) \rightarrow \{|0\rangle, |1\rangle\}$. We then follow up in Sec. 3.3 with a description of the actual teleportation setup and its two-stage Bell analyzer.

3.2 Hadamard rotation of a vacuum-photon superposition

Consider a qubit made up of an equal superposition of the vacuum and a single photon:

$$|X_\theta\rangle = \frac{1}{\sqrt{2}}\Big(|0\rangle + e^{i\theta}|1\rangle\Big) \tag{3.3}$$

where θ is the equatorial angle on the Bloch sphere. Our first goal is to devise a projector $\hat{\Pi}_\theta = |X_\theta\rangle\langle X_\theta|$ which can resolve the phase θ. Note that any projector $\hat{\Pi}_\theta$ can be implemented from any other $\hat{\Pi}_\beta$ by interposing a phase shift $\Delta\theta = \theta - \beta$. We will show in 3.3.1 that such a projector, when applied in parallel to the two modes of $|\varphi^{\pm}\rangle$, will allow us to resolve the sign of the superposition. We shall for now restrict ourselves to the single-mode case and describe how $|X_0\rangle$ can be distinguished from $|X_\pi\rangle$.

Let's define two initially separated Hilbert spaces pertaining to an atomic and a photonic mode, respectively. Formally, the space under consideration is $\mathcal{H} = \mathcal{H}_{\text{atom}} \otimes \mathcal{H}_{\text{photon}}$ where $\mathcal{H}_{\text{photon}} = \{|n\rangle : n \in \mathbb{N}\}$ and $\mathcal{H}_{\text{atom}} = \{|g\rangle, |e\rangle\}$. Here, n denotes the number of photons, and $|g\rangle$ and $|e\rangle$ denote the ground and excited atomic states, respectively. The interaction between

the two modes is dictated by the Jaynes-Cummings (JC) Hamiltonian, expressed below in the rotating wave approximation:

$$\hat{H} = \hbar\gamma \left(\hat{s}^{-}\hat{a}^{\dagger} + \hat{s}^{+}\hat{a}\right) \tag{3.4}$$

where $\hat{a}$ ($\hat{a}^{\dagger}$) is the photon annihilation (creation) operator, and $\hat{s}^{+}$ ($\hat{s}^{-}$) is the atomic raising (lowering) operator. γ quantifies the strength of the photon-atom coupling. The transformations undergone by any preparation in $\mathcal{H}$ under the action of $\hat{H}$ are summarized in §3.2.1 and shall be used in what follows.

The candidate qubits $|X_0\rangle$ and $|X_\pi\rangle$ to be measured are initially stored in the photonic mode whereas the atom is prepared in the ground state. Upon an interaction time $\tau = \frac{\pi}{2\gamma}$, we obtain the transformation

$$\frac{1}{\sqrt{2}}|g\rangle \otimes (|0\rangle \pm |1\rangle) \xrightarrow{\tau} \frac{1}{\sqrt{2}} (|g\rangle \mp i|e\rangle) \otimes |0\rangle \tag{3.5}$$

whereby the photonic qubit has been transferred to the atomic mode and the state is are once again separable. The atomic qubit at this stage is not yet measurable in the energy eigenbasis. It can, however, be rotated so as to align itself with the eigenstates of the atom by shining a strong coherent beam $|\alpha\rangle$ with $|\alpha| \gg 1$. (This coherent state will incidentally serve as a reference phase.) If one chooses an interaction time $t_{\mathrm{s}} = \frac{\pi}{4\gamma|\alpha|}$ the states transforms to a very good approximation (see below) as

$$\begin{cases} \frac{1}{\sqrt{2}} (|g\rangle + i|e\rangle) \otimes |\alpha\rangle \xrightarrow{t_{\mathrm{s}}} |g\rangle \otimes |\alpha\rangle \\ \frac{1}{\sqrt{2}} (|g\rangle - i|e\rangle) \otimes |\alpha\rangle \xrightarrow{t_{\mathrm{s}}} |e\rangle \otimes |\alpha\rangle \end{cases} . \tag{3.6}$$

If one now determines via, say, a fluorescence measurement that the final state of the atom was the ground (excited) state then one can conclude that the initial qubit was $|X_\pi\rangle$ ($|X_0\rangle$). A sketch of the physics underlying the transformations (3.5) and (3.6) is shown in Fig. 3.1.

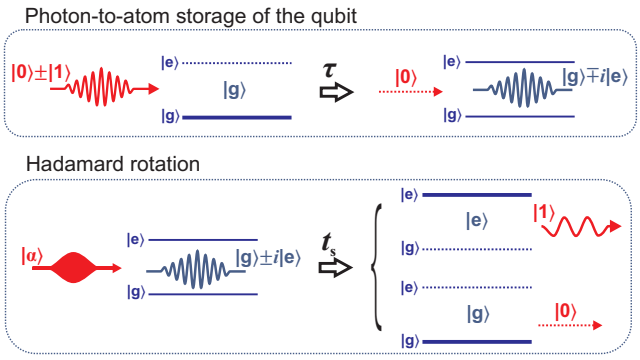

Figure 3.1: Sketch of the two-stage implementation of the $\hat{\Pi}_\theta$ projector for $\theta \in \{0, \pi\}$. The photonic and atomic modes are colored in red and blue, respectively. First, the photonic qubit is transfered to an atom initially in the ground state (top). Second, a coherent $\frac{\pi}{2}$-pulse is applied on the atom so as to rotate the qubit into one of the energy basis vectors $|g\rangle$ or $|e\rangle$ (bottom). The subsequent de-excitation of the atom (or lack thereof) will reveal that the initial photonic qubit was $|X_0\rangle$ (or $|X_\pi\rangle$).

As derived in §3.2.1, however, an error in the correspondence between initial and final states in (3.6) will arise for weaker coherent fields. This is where the superselection rule kicks in, because it is clear that the left- and the right hand side of (3.6) do not contain the same number of particles on average. An exact analysis of the transformation, made in §3.2.1, shows that the probability for such an error decreases with the strength $|\alpha|$ of the coherent state. For example, the probability of erroneously identifying $|X_0\rangle$ instead of $|X_\pi\rangle$ is given by

$$P_{\text{err}} = \frac{e^{-|\alpha|^2}}{2} \sum_{n=0}^{\infty} \frac{|\alpha|^{2n}}{n!} \left| \cos\left(\frac{\pi\sqrt{n}}{4|\alpha|}\right) - \frac{\sqrt{n}}{|\alpha|} \sin\left(\frac{\pi\sqrt{n}}{4|\alpha|}\right) \right|^2 . \tag{3.7}$$

The fidelity of the Hadamard rotation is therefore contingent on the strength of the coherent $\frac{\pi}{2}$-pulses. The error probability is plotted in Fig. 3.2, and it can be seen that already for $|\alpha|^2 = 50$, the error probability is at the 1% level. This means that already for rather modest coherent state excitations, the unitarity of the Hadamard operation in (3.6) is effectively achieved.

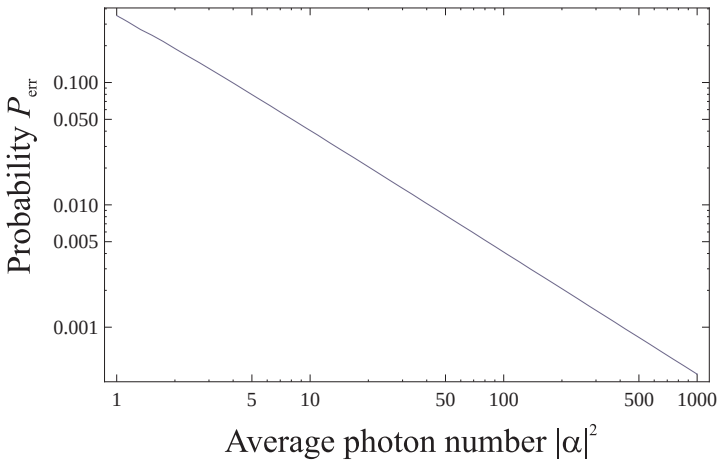

Figure 3.2: The probability $P_{\rm err}$ of an erroneous projection as a function of the coherent state average photon number.

3.2.1 Jaynes-Cummings model

We shall summarize here the mathematics behind the Hadamard rotation treated in Sec. 3.2. This is based on an application of the Jaynes-Cummings model whose Hamiltonian has already been presented in (3.4). The Schrödinger equation corresponding to this system is solved by

$$\begin{aligned} |\psi(t)\rangle &= \sum_{n=0}^{\infty} \Big[\left(c_e c_n \cos(\gamma t\sqrt{n+1}) - i c_g c_{n+1} \sin(\gamma t\sqrt{n+1})\right) |e\rangle \\ &\quad + \left(c_g c_n \cos(\gamma t\sqrt{n}) - i c_e c_{n-1} \sin(\gamma t\sqrt{n})\right) |g\rangle \Big] |n\rangle \end{aligned} \tag{3.8}$$

where the initial state is given by

$$|\psi(0)\rangle = |\psi_{\rm atom}(0)\rangle \otimes |\psi_{\rm photon}(0)\rangle = (c_g|g\rangle + c_e|e\rangle) \otimes \sum_{n=0}^{\infty} c_n |n\rangle, \tag{3.9}$$

and c_g, c_e, and c_n are complex. An in-depth derviation of (3.8) is given in [124].

Three key transformations of the atom-photon eigenstates are of interest to us, namely

$$|g,0\rangle \rightarrow |g,0\rangle, \tag{3.10}$$

$$|g,n\rangle \rightarrow \cos(\gamma t\sqrt{n})|g,n\rangle - i\sin(\gamma t\sqrt{n})|e,n-1\rangle, \tag{3.11}$$

$$|e,n\rangle \rightarrow \cos(\gamma t\sqrt{n+1})|e,n\rangle - i\sin(\gamma t\sqrt{n+1})|g,n+1\rangle. \tag{3.12}$$

The transfer of the qubit from the photon to the atomic modes is thus given by

$$\begin{aligned}
& |g\rangle \otimes \frac{1}{\sqrt{2}}\left(|0\rangle \pm |1\rangle\right) = \frac{1}{\sqrt{2}}\left(|g0\rangle \pm |g1\rangle\right) \\
\rightarrow \quad & \frac{1}{\sqrt{2}}\left(|g0\rangle \mp i\sin(\gamma t)|e0\rangle \pm \cos(\gamma t)|g1\rangle\right) \\
= \quad & \left\{t = \tau = \frac{\pi}{2\gamma}\right\} \\
= \quad & \frac{1}{\sqrt{2}}\left(|g\rangle \mp i|e\rangle\right) \otimes |0\rangle
\end{aligned} \tag{3.13}$$

Now that the qubit is stored in the atomic mode, let's derive how a coherent excitation $|\alpha\rangle$ performs the Hadamard rotation.

$$\begin{aligned}
& \frac{1}{\sqrt{2}}\left(|g\rangle \pm i|e\rangle\right) \otimes |\alpha\rangle = \frac{1}{\sqrt{2}}\left(|g\rangle \pm i|e\rangle\right) \otimes e^{-\frac{|\alpha|^2}{2}} \sum_{n=0}^{\infty} \frac{\alpha^n}{\sqrt{n!}}|n\rangle \\
= \quad & \frac{e^{-\frac{|\alpha|^2}{2}}}{\sqrt{2}} \sum_{n=0}^{\infty} \frac{\alpha^n}{\sqrt{n!}}\left(|gn\rangle \pm i|en\rangle\right) \\
\rightarrow \quad & \frac{e^{-\frac{|\alpha|^2}{2}}}{\sqrt{2}} \sum_{n=0}^{\infty} \frac{\alpha^n}{\sqrt{n!}}\Big[\cos(\gamma t\sqrt{n})|gn\rangle - i\sin(\gamma t\sqrt{n})|e, n-1\rangle \\
& \pm i\cos(\gamma t\sqrt{n+1})|en\rangle \pm \sin(\gamma t\sqrt{n+1})|g, n+1\rangle\Big] \\
= \quad & \frac{e^{-\frac{|\alpha|^2}{2}}}{\sqrt{2}} \sum_{n=0}^{\infty} \frac{\alpha^n}{\sqrt{n!}}\Big[\left(\cos(\gamma t\sqrt{n}) \pm \frac{\sqrt{n}}{\alpha}\sin(\gamma t\sqrt{n})\right)|gn\rangle \\
& + i\left(\pm\cos(\gamma t\sqrt{n+1}) - \frac{\alpha}{\sqrt{n+1}}\sin(\gamma t\sqrt{n+1})\right)|en\rangle\Big] \\
= \quad & \left\{t = t_{\mathrm{s}} = \frac{\pi}{4\gamma\,|\alpha|}\right\} \\
= \quad & \frac{e^{-\frac{|\alpha|^2}{2}}}{\sqrt{2}} \sum_{n=0}^{\infty} \frac{\alpha^n}{\sqrt{n!}}\Big[\left(\cos\left(\frac{\pi\sqrt{n}}{4\,|\alpha|}\right) \pm \frac{\sqrt{n}}{\alpha}\sin\left(\frac{\pi\sqrt{n}}{4\,|\alpha|}\right)\right)|gn\rangle \\
& + i\left(\pm\cos\left(\frac{\pi\sqrt{n+1}}{4\,|\alpha|}\right) - \frac{\alpha}{\sqrt{n+1}}\sin\left(\frac{\pi\sqrt{n+1}}{4\,|\alpha|}\right)\right)|en\rangle\Big]
\end{aligned} \tag{3.14}$$

If we now assume that $\alpha \approx n^{1/2}$, the cosine and sine function become approximately equal, thereby finalizing the Hadamard transformations (3.6).

One needs however to keep track of the error arising from the approximation. For example, the probability of erroneously obtaining a final state $|gn\rangle$ instead of $|en\rangle$ will be given by any non-zero remnant in the factor of $|gn\rangle$:

$$P_{\rm err} = \frac{e^{-|\alpha|^2}}{2} \sum_{n=0}^{\infty} \frac{|\alpha|^{2n}}{n!} \left| \cos\left(\frac{\pi\sqrt{n}}{4|\alpha|}\right) - \frac{\sqrt{n}}{|\alpha|} \sin\left(\frac{\pi\sqrt{n}}{4|\alpha|}\right) \right|^2 . \tag{3.15}$$

3.3 The Bell-state analyzer

The teleportation protocol is sketched in Fig. 3.3. It consists of an entangled resource $|\psi^+\rangle = \frac{1}{\sqrt{2}}(|01\rangle + |10\rangle)$ linking Alice and Bob and an unknown state $|\xi\rangle = a|0\rangle + b|1\rangle$ (where $|a|^2 + |b|^2 = 1$) to be teleported from Alice to Bob. The overall tripartite state, with the first two modes belonging to Alice and the last to Bob, reads

$$\begin{aligned} |\Psi\rangle &= |\xi\rangle \otimes |\psi^+\rangle \\ &= \frac{1}{\sqrt{2}}\left(a|001\rangle + a|010\rangle + b|101\rangle + b|110\rangle\right) \\ &= \frac{1}{2}|\varphi^+\rangle \otimes (a|1\rangle + b|0\rangle) + \frac{1}{2}|\varphi^-\rangle \otimes (a|1\rangle - b|0\rangle) + \\ &\quad \frac{1}{2}|\psi^+\rangle \otimes (a|0\rangle + b|1\rangle) + \frac{1}{2}|\psi^-\rangle \otimes (a|0\rangle - b|1\rangle)\,. \end{aligned}$$

Upon the detection of $|\psi^\pm\rangle$ or $|\varphi^\pm\rangle$, Alice can inform Bob via a classical channel that he has in his possession $a|0\rangle \pm b|1\rangle$ or $a|1\rangle \pm b|0\rangle$, respectively. Bob can then perform a local unitary operation of his qubit to recover $|\xi\rangle$ (Table 3.1).

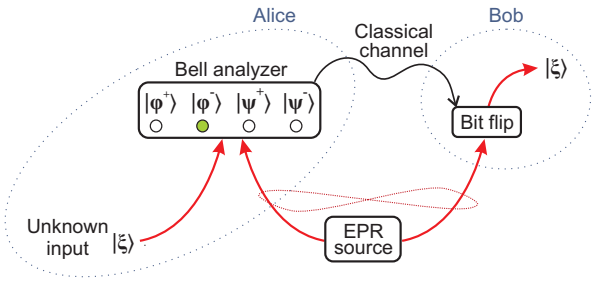

Figure 3.3: Teleportation protocol. (Here, the instance where Alice detects $|\phi^-\rangle$ is highlighted.)

Let's now focus on the Bell analyzer. We propose that it consist of two steps: Alice first distinguishes $|\psi^\pm\rangle$ from $|\varphi^\pm\rangle$, and then she determines the

Bell state	Local operation
$\|\varphi^+\rangle$	$a\|1\rangle + b\|0\rangle \rightarrow$ transfer, flip $\rightarrow \|\xi\rangle$
$\|\varphi^-\rangle$	$a\|1\rangle - b\|0\rangle \rightarrow$ shift, transfer, flip $\rightarrow \|\xi\rangle$
$\|\psi^+\rangle$	$a\|0\rangle + b\|1\rangle = \|\xi\rangle$
$\|\psi^-\rangle$	$a\|0\rangle - b\|1\rangle \rightarrow$ shift $\rightarrow \|\xi\rangle$

Table 3.1: Table of the local operations to be performed by Bob based on the four possible Bell states measured by Alice. In the case where Alice measures $|\psi^+\rangle$, no action need to be taken by Bob. In the other three cases, he will have to apply a photonic π phase shift (abridged 'shift' below) and/or transfer the photonic qubit to a two-level atom and then apply a coherent π pulse (abridged 'transfer, flip').

signs of each superposition with separate setups. We discuss each step in the two subsections below. A sketch of the Bell analyzer is shown in Fig. 3.4.

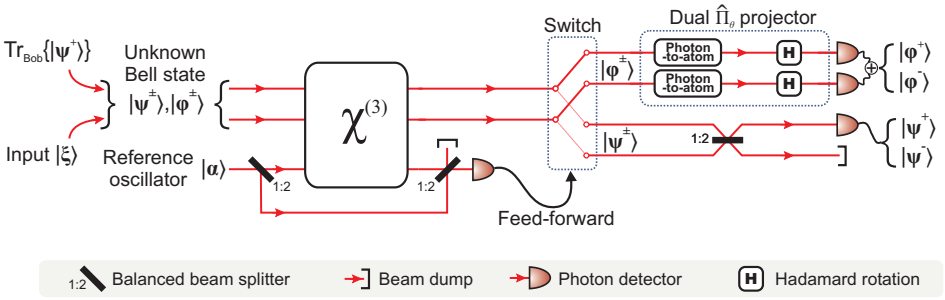

Figure 3.4: Conceptual sketch of the Bell analyzer. The first part consists of a quantum non-demolition measurement which separates $|\psi^\pm\rangle$ from $|\varphi^\pm\rangle$ by inducing a phase shift in an auxiliary coherent field if $|\psi^\pm\rangle$ was input. Depending on the outcome of this first measurement, a double pole, double throw (DPDT) switch forwards the state to either a balanced beam splitter (for $|\psi^\pm\rangle$), or a "dual-rail" extension of the projector discussed in Sec. 3.2 (for $|\varphi^\pm\rangle$).

3.3.1 Discrimination between $|\psi^\pm\rangle$ and $|\varphi^\pm\rangle$

The main difference between $|\psi^\pm\rangle$ and $|\varphi^\pm\rangle$ is that the former are energy eigenstates which are easily separable by a rotation in the energy basis (e.g., with a 50/50 beam splitter). The latter, however, are not energy or particle

eigenstates and thus require a more elaborate treatment to reveal the sign of their superposition by an energy (particle) counting detector. Our first task is therefore to branch off $|\psi^{\pm}\rangle$ and $|\varphi^{\pm}\rangle$ so that each be forwarded to the appropriate analyzer. We propose to achieve this sorting with a dual-rail quantum non-demolition (QND) measurement, first proposed for quantum error correction [51]. The idea behind this QND is to induce a phase shift in an auxiliary coherent beam depending on whether the total number of photons in the Bell state is odd (as in $|\psi^{\pm}\rangle$) or even (as in $|\varphi^{\pm}\rangle$). The coherent probe remains separable all along so that no collapse is incurred on the individual Bell states. The interaction Hamiltonian, which could be implemented physically as a cross-Kerr effect [52], is written in the rotating wave approximation as

$$\hat{H}_{\text{int}} = \hbar\kappa \left(\hat{a}^{\dagger}\hat{a} + \hat{b}^{\dagger}\hat{b}\right) \hat{c}^{\dagger}\hat{c} \tag{3.16}$$

where κ is the strength of the interaction.

If we set the interaction time to $\tau_{\text{M}} = \frac{\pi}{\kappa}$, the propagator becomes $e^{-i\pi\left(\hat{a}^{\dagger}\hat{a}+\hat{b}^{\dagger}\hat{b}\right)\hat{c}^{\dagger}\hat{c}}$ and we are then faced with two possible scenarios. If the Bell state is $|\psi^{\pm}\rangle$, then the overall state $|\psi^{\pm}\rangle \otimes |\alpha\rangle$ transforms as follows:

$$\begin{aligned}
|\psi^{\pm}\rangle \otimes |\alpha\rangle \quad &= \quad \frac{e^{\frac{|\alpha|^2}{2}}}{\sqrt{2}} \left(|01\rangle \pm |10\rangle\right) \otimes \sum_{n=0}^{\infty} \frac{\alpha^n}{\sqrt{n!}} |n\rangle \\
&\xrightarrow{\tau_{\text{M}}} \quad \frac{e^{\frac{|\alpha|^2}{2}}}{\sqrt{2}} \left(|01\rangle \pm |10\rangle\right) \otimes \sum_{n=0}^{\infty} e^{-i\pi n} \frac{\alpha^n}{\sqrt{n!}} |n\rangle \\
&= \quad \frac{1}{\sqrt{2}} \left(|01\rangle \pm |10\rangle\right) \otimes |-\alpha\rangle \\
&= \quad |\psi^{\pm}\rangle \otimes |-\alpha\rangle.
\end{aligned} \tag{3.17}$$

On the other hand, if we start with $|\varphi^{\pm}\rangle$, a similar derivation leaves the state unchanged:

$$|\varphi^{\pm}\rangle \otimes |\alpha\rangle \xrightarrow{\tau_{\text{M}}} |\varphi^{\pm}\rangle \otimes |\alpha\rangle. \tag{3.18}$$

It can now be seen that the differentiation of $|\psi^{\pm}\rangle$ and $|\varphi^{\pm}\rangle$ can be achieved be comparing the phases of the auxiliary coherent fields: Only those coherent fields that have interacted with $|\psi^{\pm}\rangle$ acquire a π phase shift, those that interacted with $|\varphi^{\pm}\rangle$ remain unchanged. The acquisition of the π phase shift can be observed by a simple classical interference between the probe beam and a reference coherent state on a balanced beam splitter.

3.3.2 Discrimination between $|\varphi^+\rangle$ and $|\varphi^-\rangle$

Now that $|\psi^\pm\rangle$ and $|\varphi^\pm\rangle$ are branched off, there remain to determine the signs at the superscript in either case. As already mentioned, the differentiation between the triplet (ψ^+) and singlet states (ψ^-) can be done easily by joining the two constituent modes on a balanced beam splitter. The outgoing modes become disentangled and the detection of the photon at either output ports has a direct correspondence to the sign of the superposition.

A more complicated situation occurs when the QND announces the states $|\varphi^\pm\rangle$. The discrimination between the signs requires a two-mode extension to the single-mode projector described in Sec. 3.2. This is done by placing a ground-state atom in the path of each of the incoming photonic qubits. After an interaction time of $\tau = \frac{\pi}{2\gamma}$, the evolution of the photon-atom system will be the straightforward extension of (3.5), namely

$$\begin{aligned} |gg\rangle \otimes |\varphi^\pm\rangle \quad &= \quad \frac{1}{\sqrt{2}}|gg\rangle \otimes (|00\rangle \pm |11\rangle) \\ &\xrightarrow{\tau} \quad \frac{1}{\sqrt{2}}\left(|gg\rangle \mp |ee\rangle\right) \otimes |00\rangle. \end{aligned} \tag{3.19}$$

Now that the qubits have been completely transferred from the photonic to the atomic modes, we can call upon the Hadamard transformation worked out in (3.6). This rotation gives:

$$\begin{cases} \frac{1}{\sqrt{2}}\left(|gg\rangle - |ee\rangle\right) \otimes |\alpha\alpha\rangle \xrightarrow{t_\mathrm{s}} \frac{1}{\sqrt{2}}\left(|gg\rangle + |ee\rangle\right) \otimes |\alpha\alpha\rangle \\ \frac{1}{\sqrt{2}}\left(|gg\rangle + |ee\rangle\right) \otimes |\alpha\alpha\rangle \xrightarrow{t_\mathrm{s}} \frac{1}{\sqrt{2}}\left(|ge\rangle + |eg\rangle\right) \otimes |\alpha\alpha\rangle \end{cases} \tag{3.20}$$

where once again $t_\mathrm{s} = \frac{\pi}{4\gamma|\alpha|}$ is the time it takes to apply a $\frac{\pi}{2}$-coherent pulse.

The difference between the two final states lies in the parity of the energy quanta stored in the atoms. An initial photonic state $|\varphi^-\rangle$ corresponds to a total energy of exactly one quantum: $\frac{1}{\sqrt{2}}\left(|ge\rangle + |eg\rangle\right)$. Conversely, $|\varphi^+\rangle$ leads to either zero or two quanta: $\frac{1}{\sqrt{2}}\left(|gg\rangle + |ee\rangle\right)$. The efficiency of this Hadamard rotation, as argued in Sec. 3.2, increases with the mean photon number of the $\frac{\pi}{2}$ pulses and can thus be made asymptotically ideal for strong coherent fields.

3.4 Deterministic quantum computing

We finally show that using the experimental techniques presented in this paper, it is also possible to achieve deterministic quantum computing based

on single photon entanglement. It has been shown by Lund and Ralph [53] that nondeterministic quantum computing using the superposition of vacuum and a single photon as a qubit can be obtained with linear optics and photon counters. However, by allowing for non-linear operations, it is possible to bring this idea into a deterministic setting.

A universal set of quantum gates could consist of the phase rotation gate, the Hadamard gate and the control sign shift (CS) gate. The phase rotation gate is easily implementable using a simple phase delay. A deterministic Hadamard gate can be constructed using the JC interaction as outlined in Sec. 3.2. The CS gate can be implemented by storing the input modes $(a|0\rangle + b|1\rangle) \otimes (c|0\rangle + d|1\rangle)$ in a pair of atoms (via the JC interaction), applying a π pulse and letting it decay:

$$\begin{aligned} & (ac|00\rangle + ad|01\rangle + bc|10\rangle + bd|11\rangle) \otimes |gg\rangle \\ \xrightarrow{\tau} \quad & (ac|gg\rangle + ad|ge\rangle + bc|eg\rangle + bd|ee\rangle) \otimes |00\rangle \\ \xrightarrow{2t_S} \quad & (ac|gg\rangle + ad|ge\rangle + bc|eg\rangle - bd|ee\rangle) \otimes |00\rangle \\ \xrightarrow{\text{decay}} \quad & (ac|00\rangle + ad|01\rangle + bc|10\rangle - bd|11\rangle) \otimes |gg\rangle \end{aligned}$$

Combining this CS gate with the above mentioned phase and Hadamard gate, universal quantum computation based on qubits of the form (3.3) can in principle be executed.

3.5 Conclusion

Our proposal is difficult to implement experimentally in that it requires expertise in two separate and highly specialized areas, namely the generation of single photons and the manipulation of light-matter interactions. We believe however that our theoretical sketch will help bring some closure to the debate that still surrounds the notion of single-particle nonlocality. The root of this debate can be traced to the perception of the vacuum $|0\rangle$ as a singular—if not pathological [24]—state whose similarity to the other Fock states has little physical meaning beyond mathematical isomorphism. By building on earlier discussions about mode entanglement and the nonlocality of this state [20, 27, 47, 49], and by showing the full power of single-photon teleportation with no additional quantum resources, we hope to have proved the contrary.

Chapter 4

Hybrid Bell tests

4.1 Background and motivation

The emergence of quantum mechanics, with entanglement as its most notable manifestation, has brought about two conflicting views of physical reality. The first and most intuitive is the local realistic view. It maintains that physical observables are deterministic and therefore independent of measurement. This view, endorsed by Einstein, Podolsky, and Rosen (EPR) [54] has come to be known as the local hidden variables (LHV) model whereby predetermined variables, though possibly inaccessible to us, account for the measured statistics of any correlated system. The competing view is known as the Copenhagen interpretation. It is an orthodox reading of quantum mechanics that considers any observable to be intrinsically uncertain unless resolved by measurement. One of the consequences of the Copenhagen interpretation—quantum nonlocality—exhibits an apparent noncompliance with relativity which led EPR to dismiss quantum mechanics as incomplete. The debate between the LHV model and the Copenhagen interpretation was confined to the philosophical realm until John Bell proposed an experimental framework for its resolution: By measuring entangled parties in different bases, a linear combination of expectation values can be assembled into an inequality which must be satisfied by any LHV theory. A violation of the inequality is otherwise a vindication of quantum nonlocality [55, 56]. Despite experimental evidence in favor of quantum mechanics, the LHV model has yet to be unequivocally ruled out. In order to do so, the measurements on the entangled parties need to take place in non-overlapping light cones. This ensures that the so-called communication loophole is closed so that no classical signaling could account for the observed correlations. A second

challenge, the detection loophole, stems from inefficient measurements and was identified as early as 1970 to be the prime obstacle to conclusive Bell tests [57]. Inefficient detection weakens correlations and makes it harder to distinguish the statistical predictions of quantum mechanics from those of LHV theories. So far, each loophole has been closed separately: The detection loophole has been closed in ionic systems [58] whereas the communication loopole has been closed in all-optical setups [59, 60]. All-optical schemes are most often concerned with tackling the detection loophole. In doing so, it is usually one of two methods that is adopted. The first method is based on direct photon detection and yields binary output depending on whether at least one photon is detected. Despite reports of high efficiencies with some nontrivial setups [61], the overall efficiency, including the *a posteriori* entanglement generation, is very low, thereby rendering Bell tests inconclusive. The second method is to bypass photon counting altogether and instead take advantage of the high efficiency of homodyne detection [62, 63, 32, 64, 65, 66]. In this case, quadrature data are sorted into binary outcomes depending on their amplitude. The successful implementation of homodyning schemes has, however, been hampered by weak margins of violations and the complexity of preparing the required states.

John Bell's discovery [55] opened up a whole subfield of research where the name of the game is to achieve larger and more conclusive violations of LHV-abiding inequalities. The initial formulations of Bell tests were statistical in the sense that the correlations involved had to be evaluated from ensemble measurements. A conceptual breakthrough was achieved when Greenberger, Horne, and Zeilinger (GHZ) proved that a certain class of states could achieve logical contradictions between measurement outcomes modeled with a LHV theory and with quantum mechanics, respectively. This came to be known as the "all-versus-nothing proof" of nonlocality [22, 67] since, superficially, a single measurement suffices to obtain the contradictory result. In reality, however, one also has to ascertain that the prepared state also fulfills a set of deterministic correlations, thereby effectively making the experimental tests of Bell inequalities and "all-versus-nothing proofs" rather similar. Initially "all-versus-nothing" proofs were thought to be exclusive to GHZ states, whereby N modes populated each by a single particle are superposed to N vacuum modes (where $N \geq 3$).

There exists another class of states consisting of a single particle symmetrically distributed over N modes, the so-called W states, which can neither be transformed into, nor obtained from, a GHZ state via local operations and classical communication. The most salient difference between the W and the GHZ is that the former are far more robust to noise admixtures

and are therefore of practical interest to quantum information protocols [68, 69, 70]. It then came as good news that, in addition to being robust to de-coherence, the W state also displays an effectively "all-versus-nothing" nonlocality as the number N of delocalizations of the single particle goes up [37] [1]. Given the ease with which W states can be produced, this finding puts them forth as promising candidates in the quest to close the detection loophole that has plagued Bell tests, particularly in the optical regime. We will show in this chapter, however, that the violation of locality by W states does not scale as hoped for with larger N when one includes de-coherence or detection inefficiencies. In other words, the "all-versus-nothing" violations that seemed attractive at extreme delocalizations $N \gg 2$ are quickly offset by a degradation of nonlocality under realistic conditions.

The outline of this chapter is as follows. We describe the W state in Sec. 4.2.1 and derive its diluted form which will be needed to simulate experimental imperfections such as losses and detection inefficiencies. We then recapitulate the Bell inequality and its associated measurements in Sec. 4.2.2. The measurement process is formalized in Sec. 4.3 with the use of of optimal positive operator-valued measures (POVM). The operators we present are optimal in the sense that, notwithstanding losses and detection inefficiencies, they perform the required projectors deterministically and accurately. Virtually no laboratory device can project optimally, but we expressly choose this best-case scenario in our derivations to prove that the "all-versus-nothing" behavior hoped-for in [37] is not possible with any realistic measurement device. The results of our simulations are summarized in Sec. 4.4 where we also briefly present what happens when one uses hybrid Bell measurements involving photon counting and quadrature binning.

[1] Note that the precedence of realism over locality, as suggested in [37], has been criticized in [G. C. Ghirardi, e-print arXiv:1101.5252 (2011)]. This sublte yet crucial point was emphasized by J. S. Bell himself in that locality is the sole assumption of his inequalities [71].

4.2 Realistic Bell test

4.2.1 The attenuated W state

The W state consists of a single particle that is symmetrically distributed over N modes. In its pure form, it reads

$$|W\rangle = \frac{1}{\sqrt{N}} \sum_{k=1}^{N} |\gamma_k\rangle, \tag{4.1}$$

where $|\gamma_k\rangle \equiv |0\rangle^{\otimes k-1} \otimes |1\rangle \otimes |0\rangle^{\otimes N-k}$ represents a photon at the kth mode, all other modes remaining empty. It is written in matrix notation as

$$\hat{\rho}_W = \frac{1}{N} \sum_{i=1}^{N} \sum_{j=1}^{N} |\gamma_i\rangle\langle\gamma_j|. \tag{4.2}$$

The above is a pure state which will inevitably suffer de-coherence under realistic conditions. Not only will it undergo mixing and losses in preparation and transmission, but its very characterization will also incur detection inefficiencies. All these "real-world" effects can be bundled together in a generic de-coherence factor at each of the modes. We do this by simulating a fictitious beam splitter of transmission η_k^2 at each mode k of the N-mode system. η_k^2 can thus be interpreted as both the transmission efficiency of mode k and the quantum efficiency of any measurement that is ultimately performed on it. The initially pure W state (4.2) effectively turns into the mixed state

$$\begin{aligned} \hat{\rho}'_W &= \frac{1}{N} \sum_{i=1}^{N} \left(\eta_i^2 |\gamma_i\rangle\langle\gamma_i| + \left(1-\eta_i^2\right) |0\rangle^{\otimes N} \langle 0|^{\otimes N} \right) + \\ &\quad \frac{1}{N} \sum_{i=1}^{N} \eta_i \sum_{j=i+1}^{N} \eta_j \left(|\gamma_i\rangle\langle\gamma_j| + |\gamma_j\rangle\langle\gamma_i| \right). \end{aligned} \tag{4.3}$$

In deriving the above state, we have only taken into account the attenuating effect of the environment. A more thorough modeling of real-world effect would include dark counts in detection or incoherent photon admixtures from thermal baths. Such noise sources shall be ignored without compromising the main objective of our paper, i.e., to prove that nonlocal components of the W state are vulnerable to loss.

From an experimental point of view, it is worth highlighting the relative ease with which W states can be prepared in comparison to, say, GHZ

states. It indeed suffices to send a single photon into two beam splitters with reflectivities of $\frac{1}{3}$ and $\frac{1}{2}$, respectively (Fig. 4.1a). A remote preparation can also be implemented in order to avoid transmitting the W state through lossy channels (Fig. 4.1c) [72, 73].

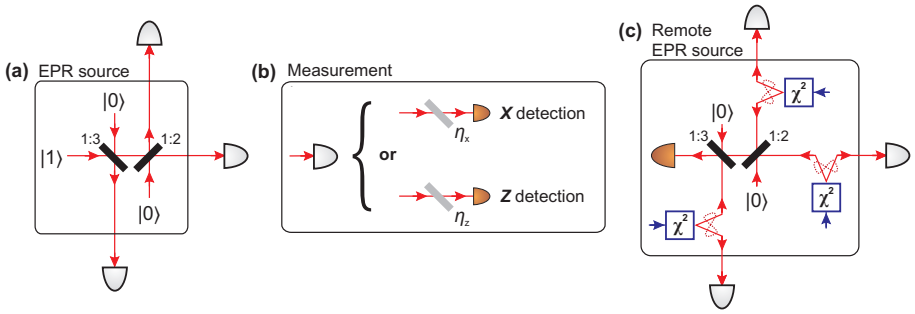

Figure 4.1: **Experimental setup for the tripartite example ($N = 3$).** **a,** Conceptual setup for the preparation of the W state. A single photon is fed into two consecutive beam splitters of reflectivities $\frac{1}{3}$ and $\frac{1}{2}$, respectively. The generation of the input single photon can be achieved by heralding one photon from the pair emitted via spontaneous parametric down-conversion (SPDC). Any inefficiency of the heralding detector will not affect the purity of the produced state, but will simply reduce its generation rate. **b,** Measurement scheme. Each of the three modes that emerge are randomly measured in either one of two ways: By a projection on $\hat{Z}$, or by a projection on $\hat{X}$. Fictitious beam splitters, drawn here in gray, are merely used as mathematical models for inefficient detection. If one works with optimal detectors, then the effectively measured state is given by (4.3). **c,** Remote preparation of the W state. Three weak squeezers (labeled χ^2) produce a state $p_0|00\rangle + p_1|11\rangle$ (with $p_0 \gg p_1$) where one mode from each is sent "backwards" to the same beam splitter arrangement as in (**a**) for entanglement with the other two. Upon detection of a single photon, the remote modes collapse to a W state.

4.2.2 The Bell inequality

The Bell factor Ω pertaining to W states was initially derived in [74] and extended to the N-partite case in [37]. Any model that satisfies the inequality $\Omega > 0$ has a probability Ω of contradicting locality. For a permutationally-symmetric state such as the W, a closed-form expression for the Bell factor

is given by

$$\begin{aligned}\Omega &= N \cdot P(z_1 = -1, z_2 = \ldots = z_N = +1) \\ &\quad -(N)_2 \cdot P(x_1 = +1, x_2 = -1, z_3 = \ldots = z_N = +1) \\ &\quad -P(x_1 = \ldots = x_N = +1) \\ &\quad -P(x_1 = \ldots = x_N = -1) \end{aligned} \tag{4.4}$$

where $(N)_2 = N(N-1)$ is the number of permutations of any pair of modes over a total of N. The function P is the probability of projecting the W state on a set of Pauli operators $\hat{X}$ or $\hat{Z}$ so as to achieve the eigenvalues specified as arguments. The subscript on the eigenvalues labels the measured mode. In the Fock basis, the eigenvalue equations of the $\hat{X}$ and $\hat{Z}$ operators are

$$\begin{cases} \hat{Z}|0\rangle = +1|0\rangle, \hat{Z}|1\rangle = -1|1\rangle, \text{ and} \\ \hat{X}\left[\frac{1}{\sqrt{2}}\left(|0\rangle \pm |1\rangle\right)\right] = \pm\frac{1}{\sqrt{2}}\left(|0\rangle \pm |1\rangle\right). \end{cases} \tag{4.5}$$

We shall return to the formal representation of these operators in the next section. For now, it can be seen that $\hat{Z}$ is essentially a binary photon detector which takes on eigenvalue $+1$ or -1 depending on whether a photon is measured. $\hat{X}$ is not an operator in the energy basis, it could however be aligned with the Fock basis via a Hadamard rotation as proposed in [37]. That said, we shall abstract these operators from their physical implementation. Instead, we assume that optimal POVM's exist for $\hat{Z}$ and $\hat{X}$ and that one could in principle perform unambiguous projections reproducing (4.5). Recall, however, that our use of optimal POVM's does not dispense us from detection inefficiencies; these have already be taken into account in the derivation of the diluted state $\hat{\rho}'_W$ above.

4.3 Optimal POVM

Consider a generic qubit consisting of an equal superposition of a single photon and the vacuum

$$|\psi_{\theta,\phi}\rangle = \cos(\theta)|0\rangle + \sin(\theta)e^{i\phi}|1\rangle, \tag{4.6}$$

where θ and ϕ are, respectively, the azimuthal and equatorial coordinates on the Bloch sphere. From now on, we shall ignore the equatorial dimension and only work on the circle spanned by θ. The POVM which optimally projects on $|\psi_\theta\rangle$ is represented in the Fock basis as

$$\hat{\Pi}_\theta = |\psi_\theta\rangle\langle\psi_\theta| = \begin{bmatrix} \cos^2(\theta) & \cos(\theta)\sin(\theta) \\ \sin(\theta)\cos(\theta) & \sin^2(\theta) \end{bmatrix}. \tag{4.7}$$

The projective probability $P_{q,\theta}$ of any qubit $\hat{\rho}_q$ on $\hat{\Pi}_\theta$ is therefore given by

$$P_{q,\theta} = \mathrm{Tr}\left\{\hat{\Pi}_\theta \cdot \hat{\rho}_q\right\}. \tag{4.8}$$

Going back to the two projections of interest to us, the measurement operators satisfying the eigenvalue equations (4.5) are

$$\begin{aligned} \hat{\Pi}_z^+ &= \hat{\Pi}_0 = \begin{bmatrix} 1 & 0 \\ 0 & 0 \end{bmatrix}, \hat{\Pi}_z^- = \hat{\Pi}_{\frac{\pi}{2}} = \begin{bmatrix} 0 & 0 \\ 0 & 1 \end{bmatrix}, \text{ and} \\ \hat{\Pi}_x^+ &= \hat{\Pi}_{\frac{\pi}{4}} = \begin{bmatrix} \frac{1}{2} & \frac{1}{2} \\ \frac{1}{2} & \frac{1}{2} \end{bmatrix}, \hat{\Pi}_x^- = \hat{\Pi}_{\frac{7\pi}{4}} = \begin{bmatrix} \frac{1}{2} & -\frac{1}{2} \\ -\frac{1}{2} & \frac{1}{2} \end{bmatrix}, \end{aligned} \tag{4.9}$$

where the superscript on $\hat{\Pi}$ indicates the sign of the eigenvalue.

4.4 Results and discussion

4.4.1 Best-case scenario

With the POVM's for $\hat{Z}$ and $\hat{X}$ projections at our disposal, the computation of Bell's factor (4.4) is given by its constituent probabilities, which are themselves N-mode extensions of (4.8):

$$P(z_1 = -1, z_2 = \cdots = z_N = +1) = \mathrm{Tr}\left\{\left[\hat{\Pi}_z^- \otimes \left(\hat{\Pi}_z^+\right)^{\otimes N-1}\right] \cdot \hat{\rho}'_W\right\}, \tag{4.10}$$

$$P(x_1 = +1, x_2 = -1, z_3 = \cdots = z_N = +1) = \mathrm{Tr}\left\{\left[\hat{\Pi}_x^+ \otimes \hat{\Pi}_x^- \otimes \left(\hat{\Pi}_z^+\right)^{\otimes N-2}\right] \cdot \hat{\rho}'_W\right\}, \tag{4.11}$$

$$P(x_1 = \cdots = x_N = \pm 1) = \mathrm{Tr}\left\{\left[\hat{\Pi}_x^\pm\right]^{\otimes N} \cdot \hat{\rho}'_W\right\}. \tag{4.12}$$

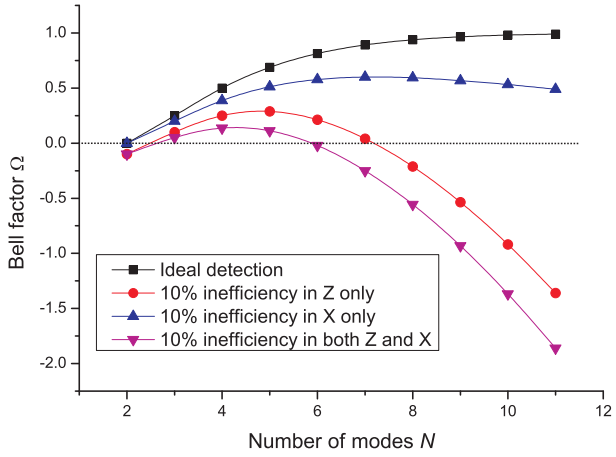

Figure 4.2: Scaling of the Bell factor with the number N of delocalized modes. Four scenarios are considered regarding the detection inefficiencies: ideal detection (squares), 10% detection inefficiency in $\hat{Z}$ (circles), 10% detection inefficiency in $\hat{X}$ (upward triangles), 10% detection inefficiency in both $\hat{Z}$ and $\hat{X}$ (downward triangles). It is worth noting that inefficiencies in $\hat{Z}$ are more detrimental to the Bell factor than inefficiencies in $\hat{X}$.

Evaluating the above probabilities yields the analytical expression

$$\begin{aligned}\Omega(\eta_z,\eta_x) &= \frac{\eta_z^2}{2}\left(3+\frac{N^2}{2}-\frac{3}{2}N\right)-2^{1-N}-\frac{N^2}{4}+\frac{N}{4}\\ &\quad+\eta_x^2\left(\frac{N}{2}+2^{1-N}-2^{1-N}N-\frac{1}{2}\right),\end{aligned} \tag{4.13}$$

where η_z^2 and η_x^2 are the efficiencies of the $\hat{Z}$ and $\hat{X}$ measurements, respectively.

In the ideal case, the Bell factor reduces to

$$\Omega(\eta_z=\eta_x=1)=1-\frac{N}{2^{N-1}}. \tag{4.14}$$

It is this expression (4.14) which prompted the optimism of Heaney *et al.* [37] towards the W state and its potential to exhibit robust violations of locality. However, as soon as one brings in non-unity detection efficiencies, the scaling of the Bell factor with larger N eventually curves downwards to ultimately dip beneath the locality bound. Four sample trends of the Bell factor as a function of the number of modes N are shown in Fig. 4.2.

A further insight into the scaling of the Bell factor with the number of modes N is obtained by looking at the minimum quantum efficiencies

required if any violation of locality is to be witnessed. Fig. 4.3 shows the trend in $\min(\eta_z^2)$ and $\min(\eta_x^2)$ for $\eta_x^2 = 1$ and $\eta_z^2 = 1$, respectively. The key result is that any quantum efficiency of less than either 80% for $\hat{Z}$ detection (assuming perfect $\hat{X}$) or 50% for $\hat{X}$ detection (assuming perfect $\hat{Z}$) will prohibit any display of nonlocality.

If, as suggested by Heaney *et al.* [37], the $\hat{X}$ projection is achieved by an ideal Hadamard rotation followed by a $\hat{Z}$ detection, then the effect of η_z^2 is felt on all N measurement sites. This is drawn as the upper curve on Fig. 4.3. The minimum quantum efficiency thus required by the scheme of [37] is $\eta_z^2 = 86.2\%$ for $N = 4$. Any scaling to larger N will not help in decreasing the minimum quantum efficiency.

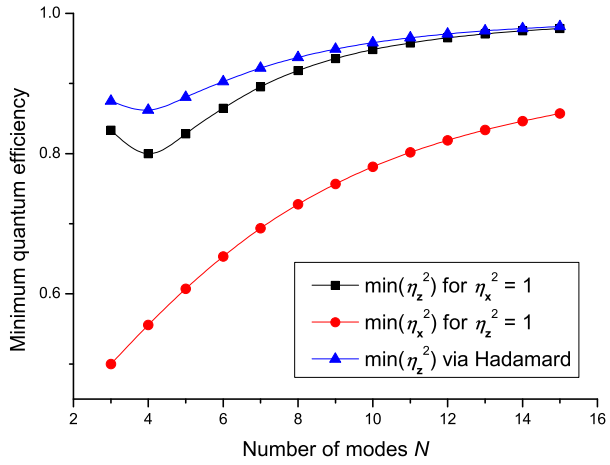

Figure 4.3: Minimum quantum efficiency for either $\hat{Z}$ or $\hat{X}$ as a function of the number of modes. These plots are obtained by solving $\Omega = 0$ in (4.13) for η_z^2 (squares) and η_x^2 (circles) while maintaining $\eta_x^2 = 1$ and $\eta_z^2 = 1$, respectively. The top curve traces the minimum quantum efficiency required of photon detectors if one is to use a Hadamard rotation to perform $\hat{X}$ measurements from $\hat{Z}$ basis (triangles).

4.4.2 Realistic scenario: Hybrid measurements

It may be worthwhile at this point to use measurement projectors for which there actually exists laboratory devices. One obvious choice for $\hat{Z}$ is the avalanche photodiode (APD) which, ignoring dark counts and inefficiencies,

clicks when at least one photon is detected. For the $\hat{X}$ operation, whose Hamiltonian is not diagonal in the energy eigenbasis, one can resort to binning continuous variables acquired by a homodyne measurement. This hybrid method of detection has been propounded recently in [75] in the context of N00N states but could conceivably be reused for other systems thanks to the high efficiency offered by homodyning.

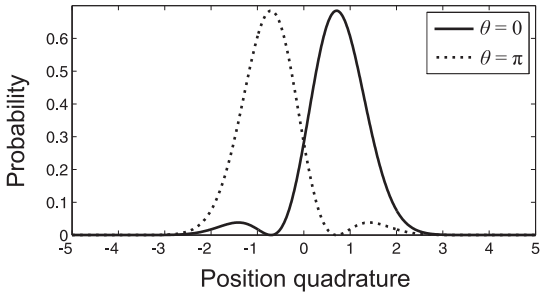

Figure 4.4: Quadrature probability distribution of the qubit $\cos(\theta)|0\rangle + \sin(\theta)|1\rangle$ for $\theta = \frac{\pi}{4}$ and $\theta = \frac{7\pi}{4}$.

Let's look at how quadrature-binning can be used to implement an $\hat{X}$-measurement. The binning is motivated by the symmetry of the quadrature probability distribution of $|\psi_{\frac{\pi}{4}}\rangle$ (i.e., $x = +1$) and $|\psi_{\frac{7\pi}{4}}\rangle$ (i.e., $x = -1$) about the zero in-phase quadrature (Fig. 4.4). We shall therefore bin our quadrature measurements by assigning $q < 0$ to $x = -1$ and $q > 0$ to $x = +1$. (Note that an ambiguity in this measurement process will arise from the overlap of the quadrature distributions.) In the Fock representation, $\hat{X}$ projections based on homodyne binning are given by

$$\hat{\Pi}_{\theta}^{\mathrm{HD}} = \begin{bmatrix} \chi_{0,0} & \chi_{0,1} & \cdots & \chi_{0,\mathrm{M}} \\ \chi_{1,0} & \chi_{1,1} & \cdots & \vdots \\ \vdots & \vdots & \ddots & \vdots \\ \chi_{\mathrm{M},0} & \chi_{\mathrm{M},1} & \cdots & \chi_{\mathrm{M},\mathrm{M}} \end{bmatrix}, \tag{4.15}$$

where $\chi_{n,m} = \int_{\Delta(\theta)} \overline{\phi_m(q)} \phi_n(q)\, \mathrm{d}q$ and $\phi_k(q) = \langle q|k\rangle$ is the quadrature probability distribution of a Fock state $|n\rangle$. M is the maximum number of photons inhabiting the measured mode and is set to $M = 1$ in the particular case of single-photon qubits we are dealing with. Note the dependence of the post-selection range $\Delta(\theta)$ on the witness qubit angle θ. In analogy to (4.8), the projective probabilities for a matrix element $|n\rangle\langle m|$ on the two

possible eigenvectors of $\hat{X}$ are

$$P_{|n\rangle\langle m|,\frac{7\pi}{4}} = \int_{-\infty}^{0} \overline{\phi_m(q)}\phi_n(q)\,\mathrm{d}q, \tag{4.16}$$

$$P_{|n\rangle\langle m|,\frac{\pi}{4}} = \int_{0}^{\infty} \overline{\phi_m(q)}\phi_n(q)\,\mathrm{d}q. \tag{4.17}$$

With these projective probabilities in hand, an evaluation of the Bell factor via Eqs. (4.10)-(4.12) yields

$$\begin{aligned}\Omega_{\mathrm{hybrid}}(\eta_{\mathrm{APD}},\eta_{\mathrm{HD}}) &= \frac{\eta_{\mathrm{APD}}^2}{4}\left(N^2-3N+6\right)\\ &\quad+\frac{\eta_{\mathrm{HD}}^2}{\pi}\left(2^{2-N}+N-2^{2-N}N-1\right)\\ &\quad+\frac{1}{4}\left(N-N^2-2^{3-N}\right),\end{aligned} \tag{4.18}$$

where $\eta_z^2=\eta_{\mathrm{APD}}^2$ and $\eta_x^2=\eta_{\mathrm{HD}}^2$ are the quantum efficiencies of the APD and homodyne detectors (HD), respectively.

Fig. 4.5 shows the scaling of the Bell factor with N. One predictable observation is that the experimental evaluation of the Bell factor with this hybrid scheme leads to much smaller violation margins than those obtained by optimal POVM's. Of particular relevance to the present chapter is the fact that scaling to larger N is not monotonic: Even with unit efficiencies, the Bell factor barely skims the nonlocality bound, peaks at $\max(\Omega_{\mathrm{hybrid}})\approx 0.09$ for $N=4$ then plunges back in the locality range for $N\geq 6$. Physically, this weak violation margin is explained by the fact that (4.15) is really an approximate projector: The two orthogonal qubits $|\psi_{\frac{\pi}{4}}\rangle$ and $|\psi_{\frac{7\pi}{4}}\rangle$ cannot be perfectly resolved by homodyne measurements because of their overlapping quadrature wave functions (cf. Fig. 4.4).

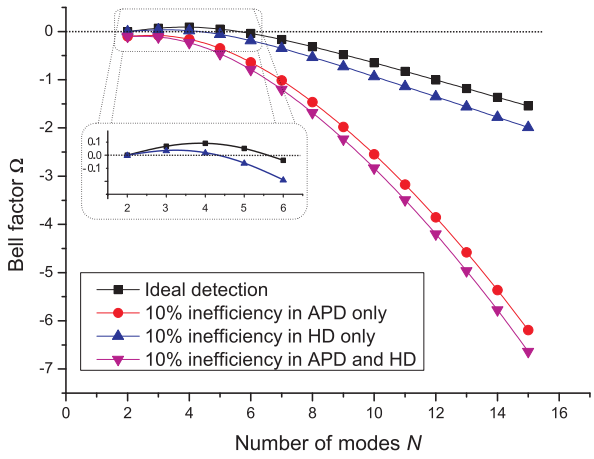

Figure 4.5: Scaling of the Bell factor with the number N of delocalized modes in the case of hybrid detection involving an APD for $\hat{Z}$ and homodyne thresholding for $\hat{X}$. Four scenarios are considered regarding the detection inefficiencies: ideal detection (squares), 90% quantum efficiency for the APD (circles), 90% detection efficiency for the homodyne detector (upward triangles), and 90% detection efficiency for both detectors (downward triangles).

The scaling of the minimum quantum efficiencies required to violate Bell's inequality are shown in Fig. 4.6. The most salient result is that nonlocality cannot be shown by the hybrid measurement scheme described above for any system with $N \geq 6$. Indeed, the "minimum quantum efficiencies" beyond $N = 5$ take on unphysical values above unity. The increase of the violation margin with larger N has therefore been overwhelmingly offset by a decrease in purity. The best result that can be achieved is for $N = 3$ where the minimum quantum efficiencies required are 95% for the APD (assuming ideal homodyning) or 79% for the the homodyne detector (assuming ideal photon detection).

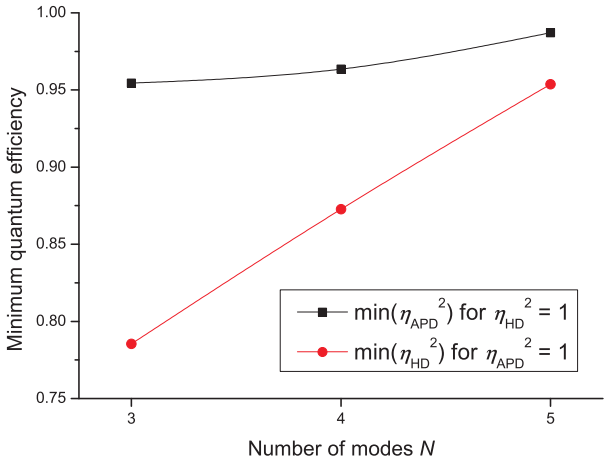

Figure 4.6: Minimum quantum efficiency for either the APD or the homodyne detector (HD) as a function of the number of modes. These plots are obtained by solving $\Omega_{\text{hybrid}} = 0$ in (4.18) for η^2_{APD} (squares) and η^2_{HD} (circles) while maintaining $\eta^2_{\text{HD}} = 1$ and $\eta^2_{\text{APD}} = 1$, respectively.

4.5 Conclusion

We have shown that in the context of demonstrating nonlocality with W states, the transition from theory to experiment is not only quantitative, but also qualitative. Both the Bell inequality and the "all-versus-nothing" violation of locality which could effectively have been achieved by W states for large N turns out to be invalidated by a minute amount of de-coherence, even if the projective measurements were optimal. In practice, one would have to make the unrealistic assumption that perfect Hadamard rotations can be used on Fock state superpositions. Even then, the minimum quantum efficiency for photon detection would have to be 86.2%. Such severe requirements can only be met by demanding detection setups (e.g., transition-edge sensors [76]). The burden on quantum efficiency has therefore been shown not to benefit in any appreciable way from large delocalizations of a single quantum. The situation is predictably worse when one uses approximate projectors to perform the Pauli projector $\hat{X}$: A minimum quantum efficiency of 95% is required of the photon counters if the Bell measurements are performed with a hybrid scheme involving quadrature binning.

Note: It has come to our attention that similar work has very recently been published by Chaves and Bohr Brask in [77]. The main difference with our treatment lies in a slight variation of the inequality under considera-

tion: They include a positive term in their inequality which leads to higher violations and therefore lowers the requirement on quantum efficiency.

Chapter 5

Amplification of cat states by homodyne heralding

We present a scheme for the amplification of Schrödinger cats that collapses two smaller states onto their constructive interference via a homodyne projection. We analyze the performance of the amplification in terms of fidelity and success rate when the input consists of either exact coherent state superpositions or of photon-subtracted squeezed vacua. The impact of imprecise homodyne detection and of impure squeezing is quantified. We also assess the scalability of iterated amplifications.

Coherent state superpositions, or optical Schrödinger cat states, are widely recognized as promising resources in quantum information [78, 7, 79, 80, 13], quantum metrology [81, 82, 83], and fundamental tests [84, 85, 86, 87]. In the near-orthogonal basis of coherent states $\langle\gamma|-\gamma\rangle = e^{-2\gamma^2}$, two particular instances for these states are

$$|\kappa_{\pm}(\gamma)\rangle = \frac{1}{\sqrt{2 \pm 2e^{-2|\gamma|^2}}} \left(|\gamma\rangle \pm |-\gamma\rangle\right), \tag{5.1}$$

where the sign ($\pm$) of the superposition refers to the even and odd cat state, respectively. These states exhibit quasi-probability distributions in phase space which are distinctly non-classical. This makes them all the more challenging to generate deterministically as that would require strong Kerr-type non-linearities [88, 89, 90]. One has then to resort to heralding techniques which, though probabilistic, need only linear optics and projective measurements [91]. These state-engineering schemes are nonetheless approximative and present a limitation in the fidelity they produce with ideal cat states. Photon-subtraction of squeezed vacuum, for example, is a

well-established method to generate approximations of small amplitude cat states, colloquially referred to as Schrödinger *kittens* [92, 93, 94, 14, 95]. Even in the best experimental conditions, the fidelity between the photon-subtracted squeezed vacuum (PSSV) and an actual odd cat state $|\kappa_-(\gamma)\rangle$ degrades markedly for $\gamma \geq 1.2$ [96]. Yet, for these states to be reliable resources in quantum computation, their fidelity with cat states at least as large as $\gamma = 1.2$ need to be maintained at near-unit fidelity [79, 97].

Single-photon subtraction is only one example of several measurement-induced schemes which have been proposed to generate kitten states [98, 99, 14, 100, 101, 102, 103]. However, none of these schemes can produce arbitrarily large cats in a single run. Ways to get around this issue have been devised using the recursive amplification of small, approximate cats [104, 105]. For example, it was suggested in [106] to interfere a supply of delocalized single photons followed by homodyne heralding to generate large entangled cat states. These proposals have in common that they rely on the coherent mixing of two small cats, whereupon a projective measurement collapses one of the two outputs onto a *constructive interference* of the inputs—hence the amplification. Here, we shall pursue the same idea but make use solely of homodyne heralding for its relative simplicity and high quantum efficiency. We also demonstrate that the acceptance window of homodyne heralding can be widened to increase the success rate of the amplification while at the same time maintaining a satisfactory fidelity at the output.

The outline of this chapter is as follows. In Sec. 5.1 we review the generation of odd kitten states from squeezed vacuum. The output is compared to the ideal odd cat state and the effects of impure squeezing are illustrated. In Sec. 5 we present the amplification scheme in the case of ideal input cats and model the effect of a wide homodyning window. Sec. 5.3 then considers the amplification of the more realistic PSSV. The impact of both impure squeezing and wide post-selection is illustrated. In 5.4, we return to the idealized case of ideal homodyning and pure squeezing to consider how our scheme scales with iterated amplifications.

5.1 Approximation of small odd cats

In this section, we shall briefly review the generation of odd kitten states from the photon-subtraction of squeezed vacuum and analyze its performance in the face of impure squeezing. The basic setup is depicted in Fig. 5.1. The original proposal of Dakna *et al.* [92] required that the photon

subtraction be performed by photon-number resolving detectors. However, as is done in most practical schemes [93, 95, 94], we shall assume that the post-selection is a binary detection of either zero photons or at least one photon, as would be allowed for by an avalanche photodiode (APD). The modeling of such an "on-off" post-selection operation is presented in Sec. 2.5.

Quantum inefficiencies and dark counts are two nuisances inherent to photodetection which should be reckoned with. Whereas the former merely affects the success probability of the scheme, the latter contaminates the output with a squeezed vacuum component which weakens the nonclassicality of the output. An equally detrimental effect is the impurity of the squeezed vacuum. We shall not treat quantum inefficiencies and dark counts here as they have already been covered in [91] in the context of cat amplification. We will however look at the fidelity response to the amplitude and impurity of squeezing.

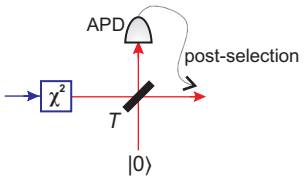

Figure 5.1: Setup for the generation of approximate small odd cat states. A squeezed vacuum, represented here by the pumping of a χ^2 nonlinear medium, is partially reflected onto an "on-off" photon detector such as an avalanche photodiode (APD). Upon the reflection of at least one photon from the squeezed vacuum, a state that likens the squeezed single photon is prepared in the limit of unit transmission $T \to 1$.

5.1.1 Fidelity of the output for pure squeezing

Let's assume from now on that the squeezed vacuum is pure and anti-squeezed in the x-quadrature. I.e., if we denote the squeezing relative to the shot noise variance by ξ (in dB), then $\xi_x = -\xi_p > 0$, where the subscript labels the measured quadrature [1]. The fidelity of the PSSV state with an ideal cat state $|\kappa_-(\alpha)\rangle$ then depends on the squeezing ξ and the transmission T of the subtraction beam splitter [2]. The effect of these parameters is

[1] For simplicity, we shall refer to both squeezing and anti-squeezing as *squeezing* ξ. The difference between the two is only made by the sign of ξ

[2] The transmission of the subtraction beam splitter does not just affect the success probability of the scheme, but also the fidelity of the output state. This is because we are

illustrated in Fig. 5.2 where we can see that the fidelity is optimized for low squeezing and near-unit beam splitter transmission $T \to 1$. For any given input squeezing, there corresponds a finite amplitude α of the target cat with which the output has an maximized fidelity. For example, a squeezing of, say, 3 dB is optimal for producing an approximation to a cat state of size $\alpha = 1.0$. A complementary investigation of PSSV states that looked at nonclassicality as the main figure of merit (as opposed to fidelity) is given by Kim *et al.* in [107].

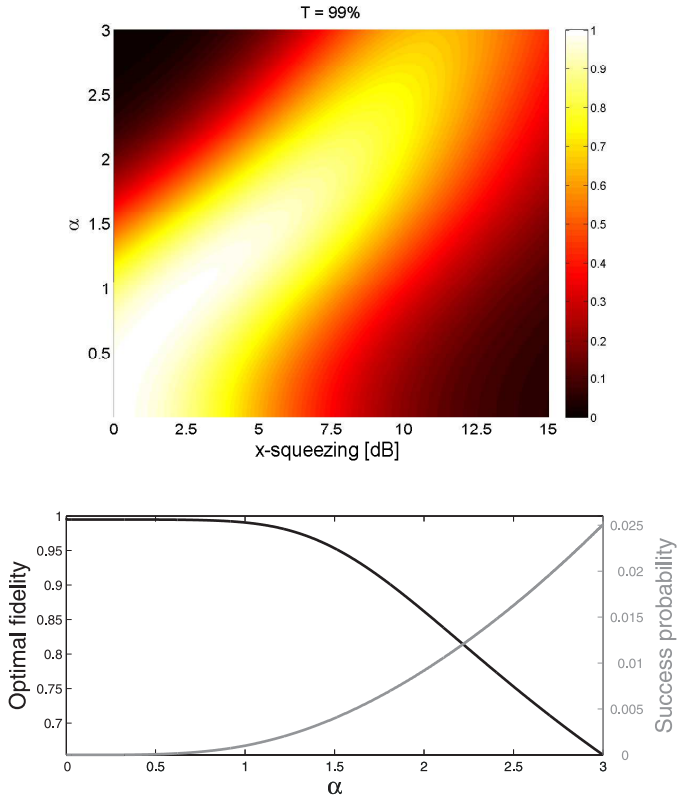

Figure 5.2: *Top*: Contour plot of the fidelity of the PSSV state with $|\kappa_-(\alpha)\rangle$ given an input squeezing ξ_x between 0 and 15 dB. *Bottom*: Maximum achievable fidelity of the PSSV with $|\kappa_-(\alpha)\rangle$ (black) and corresponding success probability as a function of α (gray). In both cases, the transmission of the subtraction beam splitter is 99%.

using an "on-off" post-selection where we assume that by setting $T \to 1$, only one photon will makes its way to the APD. A lower transmission would furthermore inflict higher loss of the initial squeezed state.

In order to assess the performance of the PSSV generation, it is most instructive to restrict ourselves to the maximal fidelity achievable with any target cat of size α. This fidelity optimum is traced by the ridge of Fig. 5.2 (top) and its α dependence is reproduced in Fig. 5.2 (bottom) along with the corresponding success rate. For example, if one wants to produce an approximate odd cat state of size $\alpha = 1.5$, the required squeezing should be $\xi \approx 5.2$ dB for a fidelity of at most 95.4% and a success probability of 0.4%.

As far as the success probability is concerned, it can be increased at the expense of fidelity by increasing the incidence of photons on the APD via stronger squeezing or weaker beam splitter transmission.

5.1.2 Impact of impure squeezing

In any real world experiment, noise will inevitably inflate the variance of the squeezed vacuum in either quadrature. This impurity has been explained as stemming from losses or from multimode parametric down-conversion [108] whereby the photons triggering the post-selection belong to a different spatial or frequency mode than the heralded state. Impure squeezing may originate in the down-converter itself or, more generally, at any point in the setup where vacuum contamination or modal mismatch could take place, including at the detectors (e.g., via quantum inefficiencies). Regardless of its root causes, we shall wrap these impurities into a single parameter ϵ relating the squeezing ξ in dB of the x- and p-quadratures,

$$\xi_x = -\epsilon \xi_p, \tag{5.2}$$

whereby pure squeezing corresponds to $\epsilon = 1$. As derived below, the purity of the squeezed vacuum is given by

$$\mathcal{P} = 10^{-\frac{1}{20}(1-\epsilon)\xi_p}. \tag{5.3}$$

Note that the Heisenberg uncertainty relation imposes that $\epsilon \geq 1$.

The impact of impurity on fidelity is plotted in Fig. 5.3 where we set the squeezing at -3.0 dB and adjust the anti-squeezing according to four different settings of purity. The immediate observation is that a decrease of 10% in purity, from 100% to 90%—corresponding to an increase of anti-squeezing to +3.9 dB from +3.0 dB, leads to a drop of the maximum fidelity of nearly 32%.

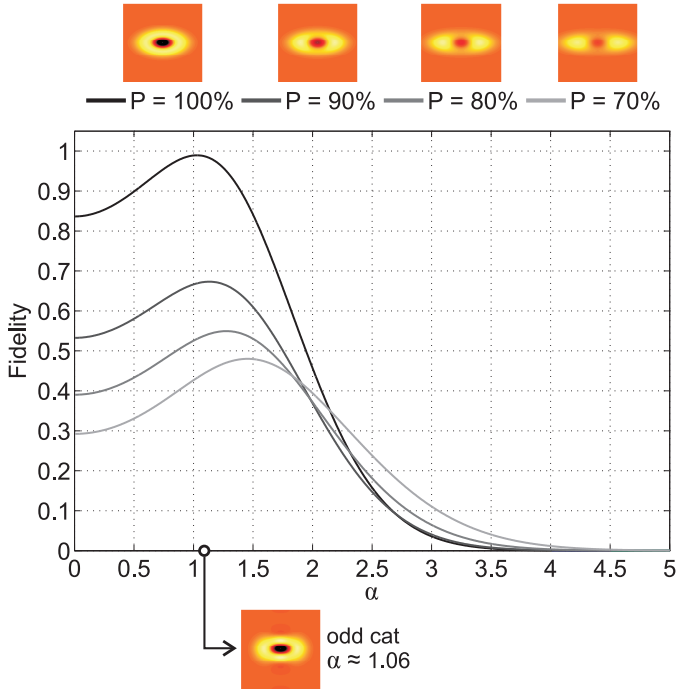

Figure 5.3: Fidelity between an ideal cat state $|\kappa_-(\alpha)\rangle$ and the kitten states obtained from squeezed vacuum $\xi_p = -3$ dB at four squeezing purities $\mathcal{P}$ (marked in decreasing darkness of gray): 100%, 90%, 80% , and 70%. The Wigner functions of the PSSVs corresponding to these four purities are shown at the top. As a reference of what the "ideal" output ought to look like, the Wigner function of the state $|\kappa_-(1.06)\rangle$, which has the highest fidelity with the PSSV obtained from pure squeezing, is shown at the bottom. The transmission of the subtraction beams splitter is set at 99%.

Purity of the squeezed vacuum. Let the variance of the vacuum phase space distribution be labeled by V_0. As is treated more formally in §2.5, the squeezing operation along a quadrature q consists of a re-scaling of phase space $q \to s_q q$ where $s_q = \sqrt{V_q/V_0}$ such that the new variance along q is V_q. The relationship between the dimensionless re-scaling factor s_q and the squeezing ξ_q (in decibels) is given by

$$\xi_q = 10 \log_{10} \frac{V_q}{V_0} = 20 \log_{10} s_q \Leftrightarrow s_q = 10^{\xi_q/20}. \tag{5.4}$$

The purity of a state of Wigner function W is given by

$$\mathcal{P} = 2\pi \iint W^2 \, \mathrm{d}x\mathrm{d}p, \tag{5.5}$$

and the Wigner function of a squeezed vacuum state $\hat{S}|0\rangle$ is

$$W_{\hat{S}|0\rangle}(x,p) = \frac{1}{\pi s_x s_p} e^{-(x/s_x)^2-(p/s_p)^2}. \tag{5.6}$$

The purity of squeezed vacuum can therefore be shown to be

$$\mathcal{P} = \frac{1}{s_x s_p} = 10^{-\frac{1}{20}(\xi_x+\xi_p)}, \tag{5.7}$$

hence equation (5.3).

5.2 Amplification of ideal odd cats

In Fig. 5.4 we present our amplification setup: Two identical cats are mixed on a balanced beam splitter whereupon one of the ensuing modes heralds the amplified output based on the measurement of x-quadratures around $x = 0$. The scenario where the inputs are idealized cats of opposite parity has been outlined by Takeoka and Sasaki in [105]. We will however look at the more practical case where the input have identical parity.

Let's briefly run through the evolution of the state in setup. We can readily see that the state emerging from the first balanced beam splitter contains an even cat of amplitude $\sqrt{2}$ times larger:

$$\begin{aligned} & |\kappa_\pm(\alpha)\rangle \otimes |\kappa_\pm(\alpha)\rangle \\ \rightarrow \quad & |\kappa_+(\sqrt{2}\alpha)\rangle \otimes |0\rangle \pm |0\rangle \otimes |\kappa_+(\sqrt{2}\alpha)\rangle. \end{aligned} \tag{5.8}$$

If, by measuring one of the modes, we can post-select $|0\rangle$ from $|\kappa_+(\sqrt{2}\alpha)\rangle$, then the other mode will collapse onto the desired amplified state $|\kappa_+(\sqrt{2}\alpha)\rangle$. The accuracy of this discrimination is of course limited by the overlap of vacuum with the cat $\langle 0|\kappa_+(\sqrt{2}\alpha)\rangle$, which is however negligible for $\alpha \gg 0$. Based on the wave function profiles of the vacuum and the cat, we can see that homodyne measurement of the $x = 0$ quadrature is indeed a good way to discriminate the two states as it is where their overlap is minimized (cf. inset of Fig. 5.4).

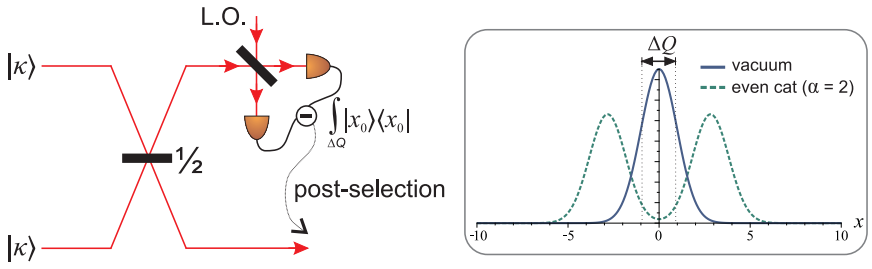

Figure 5.4: Setup for the amplification of two ideal Schrödinger cats into a larger even cat. The two inputs are mixed on a symmetric beam splitter and one of the outputs is projected onto an x-quadrature window of width ΔQ around $x_0 = 0$ by an otherwise ideal homodyne detector. *Inset*: Wave functions $\langle x|0\rangle$ (solid curve) and $\langle x|\kappa_+(2)\rangle$ (dashed curve) of the vacuum and of an even cat state of size $\alpha = 2$, respectively. The two functions are best distinguished at $x = 0$ where their overlap is minimized.

Applying the homodyne projection $|x_2 = 0\rangle\langle x_2 = 0|$ on the second mode of (5.8), we are left with

$$|\psi_{\text{out}}\rangle = \frac{e^{\alpha^2}}{2} \cdot \frac{|\sqrt{2}\alpha\rangle + |-\sqrt{2}\alpha\rangle \pm 2e^{-2\alpha^2}|0\rangle}{\sqrt{\cosh(2\alpha^2) + e^{-2\alpha^2} \pm 2e^{-\alpha^2}}}. \tag{5.9}$$

The fidelity of this state with an ideal even cat state of size β is

$$F = \text{sech}(\beta^2) \cdot \frac{\left|\cosh(\sqrt{2}\alpha\beta) \pm e^{-\alpha^2}\right|^2}{\cosh(2\alpha^2) + e^{-2\alpha^2} \pm 2e^{-\alpha^2}}. \tag{5.10}$$

In practice, a valid output is heralded whenever the homodyne detector records a state whose x-quadrature lies within a window ΔQ around $x = 0$ where ΔQ shall be expressed in shot noise units (SNUs) [3]. We keep track of such a post-selection window because no practical homodyning device has enough resolution to truly project onto an exact quadrature $|q_0\rangle\langle q_0|$. Experimentally, such a precise projection would not be desirable either for it would lead to very small success probabilities. A compromise is therefore to allow a finite post-selection range. A full model of this realistic "wide" homodyning is presented in Sec. 2.3.3.

A digression is in order at this point regarding the ambiguity of the homodyne heralding. In other words, on needs to quantify the error in

[3] By shot noise unit, we mean the standard deviation of shot noise in phase space. By setting $\hbar = 1$, this implies $SNU = \frac{1}{\sqrt{2}}$ (in absolute units of phase space quadrature).

the discrimination between the vacuum and a cat state with a homodyne projector. As mentioned above, the purpose of the homodyne measurement is to collapse the output state onto an even cat upon the detection of vacuum; cf. Eq. (5.8) and the inset of Fig. 5.4. The projector for this measurement is

$$\hat{\Pi}^{\rm hd}_{|0\rangle} = \int_{-\frac{1}{2}\Delta Q}^{\frac{1}{2}\Delta Q} |x\rangle\langle x|\,{\rm d}x. \tag{5.11}$$

Due to the intrinsic overlap of the wave functions of $|0\rangle$ and $|\kappa_+(\alpha)\rangle$, $\hat{\Pi}^{\rm hd}_{|0\rangle}$ can only act as an approximate discriminator between them. In addition, the finite width of the quadrature-selection window introduces an approximation of its own. The error in the discrimination, namely the probability of mistaking an even cat for the vacuum is given by

$$P_{\rm err} = \frac{P(|\kappa_+(\beta)\rangle)}{P(|\kappa_+(\beta)\rangle) + P(|0\rangle)}, \tag{5.12}$$

where, $P(|\gamma\rangle) = {\rm Tr}\left\{\hat{\Pi}^{\rm hd}_{|0\rangle}|\gamma\rangle\langle\gamma|\right\}$ and $|\gamma\rangle \in \{|0\rangle, |\kappa_+(\beta)\rangle\}$. Fig. 5.5 shows that the discrimination is best achieved for small ΔQ and large β. The asymptotic convergence to $P_{\rm err} = 0.5$ at large ΔQ or small β indicates a complete lack of discrimination between the states: They become equally likely to be inferred by the homodyne projector.

Let's return the the amplification scheme. From now on, we shall only consider odd cat inputs to the amplification setup. (The next section deals with approximations to odd cat inputs, namely PSSVs.) A contour plot of the fidelity between an even cat of size β and the amplified state from two odd cats of size α is shown in Fig. 5.6 for a homodyning window of 1 SNU. The $\sqrt{2}$ amplification factor that was also witnessed in earlier schemes [104, 109, 105] is recognizable as the slope $\frac{\beta}{\alpha}$ where the fidelity is optimized. The bend of this optimum crest for $\alpha \leq 1$ arises from the vacuum component which "survives" the post-selection but vanishes from the output state $|\psi_{\rm out}\rangle$ for larger α. This feature is in a sense a manifestation of the discreteness of photon numbers for weak coherent states. As can be seen from (5.9), the output consists of an even cat minus a vacuum. For $\alpha \to 0$, this "subtraction" of the vacuum component yields a state whose 2-photon component has a relatively higher weight than in any even cat of size $\beta \ll 1$. The proportionality in amplitude between input and amplified cats thus breaks down, and it is instead $|\beta \approx 1\rangle$—of all even cats—that exhibits the best fidelity with the output.

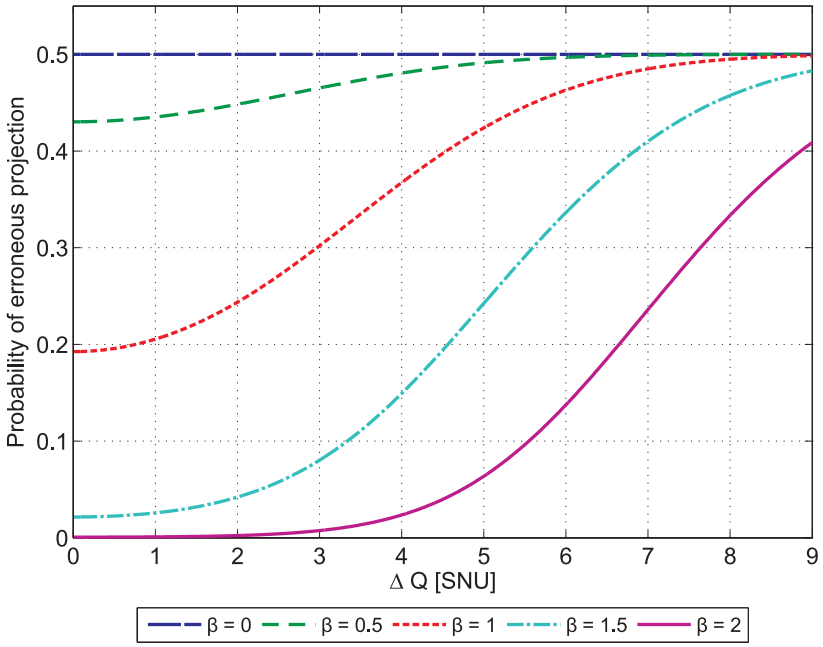

Figure 5.5: Probability P_{err} of mistaking an even cat state of size β for a vacuum state as a function of the quadrature acceptance window ΔQ.

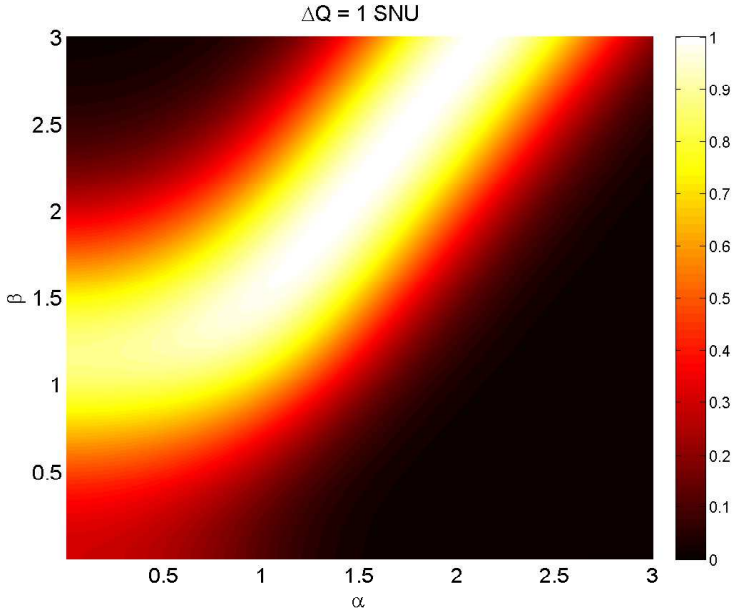

Figure 5.6: Contour plot of the fidelity between an even cat of size β and the amplification obtained from two odd cats of size α. The post-selection window is set to 1 SNU.

Just as in Fig. 5.2 for the PSSV state, it is informative to look at the mapping between input and output parameters which optimizes fidelity. This is shown in Fig. 5.7 where the optimal input state amplitude is plotted as a function of the amplitude β of the target state $|\kappa_+(\beta)\rangle$. For example, if one wants to produce an even cat state of size $\beta = 2$, then an input odd cat state of size $\alpha = 1.4$ is required. The fidelity of the output with $|\kappa_+(\beta = 2)\rangle$ will be nearly 100% and the success probability of the operation about 20%. As discussed above, the flat plateau for $\beta \leq 1$ corresponds to the range where the vacuum component that filtered through the post-selection becomes predominant. The consequence is that the single-photon "cat state", $|\kappa_-(\alpha \to 0)\rangle \approx |1\rangle$, becomes the only input to optimize outputs of target size $\beta \in [0, 1]$.

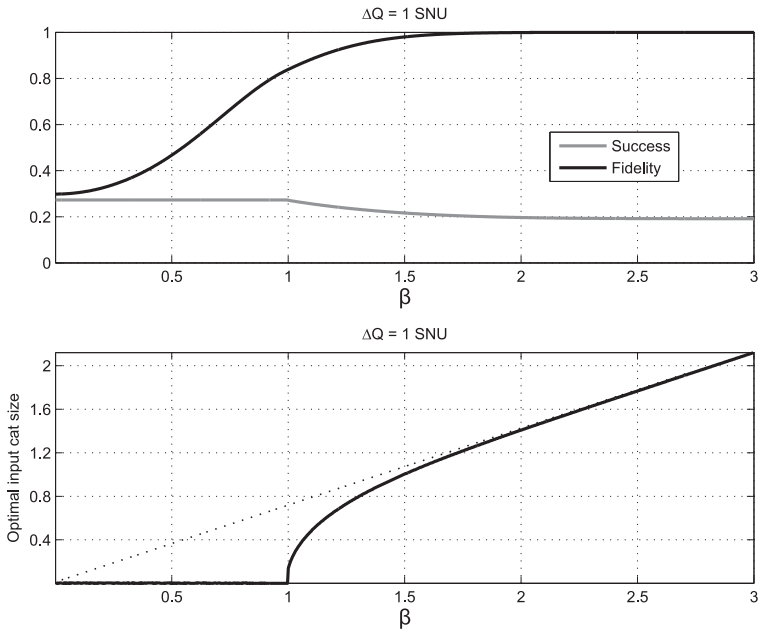

Figure 5.7: *Top*: Maximum fidelity (black) and corresponding success probability (gray) of the amplified output with respect to an even cat state of size β. *Bottom*: Amplitude α of the input required to obtain the maximum fidelity of the output with an even cat state of size β. The dotted line marks the $\sqrt{2}$ amplification factor. The homodyne post-selection window is 1 SNU wide.

To assess the robustness of the amplification scheme to the homodyning

width ΔQ, Fig. 5.8 plots the fidelity between the output produced from two odd cats $|\kappa_-(\alpha)\rangle$ and an even cat $|\kappa_+(\beta = \sqrt{2}\alpha)\rangle$ given different homodyning windows. The fidelity curve for exact homodyning $\Delta Q \to 0$ is also plotted as a reference. It can be seen that the amplification is only vulnerable to ΔQ for small inputs. Beyond a target size of $\beta \approx 3.5$, homodyning widths of up to 8 SNUs hardly have any effect on the fidelity. From an experimental point of view, this robustness of the homodyning post-selection allows one to reach higher success probabilities without compromising fidelity. For example, by sending in two odd cats of size $\alpha = 2.5$, one every two homodyne measurements will successfully herald an even cat of size $\beta = \sqrt{2} \times 2.5 \approx 3.5$ with a fidelity of nearly 100%.

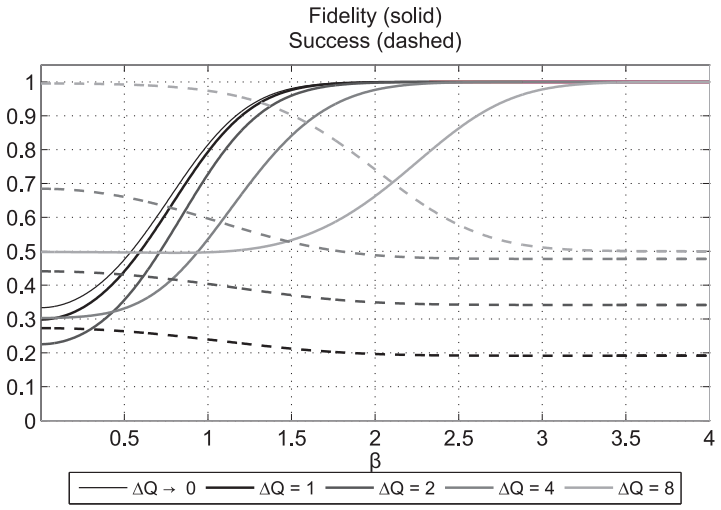

Figure 5.8: *Solid curves*: Fidelity between an even cat of size $\beta = \sqrt{2}\alpha$ and the output of mixing two odd cats of size α for five homodyning widths ΔQ (in SNUs). *Dashed curves*: Corresponding success probabilities. (The curve for $\Delta Q \to 0$ is zero throughout since the probability of picking out the exact $x = 0$ quadrature is vanishingly small.) The shading of the curves is lightens with larger homodyning windows.

For another perspective on the dependence of fidelity on homodyning width, let's consider the amplification of two odd cat states of a fixed size $\alpha = 1$. The decrease in fidelity of the output with an even cat of size $\beta = \sqrt{2}$ is traced in Fig. 5.9. Also shown are three sample Wigner profiles of the output which display a clear degradation of the negativity as ΔQ increases.

The simulations presented above, as well as all other numerical results

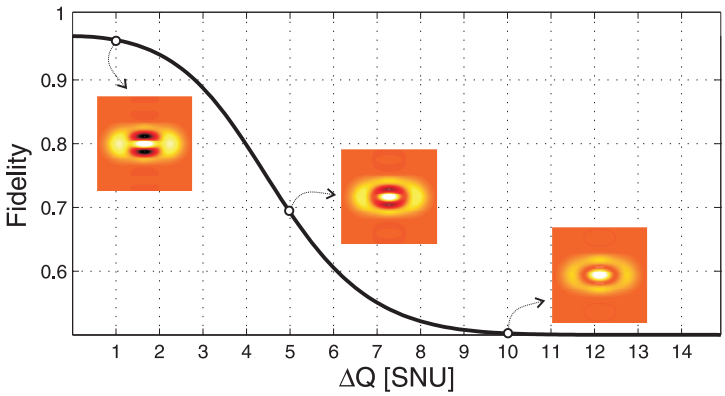

Figure 5.9: Fidelity of the state amplified from two cats of size $\alpha = 1$ with an even cat of size $\beta = \sqrt{2}$ for a homodyning window $\Delta Q \in]0, 15]$ SNU. The decrease in fidelity for wider homodyning windows is understandable from the increased overlap between the vacuum and the cat state, as illustrated in the inset of Fig. 5.4. The Wigner profile of the output is shown for three sample values of ΔQ at 1, 5, and 10 SNUs, respectively.

in this chapter are arrived at by a generic method of simulating linear transformation and projective measurements of states consisting of Gaussian superpositions (see Sec. 2.5).

5.3 Amplification of approximate small cats

In this section, we consider the more realistic case where PSSVs are amplified, i.e., the inputs to Fig. 5.4 are the outputs of Fig. 5.1. In Fig. 5.10, the fidelity profile with an even cat of size β is plotted with respect to the input (pure) squeezing for $\Delta Q = 1$ SNU and $T = 95\%$. The contour lines of PSSV generation are overlaid to visualize the amplification, i.e., the shift of the high-fidelity area upwards to larger values of β—cf. Fig. 5.2.

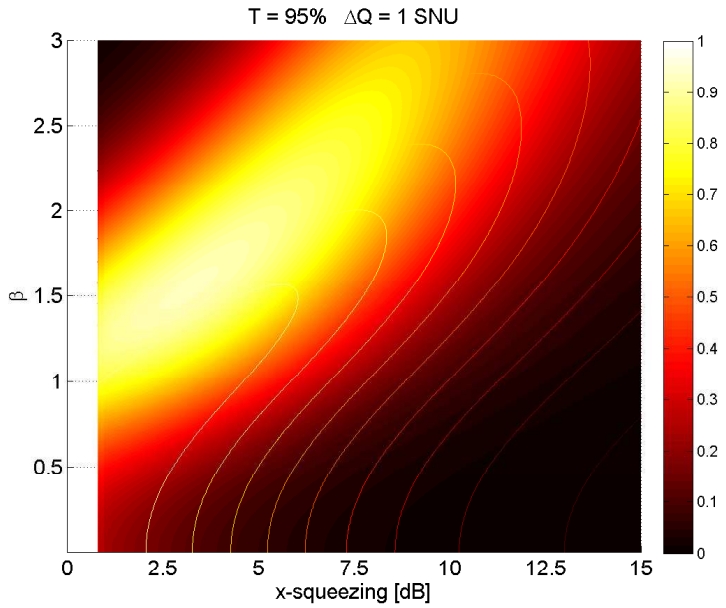

Figure 5.10: Contour plot of the fidelity between an even cat $|\kappa_-(\beta)\rangle$ and the amplified PSSV obtained from an anti-squeezing ξ_x between 0 and 15 dB. The transmission of the subtraction beam splitter is 95%. The contour lines of PSSV generation fidelity are overlaid to better visualize the shift in target amplitude β resulting from the amplification. The blank vertical stripe for $\xi_x \leq 0.8$ dB is a region where numeric underflow is too frequent to produce reliable data. (This is because the normalization factor which enters in the fidelity is itself inversly proportional to the success probability. The latter tends to negligible values for small squeezing.)

In order to assess the performance of the amplification scheme, we shall set a target even cat state of amplitude β and retrace the quantum circuit to see what input squeezing is necessary to achieve the highest fidelity with $|\kappa_+(\beta)\rangle$ at the output. This is shown in Fig. 5.11, along with the dependence of the success probability and fidelity on β, as well as the size α of the odd cat that best matches the input PSSV. Let's assume, for instance, that we want to produce an even cat of size $\beta = 1.5$. The required squeezing for the PSSV will then be around 2.9 dB, corresponding to a fidelity of 96.4% with an odd cat state of size $\alpha \approx 1.0$. The output, however, will have a fidelity of 92.6% with $|\kappa_+(\beta = 1.5)\rangle$ and the success probability of the amplification will be 20% (notwithstanding the success probability of 0.6% required to produce the "offline" PSSV).

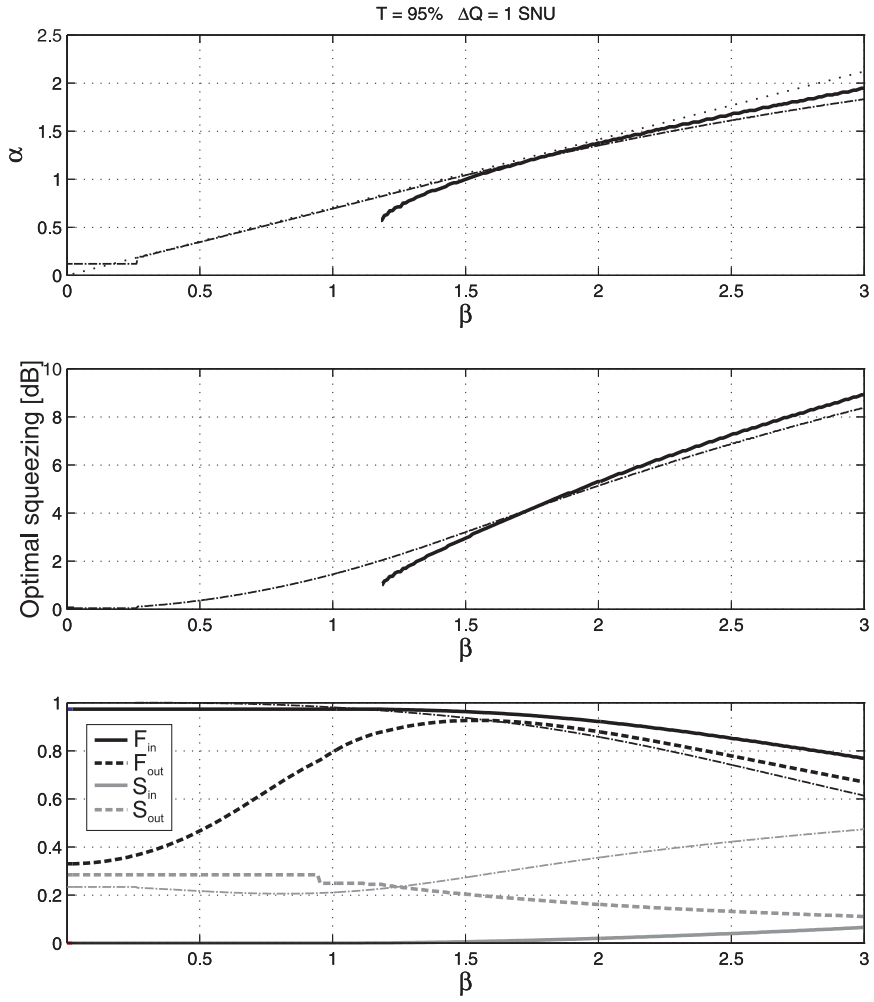

Figure 5.11: *Top*: Dependence of the effective size α of the PSSV state input on the target size β of the output such that the fidelity of the output with $|\kappa_+(\beta)\rangle$ is maximized. The dotted line marks the $\frac{\alpha}{\beta} = \frac{1}{\sqrt{2}}$ amplification ratio. The subtraction beam splitter for the PSSV generation is set to 95% and the homodyning window to 1 SNU. *Middle*: Pure squeezing required of the input in order to achieve the maximal fidelity with an even cat of size β. *Bottom*: Maximum fidelity obtainable at the output with an even cat of size β (dashed black), along with the corresponding success probability of the amplification (dashed gray). Also shown is the maximum fidelity of the required input PSSV with an odd cat of size α (solid black), and the success probability of the PSSV generation (gray black). (In all three graphs, the finer dash-dotted lines refer to the results of Lund *et al.* in [104], with, in the bottom graph, the black and gray shadings representing fidelity and success probability, respectively.)

Note that the solid curves in the first two plots of Fig. 5.11 only start at $\beta \approx 1.2$. This is because below that threshold, the optimal squeezing lies in a numerically unstable region marked the blank band in Fig. 5.10.

A first-hand observation to be drawn from Fig. 5.11 is the similarity it shows with Fig. 5.7 for small target cat sizes. Both scenarios with ideal cats and PSSV inputs start out with a fidelity around 30-35% which then increases to over 90% for targets cats of size $\beta \approx 1.5$. Beyond this point, however, the performance of PSSV amplification starts to degrade, whereas that of ideal cats can be pursued to indefinitely large target sizes while retaining unit fidelity. One conclusion is therefore that the approximation of cat states from PSSVs can be used to generate amplified states of sizes up to $\beta = 1.5$ with practically the same fidelity as if one used ideal odd cat states as inputs. On the other hand, both Figs. 5.7 and 5.11 exhibit the plateau in optimal input cat size—or in the case of PSSVs, *effective* cat size—which we discussed in the previous section. In that region, $\beta \in [0, 1]$, the ideal input cat states or PSSVs cease to have any dependence on the target size β and discrete states, namely single photons, become the optimal input state.

In addition to simulating our own amplification scheme, we have overlaid as finer dash-dotted curves the results of Lund *et al.*, which we shall refer to as the LJRK scheme [104]. Instead of using homodyning, they mix the heralding arm with a coherent state on a balanced beam splitter such that both emerging modes contain at least one photon if the heralded mode is amplified. Contrary to the homodyne method, the LJRK projection is unambiguous as it does not yield any residual vacuum component, unlike in (5.9). This explains why the fidelity in the LJRK scheme remains quasi-ideal for low target sizes β. Beyond $\beta \approx 1.5$, however, both methods are comparable in terms of fidelity and amplification factor. The homodyne method offers nonetheless experimental advantages over the photon detection of LJRK in that it does not suffer as much of quantum inefficiency or electronic noise. In particular, the need for coincident detection of photons in LJRK suppresses the success probability by the *square* of the quantum inefficiency. (The dash-dotted curve in Fig. 5.11 assumes ideal quantum efficiency.)

If one assumes ideal quantum efficiencies at the detectors, the two main nuisances to the performance of the amplification scheme are (i) the impurity $\mathcal{P}$ of squeezing, and (ii) the width ΔQ of the homodyning detection. To visualize the robustness of the scheme to these two factors, let's choose an optimal input squeezing with a target even cat of size, say, $\beta = 1.5$. From Fig. 5.11, this corresponds to $\xi_p = -2.9$ dB for a fidelity of 92.6% and a

success probability (assuming offline PSSVs) of 20%. From this reference point, the trend of fidelity and success probability varying either $\mathcal{P}$ or ΔQ is plotted in Fig. 5.12. Recall that, by convention, we model a decrease of purity by an increase in anti-squeezing (ξ_x) while maintaining squeezing proper (ξ_p) fixed.

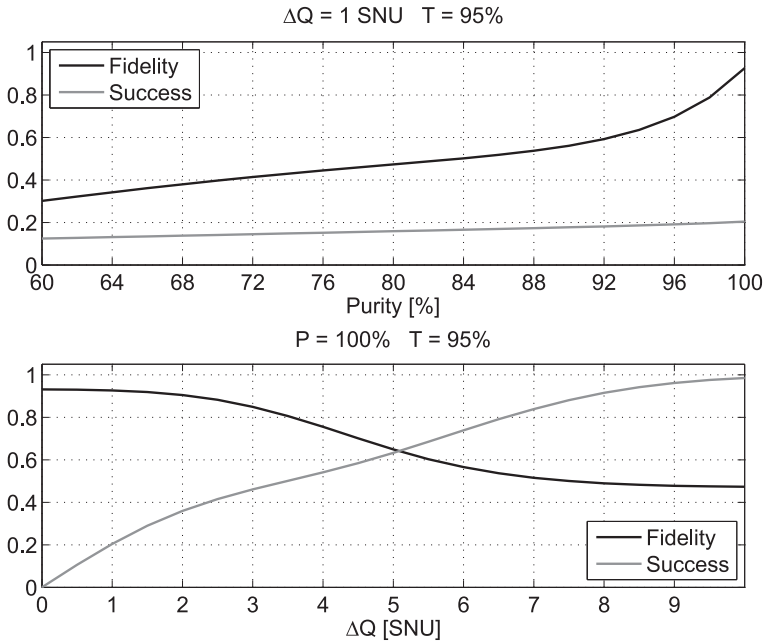

Figure 5.12: Robustness of the PSSV amplification to squeezing impurity (top) and homodyning width (bottom). The fidelity with an even cat of size $\beta = 1.5$ and the success probability of the amplification (assuming offline PSSVs) are plotted in black and gray, respectively. The transmission of the subtraction beam splitter from which the kittens are generated is 95% and the anti-squeezing in p is fixed $\xi_p = -2.9$. (This squeezing is chosen such that the fidelity with $|\kappa_+(\beta = 1.5)\rangle$ is maximized in the case of pure squeezing and $\Delta Q = 1$ SNU—cf. the middle plot of Fig. 5.11.)

5.4 Scalability

As was shown in the previous section, we are bound by a trade-off between amplification and fidelity. I.e., if the output fidelity is to be kept high, one has to work with smaller kittens to begin with, and thus cannot reach higher

amplitudes (cf. Fig. 5.11). A high fidelity can however be achieved with larger states if we cascade the setups into a complete binary tree. We shall discuss the scalability of such a recursive amplification in the case of perfect homodyning ($\Delta Q \to 0$) and pure squeezing ($\epsilon = 1$), both for ideal input cats and for PSSVs inputs.

Let's describe each iteration stage k as the amplification of two identical wave functions $\varphi_k(x_1)$ and $\varphi_k(x_2)$ into a larger state $\varphi_{k+1}(x_1)$ where mode 2 has been post-selected by homodyning. This iteration step is given by

$$\begin{aligned} & \varphi_k(x_1) \cdot \varphi_k(x_2) \\ \to \quad & \{\text{50:50 beam splitting}\} \\ = \quad & \varphi_k\left(\frac{x_1 - x_2}{\sqrt{2}}\right) \cdot \varphi_k\left(\frac{x_1 + x_2}{\sqrt{2}}\right) \\ \to \quad & \{\text{projection on } |x_2 = 0\rangle\langle x_2 = 0|\} \\ = \quad & \varphi_k\left(\frac{x_1}{\sqrt{2}}\right) \cdot \varphi_k\left(\frac{x_1}{\sqrt{2}}\right) \\ \varphi_{k+1}(x_1) \quad \propto \quad & \varphi_k^2\left(\frac{x_1}{\sqrt{2}}\right), \end{aligned} \tag{5.13}$$

where the initial wave function φ_0 is that of the inputs. It can be obtained from the 1-variable analog of (2.96). In the case of input PSSVs, this involves the highly unbalanced mixing two vacua, one of which is squeezed, and—ideally—a one-photon projector $\varphi_{|1\rangle}$. I.e.,

$$\begin{aligned} \varphi_0(x_1) = \lim_{T\to 1} \int_{-\infty}^{\infty} \quad & \varphi_{\hat{S}|0\rangle}\left(\sqrt{T}x_1 - \sqrt{1-T}x_2\right) \\ & \cdot\varphi_{|0\rangle}\left(\sqrt{1-T}x_1 + \sqrt{T}x_2\right) \\ & \cdot\varphi^*_{|1\rangle}(x_2)\,\mathrm{d}x_2. \end{aligned} \tag{5.14}$$

Since we only want to investigate how scaling behaves, however, we shall simplify the PSSV by a squeezed single photon,

$$\lim_{T\to 1} \varphi_0(x) \quad = \quad \langle x|\hat{S}|1\rangle = \frac{\sqrt{2}}{\pi^{1/4}s^{3/2}} x e^{-x^2/2s^2} \tag{5.15}$$

where $s = 10^{\xi/20}$ is the factor by which the quadrature phase space is re-scaled as a consequence of the pure squeezing (i.e., $x \to sx$ and $p \to p/s$).

The wave function of the state at the k^{th} iteration is given in closed-form by

$$\varphi_k(x) = \frac{1}{\mathcal{N}^{(k)}} \varphi_0^{2k}\left(2^{-k/2}x\right), \tag{5.16}$$

where

$$\mathcal{N}^{(k)} = \left[\int_{-\infty}^{\infty} \varphi_0^{2k}\left(2^{-k/2}x\right)\,\mathrm{d}x\right]^{\frac{1}{2}} \tag{5.17}$$

is the normalization factor.

Fig. 5.13 tracks both the amplitude and the fidelity of the outputs as a function of the number of iterations k. As already expected from (5.16), the output amplitude grows as $\sqrt{2}^k$. This does not imply however that iterations could be carried out indefinitely. For the particular choice of initial conditions plotted, $\alpha = 1$ for the cat or 3 dB of squeezing for the PSSV, the fidelity drops below 90% at the fifth iteration. This shortcoming of recursive amplifications is due to the non-unitarity of the amplification in the coherent state basis. Looking back at the idealized case of (5.9), we see that the amplification is not a straightforward mapping of a cat state onto a larger one, but instead introduces an extra vacuum term. This vacuum, which arises from the intrinsic ambiguity of the homodyne projection, is also amplified along with the cat. Even if one does start the first iteration with an ideal cat, any subsequent iteration k will inherit this vacuum component, which in turn will contaminate the following step $k+1$ with additional terms orthogonal to an even cat.

The success rate of iterated amplifications is the main issue facing scalability. As shown in Fig. 5.14, the scheme exhibits a sharp drop in the success probability with the increasing number k of iterations. Another obvious overhead is the number of input states which grows as 2^k.

5.5 Conclusion

We have presented an amplification protocol for cat states that is based on imprecise homodyne measurement. The performance of the scheme was assessed in terms of fidelity and success rate and illustrated by an optimized relation between the target size β and the input size α of the cat states involved. Given that ideal cat states are challenging to produce, we also presented how the amplification behaves with approximations to cat states, namely photon-subtracted squeezed vacuum. Here again, we determined the optimal relation between the input squeezing and the effective size of the output. The purity of squeezing at the input was determined to be crucial in achieving a high fidelity at the output. The amplification was however relatively robust to imprecise homodyne thresholding, thereby allowing an increase in success probability.

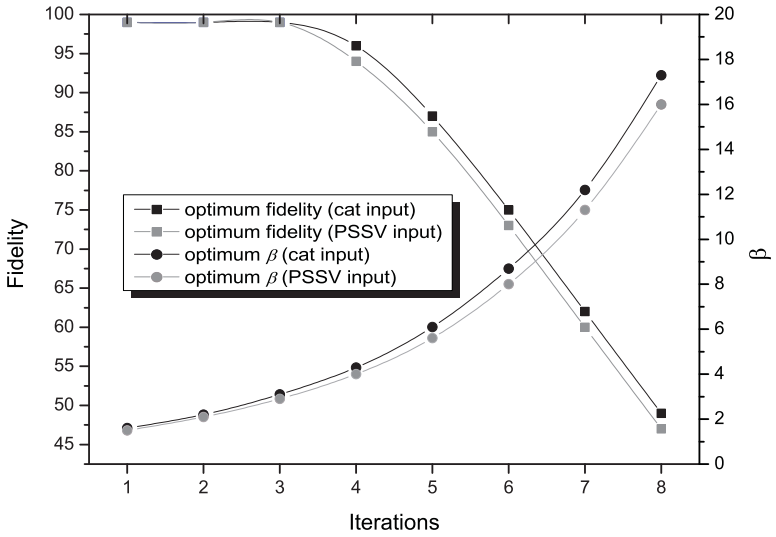

Figure 5.13: Maximum fidelity (squares) and corresponding effective size β (disks) of the output as a function of the number of iterations. The inputs to the first iteration are an ideal odd cat of size $\alpha = 1$ (black) or a PSSV squeezed by 3 dB (gray).

The recursive application of the amplification protocol is then simulated in the idealized case of exact homodyning and pure squeezing. Although the amplification factor does grow as as $\sqrt{2}^k$ with the number k of recursions, the output fidelity eventually degrades due to the non-unitarity of the amplification. One is therefore constrained to a finite number of recursions where the state is amplified while at the same time retaining a high fidelity.

We saw in §5.3 that target cat sizes $\beta = 1.5$ can be reached with fidelities up to 93% if one uses PSSVs obtained from a 5% tapped-off squeezed vacuum. (If one assumes ideally squeezed single photons, that fidelity can even increase to 98%, cf. the first iteration in Fig. 5.13. For higher iterations of the amplification, amplitudes of $\beta \approx 3$ can be obtained while maintaining fidelity around 98%.) Although such approximate states may not permit fault-tolerant quantum computation, they nonetheless allow for proof-of-principle experiments that require effective cat sizes larger than those of basic PSSVs. For instance, our amplification protocol can find uses in teleportation [110] or some demonstrations of quantum gates [111, 13]. The question of whether the amplified states can be harnessed for any particular use in quantum information will require a feasibility study of its own that

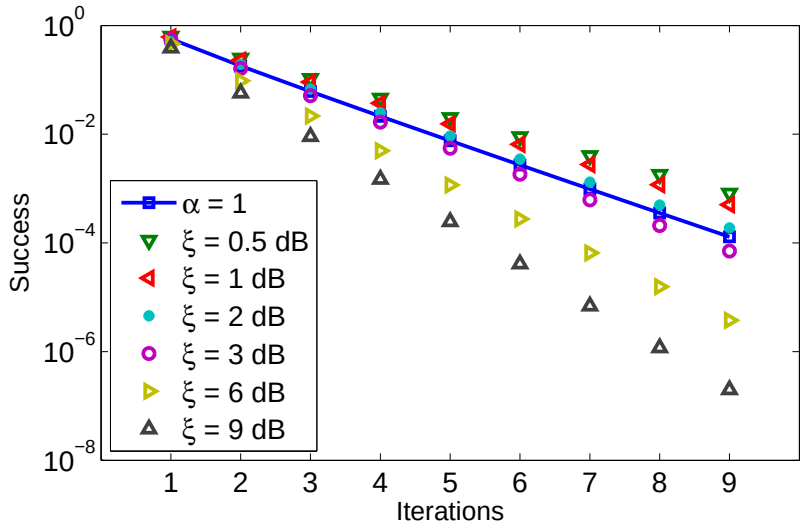

Figure 5.14: Success probability of iterated amplifications for an input cat state $|\kappa_-(\alpha = 1)\rangle$ as well as for various input PSSVs with squeezing $\xi \in \{0.5, 1, 2, 3, 6, 9\}$ dB.

pays particular attention to the tradeoff between target sizes and fidelities.

Let's conclude with a final note on the practical challenges to our protocol. In addition to the issues proper to PSSV preparation (and already discussed in [94, 14, 95, 98, 99]), the key challenge facing the amplification protocol is phase stability. This arises because the pairs of interfering PSSVs need to be synchronous, thereby leading to very small success rates. This is to be factored on top of the already small success rate of an otherwise ideal post-selection (Fig. 5.14). Small success rates are compensated for by running the experiment over a larger batch of input states. However, this in turns requires that the relative phases—of the two interfering PSSVs and of the local oscillator—be kept stable for protracted periods using a particularly reliable locking system.

Chapter 6

Experimental trials

This chapter serves three purposes. The first is to illustrate some experimental devices that make up the theoretical toolbox presented in the Chapter 2. The second is to describe the setup with which photon-subtracted squeezed vacuum is prepared. Finally, the last section will serve as a repository for the many bedeviling setbacks encountered in the laboratory in the course of this PhD project.

One of the initial goals was to produce approximate coherent state superpositions via photon subtraction of the squeezed vacuum. These approximate cat states were then supposed to be used as resources for more elaborate schemes such as entanglement distillation [112], noise-free attenuation, and cat state amplification [113]. Small cat state superposition had already been obtained from our setup and successfully harnessed by Tipsmark *et al.* in a proof-of-principle implementation of a Hadamard gate [13]. However, the resource states used were exhibiting unsatisfactory purities for more demanding applications. This required changing the down conversion crystal and consequently re-adjusting the entire optical configuration from which squeezing was to obtained. This has however lead to a dead end where not only the squeezing, but also the classical de-amplification could hardly be observed for a reason—or multitude of reasons—that have yet to be tracked down. To further exacerbate matters, the pulsed laser driving the entire experiment has been prone to severe noise contamination from the cavity dumper. These issues will be highlighted at the end of this chapter.

Optical frequency	829.7 nm
Spread in optical frequency	0.2 nm
Pulse duration	4.6 ps
Pulse repetition rate	816 kHz
Average pulse energy	83 nJ
Cavity frequency	82 MHz

Table 6.1: Specifications of the pulsed laser.

6.1 The pulsed laser

The laser light used in our laboratory is delivered as a train of optical pulses [114]. The advantage of the pulsed operation is that the regular bursts of light are of higher intensity than if their energy were spread as a continuous flow. This higher intensity can fully arouse the non-linearity of the down-conversion crystal without having to place it in a multi-pass configuration. Additionally, the narrow time windows that the pulses represent allow for a better timing of the detection events. As we shall see, the downside is that the finite extent of the pulse inherently includes frequency components foreign to the sharp optical frequency of the continuous-wave case. The relatively high intensities can furthermore lead to beam profile distortions in the crystal.

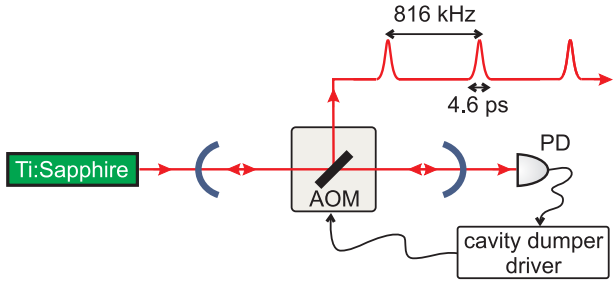

Figure 6.1: Generation of 4.6 ps pulses from a mode-locked laser. A Ti:Sapphire source of 829.7 nm is confined to a cavity, represented here as the two curved mirrors. An RF-driven acousto-optical modulator lets the pulses build up in the cavity until the 100^{th} iteration, at which point it diverts the light out for use. A photodiode (PD) ensures that this cavity dumping is synchronized with the 82 MHz frequency by feeding back to the AOM driver. Given that the round-trip frequency in the cavity is 82 MHz, we end up with a repetition rate of the pulses of 816 kHz.

The laser system used is assembled as part of Time-Bandwidth's TIGER series[1] and consists of a laser head, a control unit, a power supply from LaserQuantum[2], a cavity dumper driver from NEOS[3], and a chiller from Ferrotec[4]. Some key figures for the laser light are summarized in Tab. 6.1 and the main stages of the pulse generation are sketched in Fig. 6.1. The lasing source at 829.7 nm is a titanium-doped sapphire (Ti:Sapphire) crystal which is diode-pumped via frequency doubling of a neodymium-doped yttrium orthovanadate (Nd:YVO_4) crystal. The generated pulses then bounce in a cavity at a frequency 82 MHz. Such a repetition rate is too high to be reliably resolved by the detection electronics [115]. By incorporating an acousto-optical modulator (AOM), also known as Bragg cell, in the cavity, the repetition rate can be divided by 100 to about 816 kHz. This process is known as cavity dumping and has the advantage of conserving all the light in the cavity as opposed to, say, throwing out 99 pulses only to keep the 100^{th} [116].

Fourier-transform limit. The pulses generated by the laser were found to be Fourier-transform limitedness by measuring their duration and bandwidth with an auto-correlator. In other words, they satisfied the criterion for Fourier-transform limited Gaussian pulses, namely

$$\Delta\tau_{\text{FWHM}}\Delta\nu_{\text{FWHM}} = 2\frac{\ln 2}{\pi}. \tag{6.1}$$

In addition to being chirp-free [117], Fourier-limited pulses have the advantage that their scattering into several different modes in the temporal domain is minimized, thereby preserving the temporal purity of the state in any single mode.

6.2 Parametric processes

The electromagnetic wave equation in a homogeneous and isotropic medium is given by

$$\nabla^2\boldsymbol{E} - \frac{1}{c_0^2}\frac{\partial^2\boldsymbol{E}}{\partial t^2} = \mu_0\frac{\partial^2\boldsymbol{P}}{\partial t^2}, \tag{6.2}$$

where $\boldsymbol{P}$ is the polarization density, and c_0 and μ_0 are the speed of light and the permeability in vacuum, respectively.

[1] http://www.time-bandwidth.com
[2] http://www.laserquantum.com
[3] http://www.neostech.com
[4] http://www.ferrotec.com

Most materials only exhibit a linear relationship between the dielectric medium and the electric field. This is however only a weak-field approximation and certain materials dubbed nonlinear actually exhibit a higher order dependence of the polarization on the electric field

$$P = \epsilon_0 \left(\chi^{(1)} E + \chi^{(2)} E^2 + \chi^{(3)} E^3 + \dots \right). \tag{6.3}$$

Let's assume the driving electric field $\boldsymbol{E}$ is made up of a superposition of two components of frequencies ω_1 and ω_2 of amplitude E_1 and E_2, respectively. A quadratic response of the polarization density to such a field will then contribute the following term to (6.2):

$$\begin{aligned} P^{(2)} &= \epsilon_\circ \chi^{(2)} E^2 \\ &= \epsilon_\circ \chi^{(2)} \left(E_1 \cos \omega_1 t + E_2 \cos \omega_2 t \right)^2 \\ &= \frac{\epsilon_\circ \chi^{(2)}}{2} \Big(E_1^2 + E_2^2 + E_1^2 \cos\left(2\omega_1 t\right) + E_2^2 \cos\left(2\omega_2 t\right) \\ &\quad + 2E_1 E_2 \left[\cos\left(\omega_1 - \omega_2\right)t + \cos\left(\omega_1 + \omega_2\right)t \right] \Big). \end{aligned} \tag{6.4}$$

It can be seen that the quadratic response of the nonlinear medium produces electric fields of frequencies other than those making up the incident light. The last two terms of (6.4) show the components of the electric field where the initial frequencies ω_1 and ω_2 are doubled, subtracted, and added. Which one of these processes takes place depends on the momentum (i.e., phase) and energy (i.e., frequency) of the incoming fields $\boldsymbol{E}_1$ and $\boldsymbol{E}_2$.

6.2.1 Phase-matching

A condition for parametric processes as in (6.4) to take place is that the generated waves at the frequencies $2\omega_{1,2}$ or $|\omega_1 - \omega_2|$ maintain a consistent phase relation with their fundamental fields $\boldsymbol{E}_1$ and $\boldsymbol{E}_2$ throughout the nonlinear material. Such a regime, known as phase-matching, depends on the incidence of the input fields onto the crystal as well as the orientation of the crystal's axes as specified by the second-order nonlinear susceptibility tensor $\chi^{(2)}_{xyz}$. The relevance of phase-matching comes from the fact that the refractive index depends on the frequency of the light. The generated waves thus invariably propagate ahead or behind the driving waves to ultimately end up out of phase. This can be remedied by ensuring that the overall wave vector is conserved throughout the crystal between the input and output waves: $\boldsymbol{k}_{\text{in}} = \boldsymbol{k}_{\text{out}}$. For example, in the case of frequency doubling where two waves of frequency $\omega = \omega_1 = \omega_2$ combine to form a wave of frequency 2ω,

we get $k(2\omega) = 2k(\omega)$. Given the definition $k = n\omega/c$, we therefore get that phase-matching is achieved provided the index of refraction through which the 2ω output wave propagates equals that through which the driving fields at ω travel. Such a configuration can be realized in birefringent crystals. An alternative to birefringence is the periodic poling of the crystal along the transversal direction of propagation whereby the nonlinear susceptibility tensor flips sign at regular intervals. This periodic reversal of the nonlinear coefficient cancels out any phase mismatch acquired over any one period of the poling. It is this latter method which we used in our laboratory with a periodically-poled potassium-titanyl-phosphate (PPKTP) crystal. As opposed to the birefringence method where the input and output fields have to have orthogonal polarizations to perceive different indices of refraction, periodic poling can make use of a single polarization for all fields.

It should be noted that vector mismatch between the fields involved, unless corrected by periodic poling or birefringence, accumulates along the nonlinear crystal. I.e., the efficiency of the parametric process is increasingly affected the more the fields propagate—it is only in the case of perfect phase-matching that the nonlinearity increases indefinitely with the interaction length. One has therefore to negotiate a tradeoff between the length of the crystal and the cumulative effect of phase mismatch [118].

6.2.2 Mode-matching

In order to optimize a nonlinear interaction, the geometry of the beams involved should be chosen such that the fundamental beam transfers as much power as possible to the converted beams. The condition to achieve this is called mode-matching. It is essentially similar to a visibility optimization in interference setups where we now want to ensure that the spatial mode to be converted is in "full view" of the fundamental (or pump) mode. Most often, the plane wave approximation for the fields does not hold and one has to consider Gaussian profiles for the beams. Boyd and Kleinman [119] have theoretically demonstrated that in order to achieve the highest conversion efficiency of up-conversion, the confocal parameter z_0 of the fundamental beam should relate to the length of the nonlinear crystal L_c as

$$\frac{L_c}{2z_0} = 2.84. \tag{6.5}$$

The above optimization condition is equally valid in the case of spontaneous parametric down-conversion since it can be considered in many regards as the reverse process of down-conversion and therefore would be optimized

by the same optical geometry. In principle, this means that the highest classical gain of down-conversion is expected when the pump beam has the same confocal parameter as some probing seed [120] from which we can easily measure classical amplification. As quantum optics experiments have become common place, it turned out that the Boyd-Kleinman prescription (6.5) leads to too high focusings of the pump [121, 122]. Although a narrow focusing should in theory maximize the nonlinear response of the crystal, it also leads to thermal effects and other power-related distortions that affect both the profile of the beam and the purity of the squeezing. One could of course reduce the focusing, i.e. decrease the confocal length z_0, while at the same time increasing the length of the crystal L_c in (6.5), but the downside of a lengthened crystal is that dispersion effects become more prominent. In fact, the tradeoff between crystal length and focusing configuration has proven to be the most challenging objective to attain. §6.5 elaborates further on the many side effects of working with focused beams and presents some of the many (inconclusive) data gathered in the process of optimizing the down-conversion source.

Gaussian beam propagation. Beam profiles can be measured with a beam profiler placed at different longitudinal positions z from an arbitrary reference point down the optical path. The data points, consisting of beam radii—i.e. radial distances where the intensity reaches $1/e^2$ of its maximum—, should then fit a nonlinear model given by

$$W = W_0\sqrt{1 + \frac{\lambda^2(z-\delta z)^2}{W_0^4\pi^2}}, \tag{6.6}$$

where W_0 is the radius of the beam at the waist [123]. The wavelength of the light is λ, and δz is the position of the waist from the reference point. The outcomes from the fit are the position of the waist δz as well as its radius W_0. The latter in turn yields the Rayleigh length

$$z_0 = \frac{W_0^2\pi}{\lambda}. \tag{6.7}$$

If one wants to place the waist of a beam at the centre of the nonlinear crystal, a series of lenses can be assembled into a transformation matrix $\boldsymbol{M}$ to recreate a new waist at the desired position according to (6.6). This is sketched in Fig. 6.2.

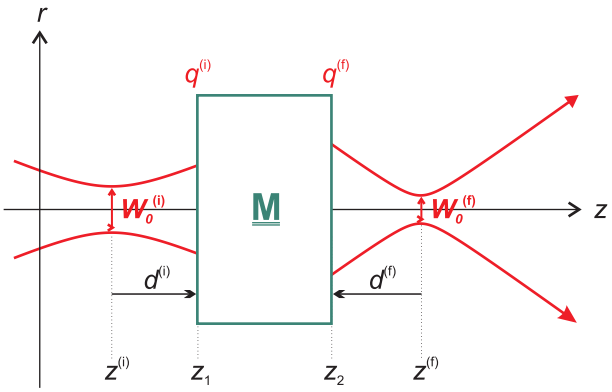

Figure 6.2: Reshaping of a Gaussian beam. The initial beam has a waste $W_0^{(i)}$ centered at position $z^{(i)}$ down the optical axis. If one wants a new waist $W_0^{(f)}$ at position z^f where, say, the nonlinear crystal is to be placed, then one needs to find a combination of lenses that amount to the transformation matrix $\boldsymbol{M}$ according to the rules of the ABCD formalism [123]. The positions z_1 and z_2 are only used as fiducials to mark where the first and last transformation lenses are to be placed.

6.3 Detection

We have already seen in Chapter 2 how to model the DV and CV measurements of photon counting and homodyning, respectively. This section will briefly introduce some aspects of detection that are specific to the experimental context.

6.3.1 Photon counters

Photon detection in our setup is limited to a binary outcome: We used avalanche photodiodes (APDs) which only click if at least one photon impinges on them.[5] The dark count rate is around 20 false clicks per second and the quantum efficiency is about 60% at 830 nm.

6.3.2 Homodyne detectors

The operation of homodyne detectors is thoroughly covered in the literature [3, 124, 115]. Let's nonethless re-emphasize the importance of balancing the detector when it comes to acquiring quadrature data. The proper operation

[5] Perkin-Elmer SPCM-AQR-16-FC [http://www.perkinelmer.com/]

of a homodyne detector requires that the signals recorded at the two photodiodes balance out completely and that the shot noise power[6] be proportional to the power of the local oscillator. When proportionality is achieved, the homodyne detector is said to be shot-noise limited. Not only does the overall power need to balance out, but so should every of its frequency components balance out individually. If this latter condition is not satisfied, some classical noise peaks will emerge from the shot-noise background in the frequency spectrum, even if power cancels out in time domain.[7] The quality of balancing of a homodyne detector can be characterized by graphs as those sketched qualitatively in Fig. 6.3

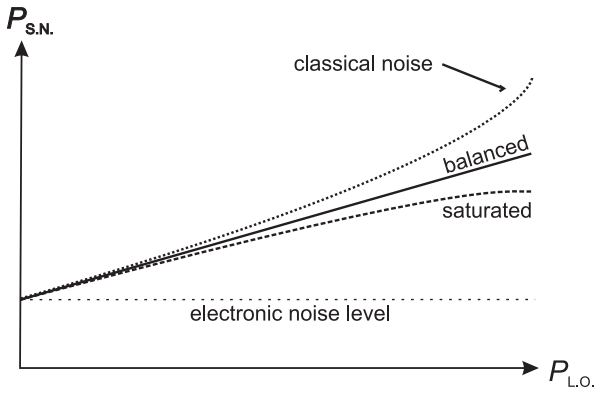

Figure 6.3: Dependence of the shot noise power on the power of the local oscillator in dimensionless units. A homodyne detector is balanced if, at any given frequency, the shot noise power $P_{\mathrm{S.N.}}$ is linear with the power of the local oscillator $P_{\mathrm{L.O.}}$. Any divergence from this linearity is indicative of either a saturation of the detector's electronics or of classical noise filtering through the signal. Note that the shot noise power lies on top of a background of electronic noise that is always present regardless of the incidence of a local oscillator.

[6]Shot noise power is quantified as the variance of the difference in current between the two photodiodes.

[7]The downside of time-domain homodyning is that it sums over all frequency components which, because of pulsed operation, cannot in any trivial way be recovered from the time trace via Fourier analysis.

6.4 State engineering

The principal state we were interested in generating in the laboratory is the photon-subtracted squeezed vacuum (PSSV) for its high fidelity with small coherent state superpositions. In this section we shall describe the main stages that come into its engineering. The most salient challenge we faced—that of producing pure squeezed vacuum—will be highlighted.

6.4.1 Experimental setup

The idea of subtracting a photon from the vacuum dates back to the work of Dakna *et al.* [92] and has been subsequently refined and simplified [91] to be first implemented in 2006 in both the continuous wave [95] and pulsed regimes [94]. The idea consists of sending a squeezed vacuum through a highly-transmissive beam splitter. The reflected arm is monitored by a photon detector, typically an avalanche photodiode (APD), which—upon clicking—heralds a PSSV. This output state then can be characterized by homodyne tomography using a local oscillator (L.O.) originating from the same laser as that of the pump and the seed.[8] The experimental setup is sketched in Fig. 6.4.

[8] This assumes that no phase diffusion occurs between pump, seed, and L.O. This point will be treated in further detail below.

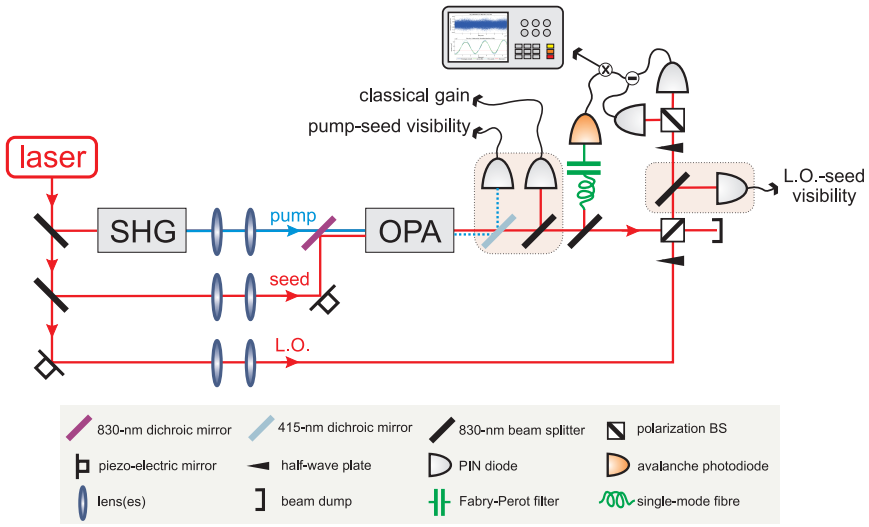

Figure 6.4: Experimental setup for the generation of PSSV. The laser beam emerges in the vertical polarization and is split into three arms: The first is for down-conversion via second harmonic generation; the second is for the seed beam with which classical gain is visualized; and the third is the local oscillator for homodyning. The pump is obtained by second harmonic generation in a first crystal (SHG) and then focused onto an optical parametric amplifier (OPA). Sets of lenses, represented here by simple pairs, are placed on all three arms so as to tune the profiles of the beams. If one is only interested in measuring squeezing, the down-converted signal is sent directly for time-domain or frequency-domain tomography via a homodyne detector. If one wants instead to produce PSSVs, then part of the signal is tapped-off onto an APD via a single-mode fibre (SMF) and Fabry-Perot filter (FP) for spatial and frequency filtering, respectively. The beige areas represent parts of the setup that are used for monitoring purposes only and are removed when actual state production takes place. Two of the quantities monitored are the "blue-blue" visibility between the up-converted seed and the pump, and the classical gain of the pump. They are both modulated by the piezoelectric mirror at the seed arm. A third monitoring PIN diode is placed after the polarization mixing of the seed and local oscillator and traces the visibility between them.

6.4.2 Pre-measurement checklist

As touched upon in §6.2.2, the above assumes that the heralded, heralding, and measured states all belong to the same mode which, to boot, should initially be populated by a pure squeezed vacuum. Failing this requirement of mode-matching, the purity of the heralded state will be severely affected. One should therefore routinely go through the following pre-measurement checklist:

1. **Seed and pump visibility**: Recall that the local oscillator defines the mode that is probed by homodyne detection. The pump, from which the down-converted signal originates, should therefore match that mode. I.e., for being the ultimate source of light, the pump (415 nm) should populate a spatial mode that needs to be "visible" to the local oscillator. To this end, a seed beam at half the optical frequency of the pump (i.e., 830 nm) is sent through the parametric amplifier for up-conversion. By maximizing the visibility[9] between the two blue beams—that merely transmitted from the pump and that resulting from the up-conversion of the seed—we can have a benchmark of how well the local oscillator will "see" any signal from the down-converted pump provided the local oscillator and the seed are in turned aligned with high visibility.

2. **Seed and local oscillator visibility**: Although we are ultimately only interested in probing the squeezing with the local oscillator, the alignment of the seed is still crucial in insuring, via step 1 above, that the pump and the local oscillator pertain to the same spatial mode. The assumption being made here is that the down converted signal populates the same mode as that of the pump. A typical value for the visibility between the seed and the local oscillator is typically between 92% and 95%.

3. **Frequency mode-matching**: The points above dealt with *spatial* mode-matching where the seed served as an intermediary between the pump and the local oscillator. However, the modes of the squeezed vacuum and the local oscillator should also be matched in *frequency*. There exists to this effect an entire theoretical body of work that deals with how the nonlinear crystal can be engineered and the pump configured such that the idler and signal beams are de-correlated in frequency. [125, 126]. A de-correlation in frequency ensures that the

[9] This blue-blue interference was measured to be 95% [2012-09-26].

heralding process at the APD does not induce a mixing of the frequency modes in the reconstructed heralded state. A simpler alternative is to simply enforce that both the heralded and heralding modes are the same by placing a Fabry-Perot filter in the heralding arm. By doing so, the filter can be adjusted so as to only transmit light of the same frequency as that of the local oscillator, thereby post-selecting the squeezing which is degenerate at the selected in frequency and hence *de facto* de-correlated.[10]

4. **Homodyne balancing**: The points above address spatial and frequency mode-matching. Another type of mode-matching, which could be regarded as *temporal*, is to ensure that the homodyne detector is balanced both in the time and frequency domain and that the signal is not infiltrated with classical noise. This has turned out to be a major challenge as the laser we are using produces an unshakable noise at 70 kHz which is passed on as parasitic side bands around the repetition rate of the pulses. Although the noise can be marginally alleviated by tuning the settings of the cavity dumper driver, the best one could do is simply to adjust the incidence on the arms of the homodyne detector such that its voltage is balanced both in time (via the oscilloscope) and in frequency (via the electronic frequency analyzer). In particular, the distribution of the homodyne signal with shot noise is checked for Gaussianity as any non-Gaussian distribution is indicative of poor balancing.

5. **Classical gain**: Finally, in addition to mode-matching, there remains the issue of phase-matching on which the efficiency of the down-conversion process depends. One needs not to look directly at the squeezing for this but simply at the classical gain, or factor of amplification and de-amplification of the seed in the presence of a pump. The larger the classical gain the better is the quantum process—i.e., squeezing—expected to be. This is done by adjusting the relative positioning of the seed with the pump. Note that there may be a potential contradiction between the optimization of classical gain and that of pump-seed visibility from point 1 above as both procedures may have different sweet spots.

[10]The central wavelength of the Fabry-Perot [FFP-TF-0830-022G1400 from Omicron Optics] has a tendency to drift and needs to be regularly re-centred at the right frequency. An electronic lock programmed in Arduino has been developed for this purpose by Jonas Schou Neergaard-Nielsen.

6.4.3 Measurement

We shall now describe some aspects of measuring the heralded states but stop short of giving a description of the tomography process as it is already discussed in other sources [127, 115]. We shall instead focus on how quadrature data are acquired and squeezing determined.

Every voltage recorded by the homodyne detector can be related to a quadrature value. Because we are working in pulsed regime, the convention we adopted is that the voltage of every pulse be integrated over a square time-window that is synchronized by the cavity dumper to correspond to the arrival of a pulse. The time-domain trace that one obtains by assembling the integrated pulses is of no use unless mapped onto a quadrature vs. local oscillator phase plot. Since we did not incorporate any phase locking of the beams in our setup, the correspondence between the time axis and the phase of the L.O. had to be inferred from the squeezed data itself: If we take variance[11] maxima to correspond to a given phase θ of the L.O. then the minima will correspond to $\theta + \pi$. The L.O. phase at any intermediate point can then be determined by phase fitting methods, of which there exists several variants such as (a) straightforward cosine fitting—which assume no phase fluctuations—, (b) smoothing algorithms that average between neighboring variance points, or (c) the more intelligent Savitzky-Golay smoothing filter which does not affect the amplitude of the extrema [128]. An example of homodyne trace and its various fits is reproduced in Fig. 6.5.

Aside: Correcting squeezing for losses

The squeezed states measured in an experimental setting suffer de-coherence as they propagate from the down-conversion crystal to the homodyne detector. To assess the actual performance of the down converter it may be informative to reverse the losses incurred on the squeezed signal through propagation or quantum inefficiencies of detection. These losses can be modeled by a beam splitter of transmission η which will have the effect of contaminating the an input quadrature $\hat{q}_{\text{in}}$ with a vacuum component $\hat{q}_{\text{vac}}$

$$\hat{q}_{\text{out}} = \sqrt{\eta}\hat{q}_{\text{in}} + \sqrt{1-\eta}\hat{q}_{\text{vac}}. \tag{6.8}$$

[11] Given the pulsed nature of the measurement, variance is determined by grouping sets of data into bins. One has then to choose a tradeoff between the resolution of the variance (for wide bins) and the resolution of the phase (for narrow bins).

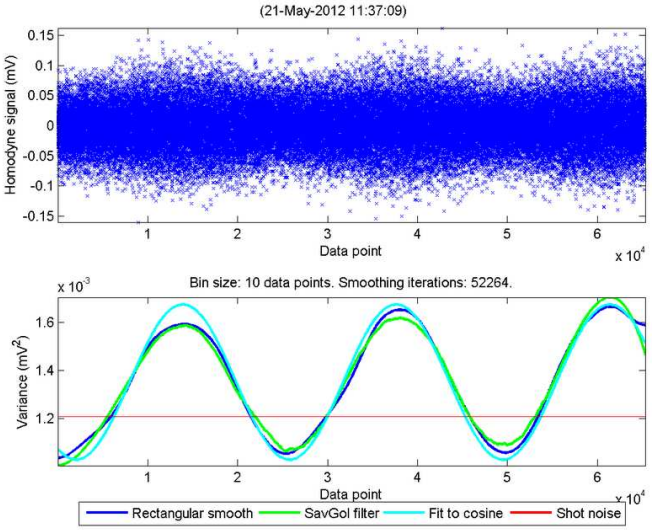

Figure 6.5: *Top*: Raw trace of integrated homodyne data consisting of a sequence of about 64000 integrated voltage points. *Bottom*: By bunching ten contiguous data points into bins, the variance can be estimated. A fit can then be performed by iteratively averaging over neighbouring points (blue), applying the Savitzky-Golay filter (green), or simply fitting to a cosine (cyan). The flat red line is obtained from the variance of shot noise and serves as the reference benchmark. It can be noticed that the anti-squeezing is systematically higher than squeezing proper. This is indicative of a non-ideal purity of squeezing.

The variance of the output can be shown to be

$$\begin{aligned} \mathcal{V}_{\rm out} &= \langle \hat{q}_{\rm out}^2 \rangle - \langle \hat{q}_{\rm out} \rangle^2 \\ &= \{\text{Eq. (6.8) and } \langle \hat{q}_{\rm vac} \rangle = 0\} \\ &= \eta \mathcal{V}_{\rm in} + (1-\eta)\mathcal{V}_{\rm vac} \end{aligned} \tag{6.9}$$

Using (2.54), we can see that the measured squeezing $\xi_{\rm out}$ really corresponds to a squeezing $\xi_{\rm in}$ coming out of the down converter according to

$$\xi_{\rm in} = 10 \log_{10} \left((10^{\xi_{\rm out}/10} - 1)/\eta + 1 \right). \tag{6.10}$$

Here, η encapsulates the combined effects of transmission and detection efficiency up to the measurement of $\xi_{\rm out}$. It can typically be broken down as follows

$$\eta = \eta_{\rm t}\eta_{\rm v}\eta_{\rm d}\eta_{\rm e}, \tag{6.11}$$

The various efficiencies are as follows. η_t is the transmission efficiency through the optical circuit. η_v is the square of the visibility of the measured signal and basically quantifies how well we are probing the right signal mode. η_d is the quantum efficiency of the detector. η_e is the efficiency with which the detector distinguishes the truly quantum noise from the parasitic electronic noise [129]. In this sense, quantum noise, also known as shot noise, is really the signal we want to measure. The signal to noise ratio (SNR), which is the ratio of variances of electronic to shot noise, therefore enters this electronic efficiency as $\eta_e = 1 - 10^{-\mathrm{SNR}/10}$. Note that the SNR is expressed in decibels. In our laboratory, approximate values for all these components are $\eta_t = 86\%$, $\eta_v = 91\%$, $\eta_d = 93\%$, and $\eta_e = 98\%$ (for an SNR of about 17 dB) [126].

6.5 Nuisances and obstacles

In the course of 2012, the reliability of the setup as a squeezing source decreased markedly to a point where no de-amplification at all could be observed. Although no definite diagnostic as to why that is could be performed by the time the experiment was terminated, two potential causes stand out. The first is that the laser source had a history of carrying a parasitic frequency around 68 kHz [126]. This implied that the signals detected at the homodyne detector could not be satisfactorily balanced out at all frequencies: The 68 kHz noise, which most likely originates from faulty circuitry in the cavity dumper driver, infiltrated the optical signal as side bands around the 815 kHz repetition rate. The second cause can be attributed to a very poor mode- and phase-matching configuration for the down converter.

Some calculations in [126] indicate that shorter crystals are more desirable if one wants to attain high purities of squeezing. As will be explained below, this is motivated by the fact that a shorter interaction length, though offering a lesser conversion efficiency, also minimizes dispersion and beam distortion effects. In view of this, we replaced the 3 mm crystal we initially had with a 1.5-mm crystal. This however implied searching from scratch—and with little guidance from theory—for a new phase-matching configuration. Such a configuration was never to be obtained as we were stuck with a highly impure conversion process that exhibited only marginal, if not completely absent, de-amplification.

6.5.1 Laser noise

Let's illustrate the noise of the laser with some measurements. Fig. 6.6 shows the radio frequency (RF) signal that comes out of the cavity dumper driver to control the AOM. The higher peaks at 820 kHz are normal, since they simply reflect the designated repetition rate. They are however surrounded by conspicuous side bands at 68 kHz which, after consultation with both the manufacturer and our in-house electronics engineer, has proved to impossible to suppress.

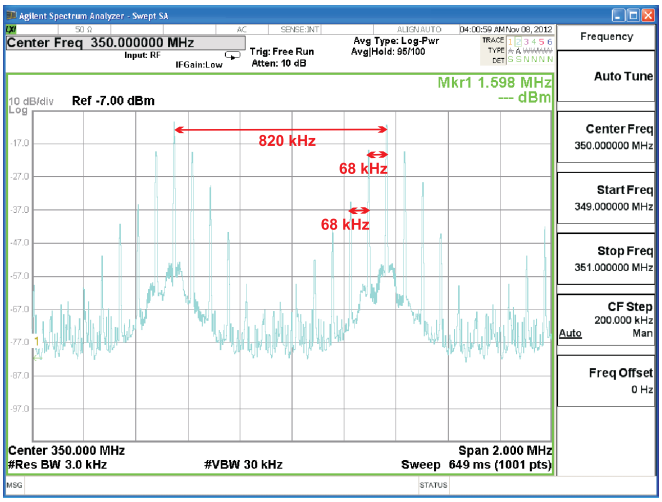

Figure 6.6: Frequency spectrum of the RF signal delivered by the cavity dumper driver to the AOM. The 820 kHz peaks corresponding to the repetition rate are flanked by 68 kHz side bands.

The problem with the noise is that it is passed on to the optical signal and once again detected as side bands to the repetition rate at the homodyne detector. Fig. 6.7 displays the frequency spectrum at the homodyne detector both for the case of complete unbalancing (blue) and maximal balancing (yellow). Note that the side bands could not be totally removed.

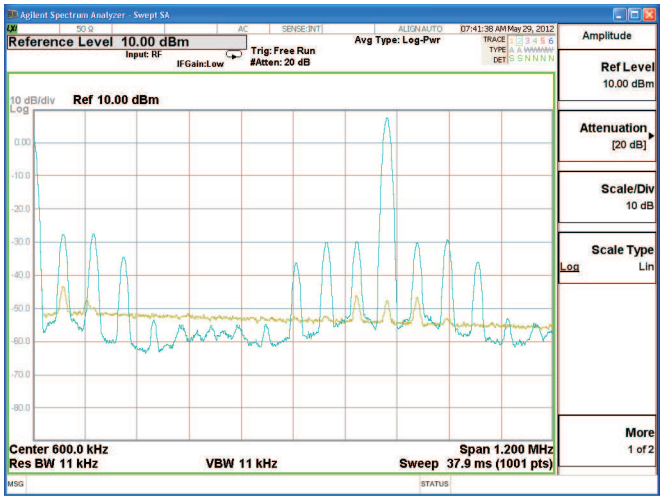

Figure 6.7: Frequency spectrum of the homodyne voltage for (nearly) balanced (yellow) and completely unbalanced (blue) power in the homodyne arms. Note that ideal balancing could never be achieved.

In addition to the noise, the laser also exhibited power fluctuations. Given that any homodyne measurement for, say, squeezing measurements, consisted of batches of 64000 consecutive pulses, any fluctuations that occur during the capture will corrupt the shot noise reference. These fluctuations are displayed in Fig. 6.8.

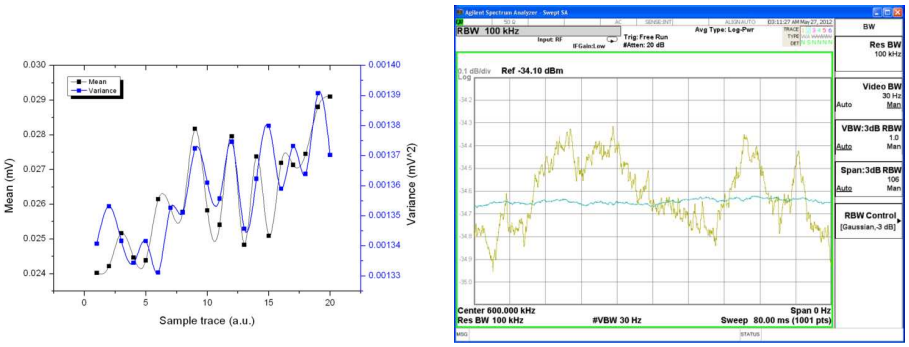

Figure 6.8: Fluctuations of the shot noise power as detected by the homodyne detector with 10 μW local oscillator. *Left*: Time-domain fluctuations of the mean homodyne signal and its variance for 20 consecutive shot noise traces of about 64000 pulses each. There is a delay of the order of 10 s between each capture. *Right*: Frequency-domain fluctuations of the 600-kHz component of shot noise over 80 ms (yellow) about its mean value (blue).

6.5.2 Phase- and mode-matching

As discussed above, the amplitude and purity of squeezing depends on whether the light-matter interaction within the crystal is optimized for the conversion process. To achieve phase- and mode-matching, several factors can be tuned such as the temperature and length of the crystal as well as the focusing and incidence of the fundamental beams [130]. Two theoretical prescriptions exist in this regard. The first one is equation (6.5) by Boyd and Kleinman [119] which, for short crystals such as ours, implies a tight focusing of the pump. However, the narrower the focusing of the pump, the more prone does the signal become to distortions and therefore to undesirable mode-mixing [131, 121, 132, 126]. The second prescription, by La Porta and Slusher [121], relates to the ratio of waists between the pump and the seed so as to obtain the best alignment of wave fronts between the fundamental and converted beams[12]. In particular, it states that the seed beam should be at least $\sqrt{2}$ larger than the pump at the waist as that will equate their confocal lengths z_0:

$$z_0^{(\text{seed})} = z_0^{(\text{pump})} \Leftrightarrow W_0^{(\text{seed})} = \sqrt{2} W_0^{(\text{pump})}, \tag{6.12}$$

[12]Once again, the seed is supposed to act as the classical "impersonation" of the modes that the down converted signal would take.

where W_0 are the waist diameters. (Here, the $\sqrt{2}$ factor comes from the fact that frequency is halved by the down-conversion process.)

In contradiction to (6.12), experimental evidence in other pulsed, single-pass configurations reports instead that it is the *pump* that should be $\sqrt{2}$ larger than the seed. This implies that for any given choice of seed, the focusing of the pump should be weakened so as to resemble more closely that of a plane wave all throughout the crystal [133, 98]. After several attempts to modify the relative size of the pump and seed,[13] only marginal de-amplification could be observed whereas squeezing was simply nonexistent. This dead-end state of affairs was most likely worsened by the persistent noise contamination from the laser itself. Fig. 6.9 shows a very noisy and extremely impure classical gain curve with essentially no de-amplification.

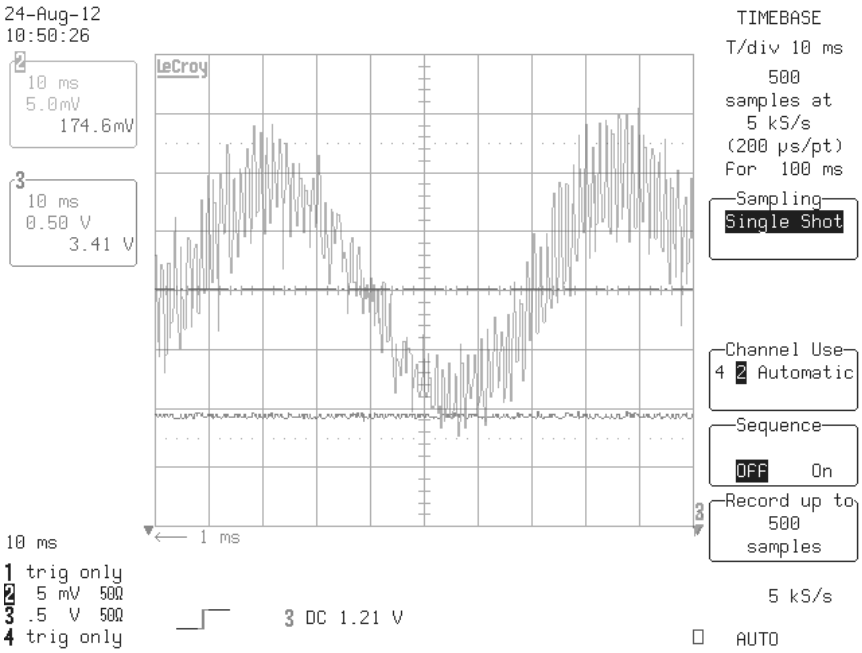

Figure 6.9: Time trace of the classical gain as a voltage detected by a photo diode in the course of 1 s. The bottom line represents the average voltage delivered by the seed. The sinusoidal line is the modulated seed with a pump of about 5 mW.

The search for phase matching also lead us to look for an optimal temper-

[13] Note that the maximum blue-blue visibility that is required by the pre-measurement checklist above (point 1) does not coincide with the maximum classical gain (point 3).

ature of the down conversion crystal. Here again, only the classical amplification was affected whereas de-amplification remained very small throughout (Fig. 6.10).

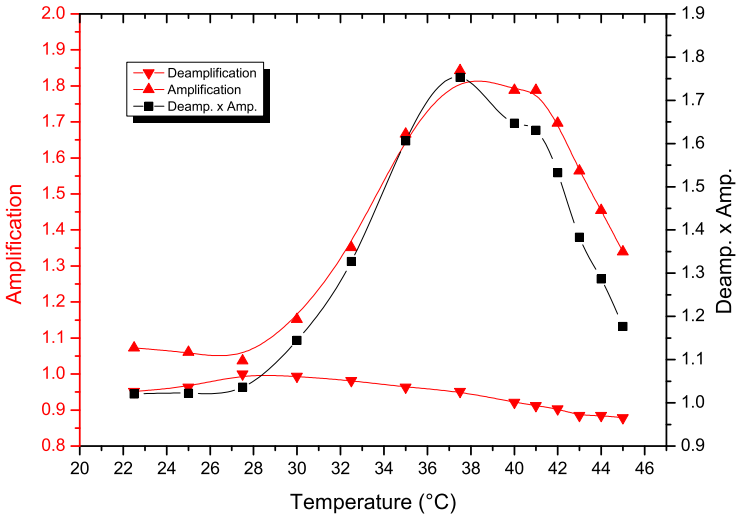

Figure 6.10: Classical amplification (△) and de-amplification(▽) as a function of the crystal temperature. The product of amplification and de-amplification (□) indicates the purity of classical gain whereby unit purity corresponds to a product of 1.

Similarly, no dependence on pump power could be noticed as far as de-amplification was concerned (Fig. 6.11).

In summary, our setup was affected by a parasitic classical signal at 68 kHz which may have had negative effects on the phase- or mode-matching of the down-conversion process. The almost total absence of classical de-amplification—and therefore of squeezing—could not be remedied by any of our attempts to match the modes of the pump, seed, and local oscillators despite visibilities all above 90%. This was made all the more puzzling by the complete independence of de-amplification on either pump power or crystal temperature. Although a defective crystal may have been at the origin, other factors could have contributed in addition to the laser noise. Among these nuisances, one can cite gain-induced diffraction due to a too tight focusing of the pump [121], group-velocity dispersion whereby pulses

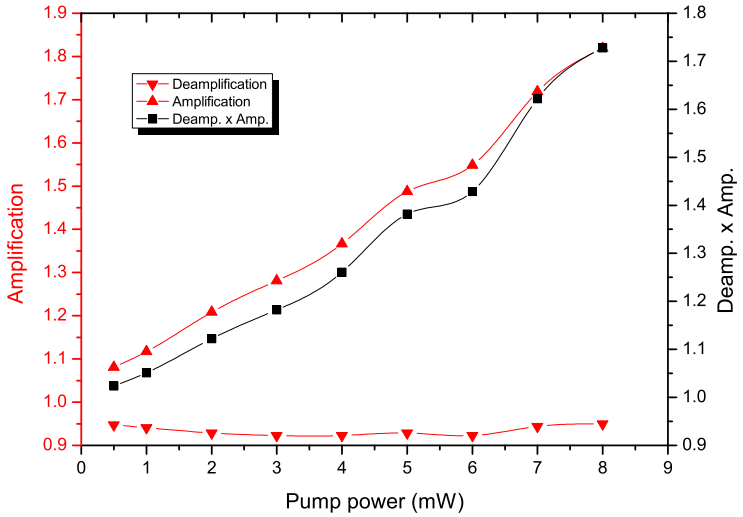

Figure 6.11: Classical amplification ($\triangle$) and de-amplification($\triangledown$) as a function of the pump power. The product of amplification and de-amplification ($\square$) indicates the purity of classical gain whereby unit purity corresponds to a product of 1.

reshaped as they traverse crystal [123], as well as thermal lensing [134] and spatial distortions of laser modes [132, 131].

Chapter 7

Conclusion and outlook

This dissertation is the collection of three seemingly disjointed topics: Teleportation, Bell tests, and the amplification of coherent state superpositions. In all three cases, however, the main challenge can be reduced to a measurement problem. Regardless of whether the measurement operation is an end in itself—as in Bell tests—or part of a state engineering protocol—as in teleportation and cat-state amplification—the experimentalist has traditionally had to make-do with either photon counting or homodyning. These detection schemes correspond to two mindsets, namely the DV and CV approaches, which have long been considered separately. Increasingly, however, hybrid schemes are used to harness the advantages of both DV and CV detection in the same setup. This was illustrated in Chap. 5 where the nonlinearity engendered by photon counting is used to produce small nonclassical cat states. The subsequent amplification of these states, which requires the discrimination of the vacuum from even cat states is on the other hand more conveniently performed by the thresholding of continuous variables. In the case of Bell tests (Chap. 4), the very nature of the measurements is that they are either aligned with or diagonal to the energy eigenbasis and thus call for DV and CV detection, respectively.

One could be tempted to think that in *quantum* mechanics, only *quanta* matter and hence that DV measurements ought to be preferable. However, the superposition principle implies that orthogonal quanta can carry relative phases which are *continuous*. Such continuous spectra are best obtained by some sort of interference—as opposed to energy—measurement, of which homodyning is the most prominent example. The downside with continuous measurements obtained from homodyning is that quantumness is inevitably blurred out and orthogonal states can only be distinguished up

to a non-ideal confidence level. Depending on the desired goal, this inherent ambiguity of CV measurement remains nonetheless an attractive compromise. The alternative, if one were to stick with DV measurement bases, is that superpositions such as $|0\rangle \pm |1\rangle$ can only be read out unambiguously through very unwieldy transfers onto atomic systems, as shown in Chap. 3. In all scenarios, the assessment of pros and cons for DV and CV schemes always passes by a feasibility study which incorporates losses and quantum inefficiencies. Only then can one make an informed choice as to photon detection or homodyning is more reliable at discriminating different states.

If one is to venture any forecast on the trend in measurement techniques, the future may very well lie with adaptive techniques such as those briefly mentioned in §2.3.5. Just like hybrid measurements allow one to choose freely between one of two measurement perspectives, say, between DV and CV, adaptive measurements provide one additional freedom in that they probe a continuum of perspectives with weak measurements. An intuitive illustration of this point is shown in Fig. 7.1.

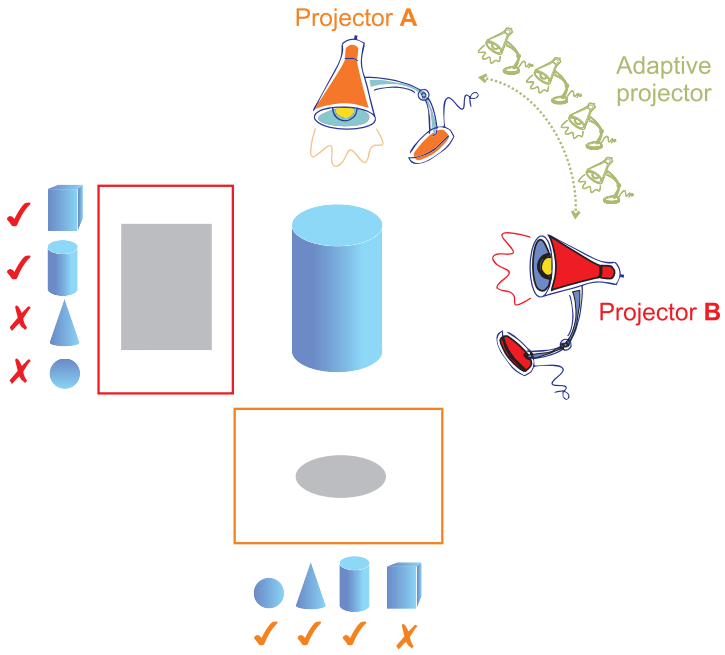

Figure 7.1: Conceptual representation of adaptive measurements. Consider two conjugate observables A and B for which there exists ideal projectors $\boldsymbol{A}$ and $\boldsymbol{B}$. For being complementary, either one of $\boldsymbol{A}$ and $\boldsymbol{B}$ has no access to the perspective of the other. A tomography of the "quantum object" in this case requires consecutive measurements of A and B, and hence two copies of the quantum object. A conjunction of the possible candidates from each measurement then identifies the object: $(\checkmark_{\text{sphere}}\checkmark_{\text{cone}}\checkmark_{\text{cylinder}}\boldsymbol{\times}_{\text{cuboid}})_A \wedge (\boldsymbol{\times}_{\text{sphere}}\boldsymbol{\times}_{\text{cone}}\checkmark_{\text{cylinder}}\checkmark_{\text{cuboid}})_B = (\boldsymbol{\times}_{\text{sphere}}\boldsymbol{\times}_{\text{cone}}\checkmark_{\text{cylinder}}\boldsymbol{\times}_{\text{cuboid}})$. But what if one cannot perform consecutive measurement? In other words, what if one only has one copy of the quantum object? Adaptive schemes can then be considered as an array of weak measurements which slide between the orthogonal perspectives of A and B according to a given algorithm which maximizes the garnered information about the state.

Bibliography

[1] J. Calsamiglia N. Lütkenhaus and K. A. Suominen. Tbd. Phys. Rev. A, 59, 1999.

[2] P. van Loock. Optical hybrid approaches to quantum information. Laser Photonics Rev., 5, 2011.

[3] M. Fox. Quantum Optics. Oxford University Press, Oxford, 2006.

[4] R. Shankar. Principles of quantum mechanics. Kluwer Academic/Plenum Publishers, New York, 1994.

[5] H. Weyl. Quantenmechanik und gruppentheorie. Zeitschrift für Physik, 45:1, 1927.

[6] W. Schleich. Quantum optics in phase space. Wiley-VCH, Berlin, 2001.

[7] J. S. Neergaard-Nielsen *et al.* Optical continuous-variable qubit. Phys. Rev. Lett., 105, 2010.

[8] R. Landauwer. Information is physical. In Proc. Workshop on Physics and Computation PhysComp '92, page 1, Los Alamitos, 1993. IEEE Comp. Sci. Press.

[9] D. Schuch and M. Moshinsky. Wigner distribution functions and the representation of canonical transformations in time-dependent quantum mechanics. SIGMA, 4, 2008.

[10] J. E. Moyal. Proceedings of the Cambridge philosophical society, 45, 1949.

[11] S. L. Braunstein and P. van Loock. Quantum information with continuous variables. Reviews of Modern Physics, 77, 2005.

[12] M. O. Scully and M. S. Zubairy. Quantum Optics. Cambridge University Press, Cambridge, UK, 1997.

[13] A. Laghaout P. Marek M. Jezek A. Tipsmark, R. Dong and U. L. Andersen. Experimental demonstration of a hadamard gate for coherent state qubits. Phys. Rev. A, 84, 2011.

[14] T. Gerrits *et al.* Generation of optical coherent-state superpositions by number-resolved photon subtraction from the squeezed vacuum. Phys. Rev. A, 82, 2010.

[15] G. Fujii D. Fukuda S. Kurimura N. Namekata, Y. Takahashi and S. Inoue. Non-gaussian operation based on photon subtraction using a photon-number-resolving detector at a telecommunications wavelength. Nature, 4, 2010.

[16] H. M. Wiseman. Adaptive phase measurements of optical modes: Going beyond the marginal Q distribution. Phys. Rev. Lett., 25, 1995.

[17] H. M. Wiseman. Quantum trajectories and quantum measurement theory. Quantum Semiclass. Opt., 8, 1996.

[18] M.A. Nielsen and I.L. Chuang. Quantum computation and quantum information. Cambridge University Press, Cambridge, 2000.

[19] D. F. Walls S. M. Tan and M. J. Collett. Nonlocality of a single photon. Phys. Rev. Lett., 66, 1991.

[20] L. Hardy. Nonlocality of a single photon revisited. Phys. Rev. Lett., 73, 1994.

[21] A. Peres. Nonlocal effects in fock space. Phys. Rev. Lett., 74, 1995.

[22] M. A. Horne D. M. Greenberger and A. Zeilinger. Nonlocality of a single photon? Phys. Rev. Lett., 75, 1995.

[23] L. Vaidman. Nonlocality of a single photon revisited again. Phys. Rev. Lett., 75, 1995.

[24] M. Pawlowski and M. Czachor. On entanglement with vacuum. Phys. Rev. A, 73, 2006.

[25] A. Drezet. Comment on single-particle entanglement. Phys. Rev. A, 74, 2006.

[26] S. J. van Enk. Reply to "'comment on 'single-particle entanglement'"'. Phys. Rev. A, 74, 2006.

[27] M.H.Y. Moussa and B. Baseia. Nonlocality of a single particle: From the fock space to cavity qed. Physics Letters A, 245, 1998.

[28] A. M. Steinberg. Single-particle nonlocality and conditional measurements. Found. Phys., 28, 1998.

[29] H.-W. Lee and J. Kim. Quantum teleportation and bells inequality using single-particle entanglement. Phys. Rev. A, 63, 2000.

[30] P. Jonsson G. Björk and L. L. Sánchez-Soto. Tbd. Phys. Rev. A, 64, 2001.

[31] Y. W. Chung H.-W. Lee J.-W. Lee, E. K. Lee and J. Kim. Tbd. Phys. Rev. A, 68, 2003.

[32] H. Nha and H. J. Carmichael. Proposed test of quantum nonlocality for continuous variables. Phys. Rev. Lett., 93, 2004.

[33] J. Dunningham and V. Vedral. Tbd. Phys. Rev. Lett., 99, 2007.

[34] S. Manciniz M. A. Anisimov, M. Caponigro and V. I. Man'ko. Tbd. J. Phys.: Conf. Ser., 70, 2007.

[35] J. J. Cooper and J. A. Dunningham. Tbd. New J. Phys., 10, 2008.

[36] K. S. Choi S. B. Papp H. Deng P. Lougovski, S. J. van Enk and H J Kimble. Tbd. New J. Phys, 11, 2009.

[37] L. Heaney and J. Anders. Phys. rev. a. Phys. Rev. A, 80, 2009.

[38] M. F. Santos L. Heaney, A. Cabello and V. Vedral. Tbd. New J. Phys., 13, 2011.

[39] H. Heydari B. Hessmo, P. Usachev and G. Björk. Tbd. Phys. Rev. Lett., 92, 2004.

[40] H. Deng P. Lougovski S. J. van Enk S. B. Papp, K. S. Choi and H. J. Kimble. Tbd. Science, 324, 2009.

[41] D. Salart *et al.* Tbd. Phys. Rev. Lett., 104, 2010.

[42] C. C. Gerry. Nonlocality of a single photon in a cavity qed. Phys. Rev. A, 53, 1996.

[43] H. Heydari J. Söderholm G. Björk, P. Jonsson and B. Hessmo. Tbd. Opt. Spectroscopy, 94, 2003.

[44] S. Popescu E. Lombardi, F. Sciarrino and F. De Martini. Teleportation of a vacuum–one-photon qubit. Phys. Rev. Lett., 88, 2002.

[45] M. Pavičić. Near-deterministic discrimination of all bell states with linear optics. Phys. Rev. Lett., 107, 2011.

[46] S. Wechsler. Nonlocality of single fermions - branches that borrow particles. e-print arXiv:quant-ph/0503232v1, 2005.

[47] J. A. Dunningham M. O. Terra Cunha and V. Vedral. Tbd. Proc. R. Soc. A, 463, 2007.

[48] L. Heaney and V. Vedral. Tbd. Phys. Rev. Lett., 103, 2009.

[49] L. Heaney. Teleportation of a quantum state of a spatial mode with a single massive particle. e-print arXiv:1011.3743, 2010.

[50] J. Calsamiglia and N. Lütkenhaus. Maximum efficiency of a linear-optical bell-state analyzer. Appl. Phys. B, 72, 2001.

[51] I. L. Chuang and Y. Yamamoto. Simple quantum computer. Phys. Rev. A, 52, 1995.

[52] H. A. Haus N. Imoto and Y. Yamamoto. Tbd. Phys. Rev. A, 32, 1985.

[53] A. P. Lund and T. C. Ralph. Nondeterministic gates for photonic single-rail quantum logic. Phys. Rev. A, 66, 2002.

[54] B. Podolsky A. Einstein and N. Rosen. Can quantum-mechanical description of physical reality be considered complete? Physical Review, 47:777, 1935.

[55] J. S. Bell. On the einstein-poldolsky-rosen paradox. Physics (Long Island City, N.Y.), 1:195, 1964.

[56] P. Grangier A. Aspect and G. Roger. Experimental realization of einstein-podolsky-rosen-bohm gedankenexperiment: A new violation of bell's inequalities. Phys. Rev. Lett., 49, 1982.

[57] P. M. Pearle. Hidden-variable example based upon data rejection. Phys. Rev. D, 2, 1970.

[58] M. A. Rowe *et al.* Experimental violation of a bell's inequality with efficient detection. Nature, 409, 2001.

[59] C. Simon H. Weinfurter G. Weihs, T. Jennewein and A. Zeilinger. Violation of bell's inequality under strict einstein locality conditions. Phys. Rev. Lett., 81, 1998.

[60] T. Scheidl *et al.* Violation of local realism with freedom of choice. PNAS, 107, 2010.

[61] A. J. Miller A. E. Lita and S. W. Nam. Counting near-infrared single-photons with 95 Optics Express, 16, 2008.

[62] B. Yurke and D. Stoler. Observing local realism violations with a combination of sensitive and insensitive detectors. Phys. Rev. Lett., 79, 1997.

[63] M. D. Reid A. Gilchrist, P. Deuar. Contradiction of quantum mechanics with local hidden variables for quadrature phase amplitude measurements. Phys. Rev. Lett., 80, 1998.

[64] A. Ferraro A. Acín, N. J. Cerf and J. Niset. Tests of multimode quantum nonlocality with homodyne measurements. Phys. Rev. A, 79, 2009.

[65] J. Fiurášek R. García-Patrón and N. J. Cerf. Loophole-free test of quantum nonlocality using high-efficiency homodyne detectors. Phys. Rev. A, 71, 2005.

[66] H. Jeong. Testing bell inequalities with photon-subtracted gaussian states. Phys. Rev. A, 78, 2008.

[67] N. D. Mermin. Extreme quantum entanglement in a superposition of macroscopically distinct states. Phys. Rev. Lett., 65:1838, 1990.

[68] M. Wieśniak D. Kaszlikowski A. Sen(De), U. Sen and M. Żukowski. Multiqubit w states lead to stronger nonclassicality than greenberger-horne-zeilinger states. Phys. Rev. A, 68:062306, 2003.

[69] G. Vidal W. Dür and J.I. Cirac. Three qubits can be entangled in two inequivalent ways. Phys. Rev. A, 62:062314, 2000.

[70] R. Chaves and L. Davidovich. Robustness of entanglement as a resource. Phys. Rev. A, 82:052308, 2010.

[71] J. S. Bell. Speakable and Unspeakable in Quantum Mechanics. Cambridge University Press, Cambridge, England, 1988.

[72] E. S. Polzik U. L. Andersen J. B. Brask, I. Rigas and A. S. Sørensen. Hybrid long-distance entanglement distribution protocol. Phys. Rev. Lett., 105:160501, 2010.

[73] J. I. Cirac L.-M. Duan, M. D. Lukin and P. Zoller. Long-distance quantum communication with atomic ensembles and linear optics. Nature, 414:413, 2001.

[74] A. Cabello. Bell's theorem with and without inequalities for the three-qubit greenberger-horne-zeilinger and w states. Phys. Rev. A, 65:032108, 2002.

[75] P. Skrzypczyk A. Salles D. Cavalcanti, N. Brunner and V. Scarani. Large violation of bell inequalities using both particle andwave measurements. Phys. Rev. A, 84:022105, 2011.

[76] A. J. Miller D. Rosenberg, A. E. Lita and S. W. Nam. Noise-free high-efficiency photon-number-resolving detectors. Phys. Rev. A, 71:061803, 2005.

[77] R. Chaves and J. Bohr Brask. Feasibility of loophole-free nonlocality tests with a single photon. arXiv:1110.3721v1, 2011.

[78] G. J. Milburn P. T. Cochrane and W. J. Munro. Macroscopically distinct quantum-superposition states as a bosonic code for amplitude damping. Phys. Rev. A, 59, 1999.

[79] G. J. Milburn W. J. Munro T. C. Ralph, A. Gilchrist and S. Glancy. Quantum computation with optical coherent states. Phys. Rev. A, 68, 2003.

[80] W. J. Munro T. C. Ralph S. Glancy S. L. Braunstein A. Gilchrist, K. Nemoto and G. J. Milburn. Schrdinger cat states and their power for quantum information processing. J. Opt. B: Quantum Semiclassical Opt., 6, 2004.

[81] T. C. Ralph. Coherent superposition states as quantum rulers. Phys. Rev. A, 65, 2002.

[82] G. J. Milburn W. J. Munro, K. Nemoto and S. L. Braunstein. Weak-force detection with superposed coherent states. Phys. Rev. A, 66, 2002.

[83] W. J. Munro J. Joo and T. P. Spiller. Quantum metrology with entangled coherent states. Phys. Rev. Lett., 107, 2011.

[84] H. Jeong. Testing bell inequalities with photon-subtracted gaussian states. Phys. Rev. A, 78, 2008.

[85] H. Jeong M Stobińska and T. C. Ralph. Violation of bell's inequality using classical measurements and nonlinear local operations. Phys. Rev. A, 75, 2007.

[86] C.-W. Lee and H. Jeong. Effects of squeezing on quantum nonlocality of superpositions of coherent states. Phys. Rev. A, 80, 2009.

[87] M. G. A. Paris G. McKeown and M. Paternostro. Testing quantum contextuality of continuous-variable states. Phys. Rev. A, 83, 2011.

[88] B. Yurke and D. Stoler. Generating quantum mechanical superpositions of macroscopically distinguishable states via amplitude dispersion. Phys. Rev. Lett., 57, 1986.

[89] A. Mecozzi and P. Tombesi. Distinguishable quantum states generated via nonlinear birefringence. Phys. Rev. Lett., 58, 1987.

[90] T. C. Ralph H. Jeong, M. S. Kim and B. S. Ham. Generation of macroscopic superposition states with small nonlinearity. Phys. Rev. A, 70, 2004.

[91] S. Glancy and H. M. de Vasconcelos. Methods for producing optical coherent state superpositions. J. Opt. Soc. Am. B, 25, 2008.

[92] T. Opatrný L. Knöll M. Dakna, T. Anhut and D.-G. Welsch. Generating schrdinger-cat-like states by means of conditional measurements on a beam splitter. Phys. Rev. A, 55, 1997.

[93] R. Tualle-Brouri J. Wenger and P. Grangier. Non-gaussian statistics from individual pulses of squeezed light. Phys. Rev. Lett., 92, 2004.

[94] J. Laurat A. Ourjoumtsev, R. Tualle-Brouri and P. Grangier. Generating optical schrdinger kittens for quantum information processing. Science, 312, 2006.

[95] C. Hettich K. Mølmer J. S. Neergaard-Nielsen, B. M. Nielsen and E. S. Polzik. Generation of a superposition of odd photon number states for quantum information networks. Phys. Rev. Lett., 97, 2006.

[96] A. P. Lund H. Jeong and T. C. Ralph. Production of superpositions of coherent states in traveling optical fields with inefficient photon detection. Phys. Rev. A, 72, 2005.

[97] T. C. Ralph A. P. Lund and H. L. Haselgrove. Fault-tolerant linear optical quantum computing with small-amplitude coherent states. Phys. Rev. Lett., 100, 2008.

[98] R. Tualle-Brouri A. Ourjoumtsev, H. Jeong and P. Grangier. Generation of optical schrödinger cats from photon number states. Nature, 448, 2007.

[99] A. Furusawa K. Wakui, H. Takahashi and M. Sasaki. Photon subtracted squeezed states generated with periodically poled ktiopo4. Opt. Express, 15, 2007.

[100] A. E. B. Nielsen and Klaus Mølmer. Transforming squeezed light into a large-amplitude coherent-state superposition. Phys. Rev. A, 76, 2007.

[101] H. Takahashi M. Takeoka and M. Sasaki. Large-amplitude coherent-state superposition generated by a time-separated two-photon subtraction from a continuous-wave squeezed vacuum. Phys. Rev. A, 77, 2008.

[102] H. Jeong P. Marek and M. S. Kim. Generating squeezed superpositions of coherent states using photon addition and subtraction. Phys. Rev. A, 78, 2008.

[103] H. Nha C.-W. Lee, J. Lee and H. Jeong. Generating a schrdinger-cat-like state via a coherent superposition of photonic operations. Phys. Rev. A, 85, 2012.

[104] T. C. Ralph A. P. Lund, H. Jeong and M. S. Kim. Conditional production of superpositions of coherent states with inefficient photon detection. Phys. Rev. A, 70, 2004.

[105] M. Takeoka and M. Sasaki. Conditional generation of an arbitrary superposition of coherent states. Phys. Rev. A, 75, 2007.

[106] E. S. Polzik U. L. Andersen J. B. Brask, I. Rigas and A. S. Sørensen. Hybrid long-distance entanglement distribution protocol. Phys. Rev. Lett., 105, 2010.

[107] P. L. Knight M. S. Kim, E. Park and H. Jeong. Nonclassicality of a photon-subtracted gaussian field. Phys. Rev. A, 71, 2005.

[108] A. Dantan P. Grangier M. Wubs R. Tualle-Brouri, A. Ourjoumtsev and A. S. Sørensen. Multimode model for projective photon-counting measurements. Phys. Rev. A, 80, 2009.

[109] M. Sasaki U. L. Andersen S. Suzuki, M. Takeoka and F. Kannari. Practical purification scheme for decohered coherent-state superpositions via partial homodyne detection. Phys. Rev. A, 73, 2006.

[110] J. S. Neergaard-Nielsen *et al.* Quantum tele-amplification with a continuous variable superposition state. e-print arXiv:1211.6634, 2012.

[111] M. Barbieri P. Grangier R. Blandino, F. Ferreyrol and R. Tualle-Brouri. A method for characterizing coherent-state quantum gates. e-print arXiv:1105.5510, 2011.

[112] J. S. Neergaard-Nielsen A. Tipsmark and U. L. Andersen. Displacement-enhanced entanglement distillation of single-mode-squeezed entangled states. Optics Express, 21, 2013.

[113] I. Rigas C. Kragh A. Tipsmark A. Laghaout, J. S. Neergaard-Nielsen and U. L. Andersen. Amplification of realistic schrdinger-cat-state-like states by homodyne heralding. Phys. Rev. A, 87, 2013.

[114] B. Yurke, P. Grangier, R.E. Slusher, and M. J. Potasek. Generating and detecting short-duration pulses of squeezed light. Physical Review A, 35:3586, 1987.

[115] C. Hettich P. Lodahl A. I. Lvovsky J. Mlynek H. Hansen, T. Aichele and S. Schiller. Ultrasensitive pulsed, balanced homodyne detector: application to time-domain quantum measurements. Optics Letters, 26, 2001.

[116] B.G. Kim, E. Garmire, S.G. Hummel, and P.D. Dapkus. Nonlinear bragg reflector based on saturable absorption. Applied Physics Letters, 54:1095–1097, 1989.

[117] Ralf Menzel. Photonics: Linear and Nonlinear Interactions of Laser Light and Matter. Springer-Verlag, 2001.

[118] A. Arie A. Bahabad, N. Voloch and R. Lifshitz. Experimental confirmation of the general solution to the multiple-phase-matching problem. J. Opt. Soc. Am. B, 24, 2007.

[119] G.D. Boyd and D.A. Kleinman. Parametric interaction of focused gaussian light beams. Journal of Applied Physics, 39:3597–3639, 1968.

[120] A.M. Weiner, A.M. Kanan, and D.E. Leaird. High-efficiency blue generation by frequency doubling of femtosecond pulses in a thick nonlinear crystal. Optics Letters, 23:1441–1443, 1959.

[121] Arthur La Porta and Richard E. Slusher. Squeezing limits at high parametric gains. Physical Review A, 44:2013, 1991.

[122] E. M. Daly and A. I. Ferguson. Spatial and temporal dependence of single-pass parametric gain. Journal of Modern Optics, 48, 2001.

[123] B.E.A. Saleh and M.C. Teich. Fundamentals of photonics. Wiley-Interscience, 2007.

[124] C. C. Gerry and P. L. Knight. Introductory quantum optics. Cambridge University Press, Cambridge, 2005.

[125] I.A. Walmsley A.B. U'Ren, K. Banaszek. Photon engineering for quantum information processing. e-print arXiv:quant-ph/0305192, 2003.

[126] A. Tipsmark. Generation of optical coherent state superpositions for quantum information processing (PhD thesis). Technical University of Denmark, 2012.

[127] A. I. Lvovsky and M. G. Raymer. Continuous-variable optical quantum-state tomography. Review of Modern Physics, 81, 1997.

[128] W. T. Vetterling B. P. Flannery W. H. Press, S. A. Teukolsky. Numerical Recipes 3rd Edition: The Art of Scientific Computing. Cambridge University Press, Cambridge, UK, 2007.

[129] Jürgen Appel, Dallas Hoffman, Eden Figueroa, and A.I. Lvovsky. Electronic noise in optical homodyne tomography. Physical Review A, 75:035802, 2007.

[130] Kahraman G. Köprülü and Orhan Aytür. Analysis of the generation of amplitude-squeezed light with gaussian-beam degenerate optical parametric amplifiers. J. Opt. Soc. Am. B, 18, 2001.

[131] J. E. Bjorkholm. Some effects of spatially nonuniform pumping in pulsed optical parametric oscillators. IEEE Journal of Quantum Electronics, 7:109, 1971.

[132] Preben Buchhave and Peter Tidemand-Lichtenberg. Generation of higher order gauss-laguerre modes in single-pass 2nd harmonic generation. Optics Express, 16:17952, 2008.

[133] Jérôme Wenger, Rosa Tualle-Brouri, and Philippe Grangier. Pulsed homodyne measurements of femtosecond squeezed pulses generated by single-pass parametric deamplification. Optics Letters, 29:1267, 2003.

[134] E.S. Polzik and H.J. Kimble. Frequency doubling with knbo3 in an external cavity. Optics Letters, 16:1400, 1991.